Alma Mater Studiorum - Università di Bologna

School of Science
Department of Physics and Astronomy
Master Degree Programme in Astrophysics and Cosmology

Inspecting Acoustic Energy as a Candidate Source of Mass Loss in Red Giant Branch Stars

Graduation Thesis

March 27, 2026

Presented by:
Leonardo Nicchiarelli

Supervisor:
Chiar.mo Prof. Andrea Miglio

Co-supervisors:
Prof. Benoît Mosser
Dr. Kévin Belkacem
Dr. Jordan Philidet
Dr. Louis Manchon
Dr. Walter E. van Rossem

Academic year 2024-2025
Graduation date V

Abstract

It has long been known that stars experience mass loss while evolving along the red giant branch (RGB). Nonetheless, the theoretical understanding of the mechanisms driving mass loss is still very poor. The most used prescription for the mass loss rate along the RGB is the Reimers' law (Reimers 1975), which lacks a solid physical foundation. A large set of theories can be grouped under the "family" of thermal winds, where mass loss consists in evaporation of coronal gas, heated by dissipation of the energy associated to magnetohydrodynamic or acoustic waves. The latter are generated by convective motions within the stellar envelope and propagate above the photosphere, where they are damped.

Fusi-Pecci and Renzini (1975) (FPR, hereafter) derived an equation where the mass loss rate relates to the total rate of acoustic energy emitted by the envelope. The physical assumptions at the basis of their approach have various limitations, primarily the use of the mixing length theory (MLT).

The scope of this project is reviewing the role of acoustic energy in the FPR mass loss prescription, on the basis of the acoustic energy extracted from the 3D atmosphere models of the Stagger grid (Magic et al. 2013). In particular, the total rate of acoustic energy is corrected on the basis of the information extracted from 3D simulations. Both the standard FPR prescription and the updated one (FPR3D, hereafter) are implemented in the 1D stellar evolutionary code Module for Experiments in Stellar Astrophysics (MESA).

A strong concentration of mass loss is found close to the RGB tip, both for the standard FPR and FPR3D models. The dependence of the total mass loss on metallicity is instead very different: for [Fe/H] $\gtrsim -0.5$, standard FPR models show a decreasing trend, whereas the FPR3D models are characterized by a monotonically increasing trend. These results are compared with the predictions of Reimers mass loss and recent observational mass-loss estimates.

Contents

Chapter 1

Mass Loss in Red Giant Branch Stars

The fact that stars lose a relevant fraction of their envelope mass along the red giant branch (RGB) has been firmly confirmed over the past decades of observations. Numerous independent techniques are now available to constrain both the mass loss rate from individual stars and the total RGB mass loss from stellar population studies. In section 1.1, I will describe the methods used in observations. The structure of this section follows the historical development of these techniques, starting with the early spectroscopic discovery of mass loss in giant stars (which dates back to more than 90 years ago) and leading to the most recent techniques, involving asteroseismology.

Unfortunately, from a theoretical point of view, our understanding of mass loss mechanisms along the RGB is still rudimentary. As described later, the number of potential physical processes that could drive mass ejecta from the atmosphere of giant stars is very large. This is what makes developing a satisfactory theory on RGB mass loss very complicated. In stellar models, the rate of mass loss along the RGB is widely calculated on the basis of prescriptions that lack a solid physical background. The most used prescription is the Reimers' law (Reimers 1975), which I will extensively discuss in section 1.2. As I will explain later, this prescription cannot reproduce some of the constraints coming from observations, such as the trend of the integrated RGB mass loss with metallicity observed in different stellar populations.

In view of the above considerations, it is clear that putting more effort in studying mass loss from a theoretical point of view is important in the field of stellar astrophysics. However, the importance of RGB mass loss is not only related to this specific field. In fact, many other branches in astrophysics would benefit from a better understanding of the mechanisms driving mass loss in RGB stars. For example:

- more accurate predictions on the dynamical evolution and fate of planets in planetary systems, including our own (Schröder and Smith 2008);
- determination of more accurate age estimates of red clump (RC) stars. In fact, the stellar age in the red-giant phase is primarily determined by the initial mass. However, the mass of RC stars is lower than their initial mass, because part of their envelope is lost throughout the RGB. Therefore, better constraints on the efficiency of mass loss would improve the accuracy of the initial-mass estimates of RC stars, thus leading to better age estimates (Miglio, Chiappini, et al. 2021).

This would have a crucial impact on studies related Galactic archaeology (i.e., the chemical and dynamical evolution of the Milky Way);

- better understanding of the formation of subdwarf B (sdB) stars, which are hot He-core burning stars with a very thin envelope. They are thought to be the product of stars that have lost nearly all of their envelope. Given their high surface temperatures, sdB stars are intense UV-emitters. Therefore, improving the understanding of the formation of these objects would also advance the study of the UV excess in old stellar systems (Han et al. 2002).

1.1 Observational evidence

1.1.1 The early discovery of mass loss in evolved stars

The presence of gas outflows from giant stars was recognized many decades ago. Adams and MacCormack (1935) discovered that on high dispersion spectra of α Orionis and other bright giants (such as α^1 Herculis and α Cygni), the strongest resonance lines showed deep absorption cores displaced shortward from the center of the photospheric lines. They found this feature for the sodium D_1 and D_2 lines, for the H and K lines of CaII and for the pair of AlI lines between H and K. The typical velocity of these outflows was estimated to be of the order of $5\,\mathrm{km\,s^{-1}}$, well below the estimated escape velocity at the stellar surface. In the years that followed, given their low velocities, winds were considered as phenomena confined in the region around the stellar surface and it was generally assumed that almost none of the matter escapes from giant stars.

The idea that evolved stars could lose a substantial fraction of their mass started to grow between the late '50s and the early '60s. The main argument was a comparison between the number of star deaths and the number of detected supernovae. As Weymann (1963) states in his exhaustive review on mass loss from giant stars: "for stars with masses greater than the white dwarf limit the star cannot stabilize itself by attaining a degenerate configuration [...]. It is now believed that at some point strongly endothermic nuclear processes will occur [...]. The collapse of the star in a short time scale will inevitably release an enormous amount of energy which we would presumably detect as a supernova explosion". For this reason, the mismatch between the number of supernovae and the number of star deaths with masses $M > 1.5\,\mathrm{M_\odot}$ was believed to indicate the existence of some kind of mechanism capable of removing a relevant fraction of stellar mass. Furthermore, the progress made in the study of high dispersion spectra showed that relatively slow gas outflows are *not* confined in the region close to the stellar atmosphere. The pioneering discovery was done on the α Herculis system by Deutsch (1956), who noticed that the blueshifted absorption cores in α^1 Her (a M-type supergiant) are also present in the spectrum of its visual companion (a G-type giant). Since no comparable blueshifted cores were known in other G-type stars, Deutsch concluded that the visual companion is embedded within an extended envelope of gas, which expands from the brighter M-type star at around $10\,\mathrm{km\,s^{-1}}$. The distance between the visual companion and the bright M-type supergiant was estimated to be around 360 times the radius of the M star, where the expansion velocity exceeds the escape velocity. Therefore, Deutsch concluded that α^1 Her *loses mass* to the interstellar medium, at an estimated rate of at least $3 \times 10^{-8}\,\mathrm{M_\odot\,yr^{-1}}$. In the following years, a high dispersion survey of all red giants accessible at that time was

performed, and cool expanding envelopes were recognized in the spectra of all giants and supergiants later than M0 and in many K and G supergiants. As of 1975, more than 120 M type giants, K giants of luminosity class II, G, K, and M supergiants were known to have circumstellar absorption lines (Reimers 1975).

Further measurements of mass loss rates became available in the late '60s, thanks to the analysis of circumstellar dust emission in the infrared and of molecular emission in the microwave. Dust grains are components of circumstellar envelopes which are heated by stellar radiation and re-emit in the infrared band. For this reason, analyzing infrared emission was soon recognized as a powerful tool to trace mass loss. I will return to the connection between dust grains and mass loss in sections 1.2.1 and 1.2.3.

1.1.2 Inferring mass loss from the HB morphology

Together with advances in dynamical detection of gas outflows, new independent evidence of mass loss along the RGB started to be available from the early '70s, thanks to the study of the horizontal branch (HB) morphology in the color magnitude diagram (CMD) of some globular clusters. The indirect methods developed in those years were of crucial importance, because they were the first evidence demonstrating the relevance of mass loss in stellar evolution. Given its importance, I summarize in this paragraph how it is possible to obtain information on mass loss thanks to the observed HB morphology in globular clusters.

A simple stellar population (SSP) is an idealized stellar system where:

- All stars have the same age (they were born from a single burst of star formation);
- All stars have the same initial chemical composition (they originated from the same molecular cloud);
- There are no multiple systems (all stars are single).

For a long time, globular clusters (GCs) were believed to be the closest systems to SSPs in nature. Now, we know that they contain *multiple populations*: stars were not born in a single star formation burst and it is possible to distinguish at least two generations of stars in many GCs (for instance, see Gratton, Carretta, and Bragaglia 2012). Nonetheless, to a first approximation, stars can be considered to have the same age and same iron abundance [Fe/H]. For this reason, when a specific globular cluster is examined, we can reasonably ascribe a single age and a single [Fe/H] to it. The observed zero-age horizontal branch (ZAHB) position in a CMD is highly sensitive to metallicity. In particular, if we compare two globular clusters with almost the same age, one being more metal-rich than the other, the former is expected to have its ZAHB placed at a redder color. This is due to the fact that the turn-off (TO) mass of the more metal-rich cluster would be higher, which in turn implies a larger envelope mass at the ZAHB and a lower effective temperature $T_{\rm eff}$. However, this expected property is not found in some cases. For instance, the GCs M3 and M13 almost have the same metallicity ([Fe/H] $\simeq -1.6$) and same age (they have the same TO-mass), but the HB morphology is completely different, as shown in figure 1.1.

Besides metallicity, it is evident that another parameter (the so-called *second parameter*) must have an influence on the position of the observed horizontal branch. This problem was very clear also in the early '70s, when the anomalous HB morphologies were discovered. It was soon after these discoveries that mass loss along the RGB

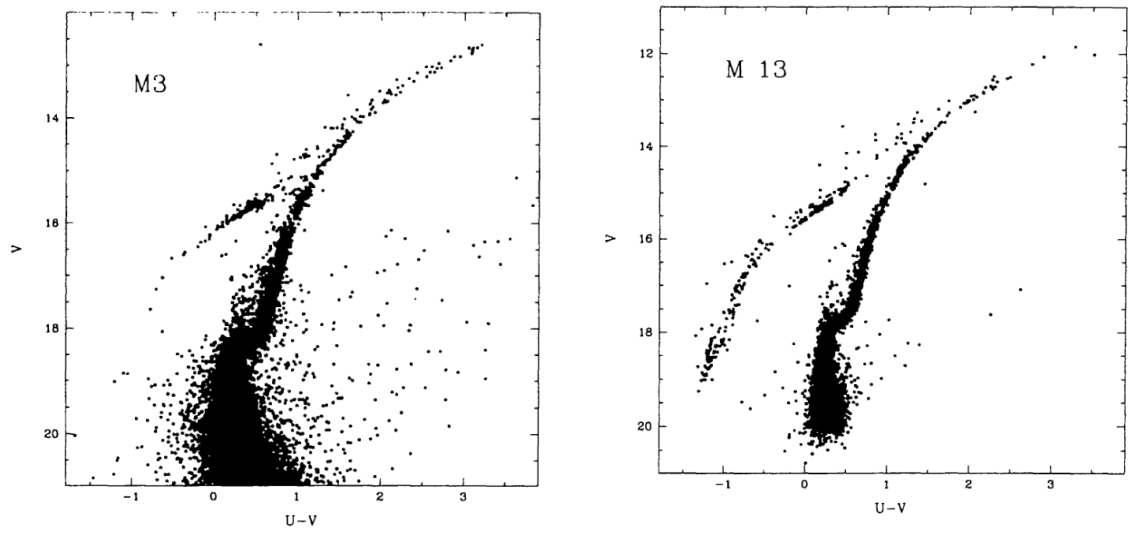

Figure 1.1: Comparison between the color magnitude diagrams (V, $U-V$) of M3 and M13. The horizontal branch of M13 is clearly more extended to the blue than that of M3. Source: *Ferraro, Paltrinieri, and Cacciari 1999*

was suggested to be the other "parameter" affecting the HB morphology. In particular, mass loss acts in the opposite direction as the metallicity effect: if stars lose a substantial portion of their envelope while ascending the RGB, they will begin the stable core helium burning phase with less massive and thinner envelopes (which implies higher effective temperature $T_{\rm eff}$). This would explain the anomalous extension to the blue of the HB of some globular clusters. From a theoretical study on the Hertzsprung-Russell (HR) diagram of globular clusters, Rood (1973) established that an integrated mass loss of $\Delta M \simeq 0.2\,{\rm M}_{\odot}$ is required to fit the observed HB morphology. Other possible candidate "second parameters" have been considered throughout the following years, but none of them is able to reproduce the HB morphology without considering mass loss along the RGB.

Our knowledge on globular clusters has improved since the '70s and, as anticipated previously, we now know that these systems are not perfect SSPs. From a dynamical point of view, the presence of binary stars is strictly connected to the formation of blue straggler stars (BSSs), which are of crucial importance in the study of globular clusters' dynamics. Concerning the chemical composition, several GCs are not homogeneous in the abundance of light elements (correlations and anti-correlations are found, for instance the Na-O anticorrelation). Also, internal spreads of helium abundance have been discovered in some globular clusters (e.g., in NGC 2808: Dalessandro et al. 2011). Particular care must be given to the He abundance, since it is another factor shaping the HB morphology: an increase in Y (the He abundance by mass) causes a lower TO-mass, which in turn leads to ZAHB stars with less massive and thinner envelopes (thus, higher $T_{\rm eff}$). For this reason, the presence of different populations having different Y further complicates the process of estimating integrated mass losses along the RGB. Nonetheless, the main result derived by Rood (1973) still remains a useful reference to have an indication on the expected amount of mass lost throughout the RGB.

In recent years, thanks to *asteroseismology* (the study of stellar pulsation), it is possible to obtain precise estimates of stellar masses. These recent methods are completely independent from HB morphology studies and can be used to infer precise integrated

mass loss along the RGB of globular clusters and other stellar populations.

1.1.3 Asteroseismic relations

In this section, I describe the main properties of oscillations in red giant stars and the most important connections between them and global stellar properties, including the mass. I follow the review by Jackiewicz (2021).

In general, a global resonant mode produces distortions on the stellar surface whose spatial pattern can be described by a spherical harmonic $Y_l^m(\theta, \phi)$. The angular degree l represents the total number of nodal lines across the surface and m determines how many of these nodal lines lie on a meridional plane. Figure 1.2 shows some examples of asymmetric modes (those having $m = 0$), tesseral modes (those with $l \neq m$) and sectoral modes (when $l = m$). For each oscillation mode, it is possible to identify the angular degree l and its radial order n, which in most cases can be interpreted as the number of nodes of the oscillation along the radial direction. Surface distortions can be either observed in small luminosity fluctuations or equivalently in Doppler shifts. Modes with high harmonic degree l distort the surface over small sectors. These high-l modes cannot be observed for stars other than the Sun, due to cancellation effects. In other words, for further stars we can only observe modes with the lowest degree ($l = 0, 1, 2, 3$), which distort the stellar surface with large scale distortions.

Stellar oscillations have been measured using various ground-based and space telescopes. Among the ground-based instruments, the Birmingham Solar Oscillations Network (BiSON) has been important to study low-degree solar oscillation modes since 1976. Another relevant network, led by the Aarhus University, is the Stellar Observations Network Group (SONG), which focuses on detecting oscillations of bright stars using radial-velocity measurements. However, the instruments that have allowed us to achieve great advances in asteroseismology are space instruments (e.g., the concluded French mission CoRoT and the NASA missions *Kepler* and TESS). The advantages of space telescopes are a higher S/N ratio and a much more extended time availability for observations, compared to ground-based instruments.

There are various physical processes which can cause the excitation of stellar oscillations. For example, classical radial pulsators (i.e., Cepheids and RR Lyrae) are located in a narrow region of the HR diagram — the instability strip — which favours the global excitation of modes through the $\kappa-$mechanism, a physical process that is controlled by opacity. On the other hand, many red giant stars instead display pulsations similar to the Sun (i.e., *solar-like oscillations*). The excitation of these modes is stochastic and is driven by turbulent convection in the outer envelope of the star. They are predominantly $p-$modes, that is pulsations whose restoring force is pressure.

Time series of luminosity or velocity fluctuations are best analyzed in the Fourier domain, where it is possible to better visualize which are the frequencies with the highest excitation (that is, the oscillations having the largest amplitudes). Figure 1.3 shows power spectra of the Sun, obtained from almost 20 years of data collected by the SOHO satellite. We can notice that the frequencies with the highest amplitude are around a value $\nu_{\max} \simeq 3090\,\mu$Hz. For lower frequencies, there are contributions to the spectrum by rotational signal, supergranulation and granulation; at high frequencies, it is found the contribution from the photon noise. In the bottom panel of figure 1.3, we can see two important features of the amplitude spectrum of solar-like oscillations: the

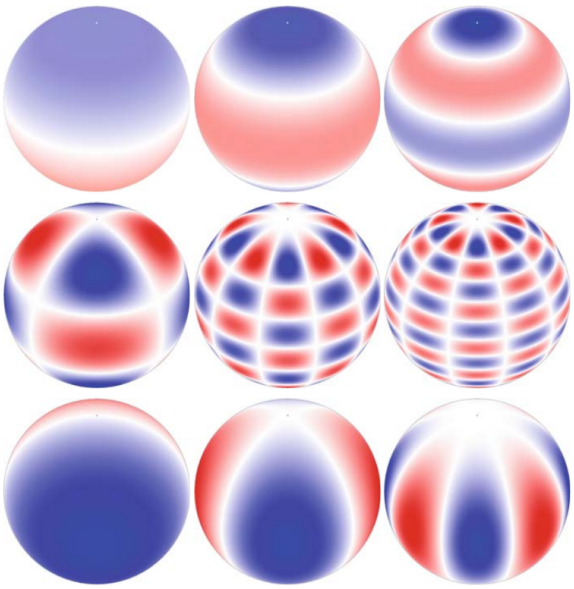

Figure 1.2: *Adapted from fig. B.1 in Aerts, Jørgen Christensen-Dalsgaard, and Kurtz (2010)*: Snapshots of the spatial pattern for various modes, viewed through an inclination angle of 55°. In red (blue): sections of the star moving in (out). The white bands are the surface nodes. *Top row*: asymmetric modes with, from left to right, $l = 1, 2, 4$. *Second row*: tesseral modes with, from left to right, $(l, m) = (4, 2), (10, 5), (15, 5)$. *Bottom row*: sectoral modes with, from left to right, $l = 1, 2, 4$.

large frequency spacing $\Delta\nu$ and the small frequency spacing $\delta\nu$. The former is defined as the difference between the frequency of two modes with consecutive radial order n and same angular degree l; the latter is still the difference between the frequencies of two modes with consecutive n, but with their respective degrees l differing by two.

The shape of the power spectra of solar-like oscillations in RGB stars is very similar to the solar one, as can be seen in figure 1.4. We can clearly see that, as the star evolves along the RGB, $\nu_{\max}$ decreases. Indeed, this quantity is strictly connected to the surface gravity of the star and to the effective temperature as:

$$\nu_{\max} \propto \nu_{ac} \propto \frac{g}{\sqrt{T_{\rm eff}}} \tag{1.1}$$

where $\nu_{\rm ac}$ is the atmospheric acoustic cut-off frequency. Equation (1.1) is typically normalized to the solar value:

$$\nu_{\max} = 3090 \frac{M/\mathrm{M}_\odot}{(R/\mathrm{R}_\odot)^2 \sqrt{T_{\rm eff}/\mathrm{T}_{\rm eff,\odot}}} \mu\mathrm{Hz} \tag{1.2}$$

Therefore, the observed decrease in $\nu_{\max}$ can be explained by the fact that surface gravity decreases with time because the radius grows as the star ascends the RGB. The oscillation frequencies with large amplitudes are typically of high radial order n. For such modes, the asymptotic theory of stellar oscillations can be used. Frequencies are related to n and l as follows:

$$\nu_{nl} \simeq \Delta\nu \left(n + \frac{l}{2} + \epsilon \right) - l(l+1) D_0 \tag{1.3}$$

where ϵ is a frequency-dependent term mostly dependent on near-surface effects, $\Delta\nu$ is the large frequency spacing defined previously and D_0 is:

$$D_0 \equiv -\frac{\Delta\nu}{4\pi^2\nu_{nl}} \int_0^R \frac{\mathrm{d}c_\mathrm{s}}{\mathrm{d}r}\frac{\mathrm{d}r}{r} \tag{1.4}$$

where c_s is the adiabatic sound speed. By looking at equations (1.3) and (1.4), we can see that the value of the frequencies is determined by the behaviour of the sound speed c_s in the stellar interior. The large frequency spacing $\Delta\nu$ is constant (at first order):

$$\Delta\nu \equiv \nu_{n,l} - \nu_{n-1,l} = \left(2\int_0^R \frac{\mathrm{d}r}{c_\mathrm{s}}\right)^{-1} \tag{1.5}$$

Since the sound speed scales as $c_\mathrm{s}^2 \propto MR^{-1}$, equation (1.5) implies that:

$$\Delta\nu \propto \sqrt{\frac{M}{R^3}} \propto \sqrt{\bar{\rho}} \tag{1.6}$$

where $\bar{\rho}$ is the mean density. Since $\bar{\rho}$ decreases as the star evolves along the RGB, also $\Delta\nu$ decreases. Combining (1.2) and (1.6), it is possible to derive the *asteroseismic scaling relations*:

$$\frac{M}{\mathrm{M}_\odot} = \left(\frac{\nu_\mathrm{max}}{\nu_{\mathrm{max},\odot}}\right)^3 \left(\frac{\Delta\nu}{\Delta\nu_\odot}\right)^{-4} \left(\frac{T_\mathrm{eff}}{\mathrm{T}_{\mathrm{eff},\odot}}\right)^{3/2} \tag{1.7}$$

$$\frac{R}{\mathrm{R}_\odot} = \left(\frac{\nu_\mathrm{max}}{\nu_{\mathrm{max},\odot}}\right) \left(\frac{\Delta\nu}{\Delta\nu_\odot}\right)^{-2} \left(\frac{T_\mathrm{eff}}{\mathrm{T}_{\mathrm{eff},\odot}}\right)^{1/2} \tag{1.8}$$

These relations are the most used scalings to estimate the stellar radius and mass through the analysis of the oscillation pattern. Using (1.7), it is possible to estimate the mass of stars in the low-luminosity portion of the RGB and the mass of stars on the red clump. The difference between these two values provides an estimate of the integrated mass loss ΔM along the RGB.

However, it has to be noted that a direct application of (1.7) does not yield accurate mass estimates. For instance, this argument was discussed by Miglio, Chiappini, et al. (2021) on the study of the coeval α-rich population in the Milky Way, observed by *Kepler*. Stellar masses are estimated with a direct application of asteroseismic scaling relations involving ν_max and the average large frequency spacing $\langle\Delta\nu\rangle$ (see blue histograms in figure 1.5). Instead, the red histograms show the results with $\langle\Delta\nu\rangle$ corrected on the basis of theoretical models. As can be seen in figure 1.5, the latter inferred mass distributions have a considerably better match with the predictions from simulations. Indeed, the application of scaling relations without corrections to $\langle\Delta\nu\rangle$ leads to systematically higher estimates of the mass (see for instance the study of Brogaard et al. 2018 on a comparison between seismically-inferred and independent mass estimates of three red giants belonging to three different eclipsing binary systems).

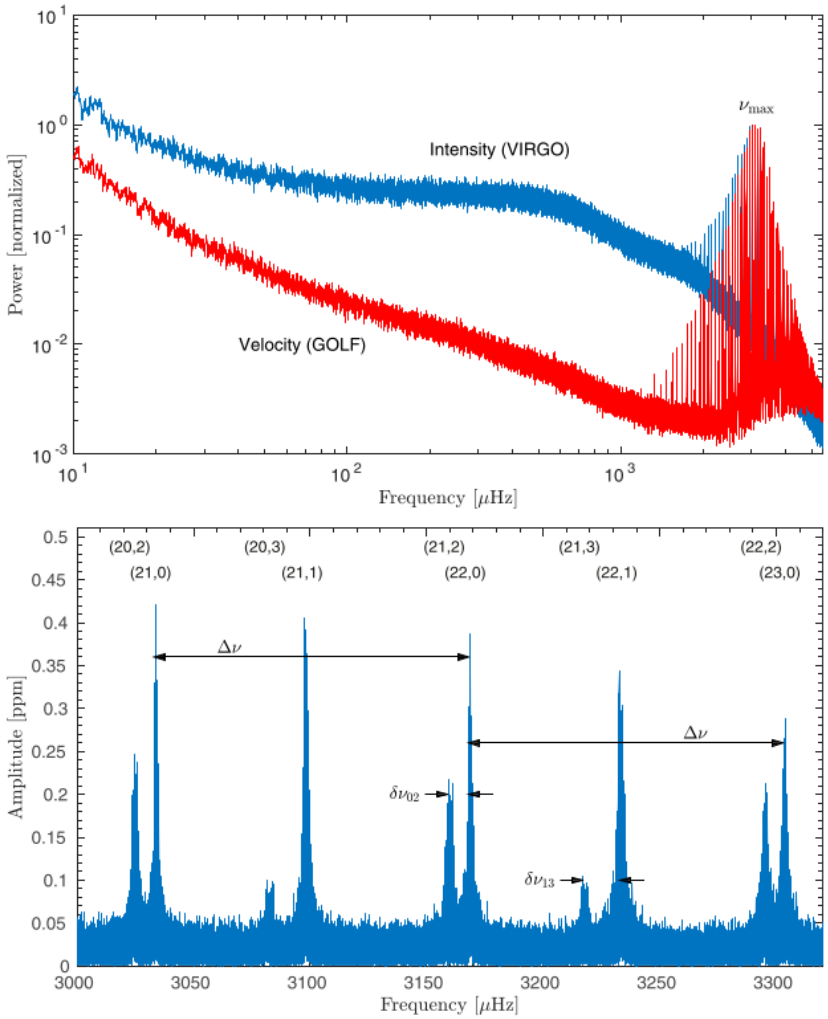

Figure 1.3: *Taken from figure 1 in Jackiewicz (2021). Top panel*: Solar power spectra obtained with VIRGO (by analyzing radial velocity fluctuations) and GOLF (from intensity variations). Both the instruments were on board of the SOHO satellite. Spectra are normalized such that the amplitudes are equal near the frequency of maximum amplitude $\nu_{\rm max} \simeq 3090\,\mu$Hz. *Bottom panel*: Amplitude spectrum computed from the VIRGO photometric data near $\nu_{\rm max}$. The peaks are labeled by their radial order n and angular degree l as (n, l). Few characteristic frequency spacings are shown, $\Delta\nu$ are the large spacings and $\delta\nu$ the small ones.

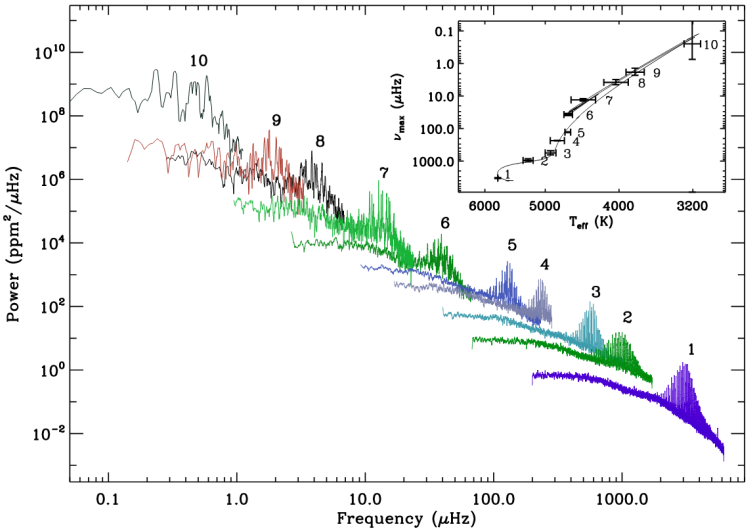

Figure 1.4: *Taken from figure 1.3 in García and Stello (2015).* Sample of power spectral density for stars with mass $M \simeq 1\,\mathrm{M}_\odot$ presenting solar-like oscillations, spanning from main sequence to RGB tip. Numbers range from 1 to 10, where 1 is the Sun and 10 corresponds to a star at the RGB tip. The number 6 is a red clump star. The inset is a seismic HR diagram ($\nu_{\max}$ is reported in the vertical axis), where the solid line is the evolutionary track of a $1\,\mathrm{M}_\odot$ star computed with MESA. The position of each star is shown as a point labeled with the corresponding number. The 1σ error bars in $\nu_{\max}$ are multiplied by a factor of 10.

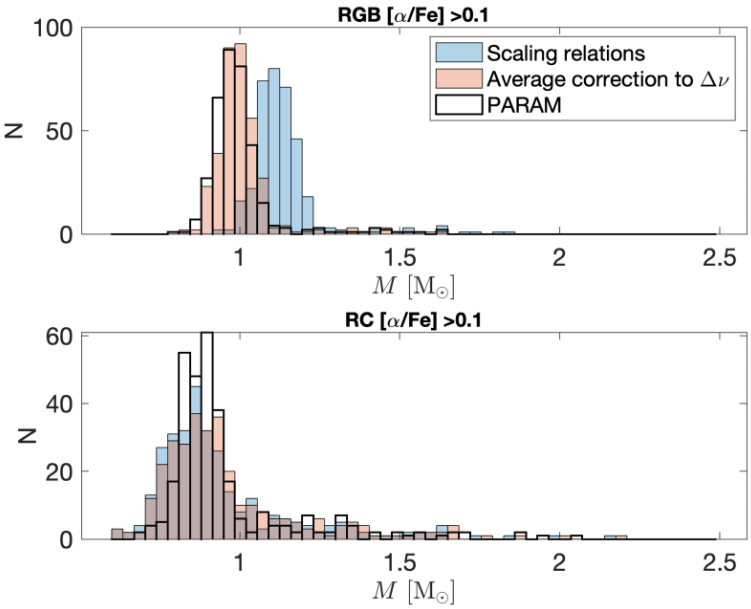

Figure 1.5: *Taken from figure 14 in Miglio, Chiappini, et al. (2021).* Mass distribution of stars with $[\alpha/\mathrm{Fe}] > 0.1$. The histograms contoured with the thick black line represent the mass distribution predicted by the code PARAM.

1.2 Modelling mass loss

In section 1.1, I presented the most important methods used to infer either the total integrated mass loss in stellar populations or the mass loss rate of individual objects. From an observational point of view, considering the variety of independent methods and the possibility of studying mass loss in both individual stars and stellar populations of different nature, we can say that a remarkable progress has been achieved. Unfortunately, the same cannot be said for our understanding of the actual physical mechanisms which cause mass loss. Our understanding of these processes is still largely unknown, as I will explain in the following sections.

1.2.1 Reimers' mass loss

A pivotal review by Reimers (1975) summarized all the different methods used to infer mass loss rates that were known at that time. Reimers collected all the estimated mass loss rates obtained with independent techniques and used them to propose a relation where the rate of mass loss depends on global stellar parameters. The physical argument at the basis of this prescription is notably simple and basically consists in a dimensional argument: Reimers suggested that the mass loss rate $\dot{M}$ should be a function of the stellar parameters which determine the structure of stellar atmospheres and envelopes. Therefore, $\dot{M}$ should depend on surface gravity g, effective temperature $T_{\rm eff}$, radius R and chemical composition. Rotation, magnetic fields, chromospheric activity, and pulsation were also mentioned as further quantities with possible influence on mass loss. Reimers considered the simplest quantity of dimension $\mathrm{g\,s^{-1}}$ that can be formed from basic stellar parameters, which is L/gR (where L is the luminosity). Then, he searched for a correlation between the measured mass loss rates and the quantity L/gR, which can be seen in figure 1.6.

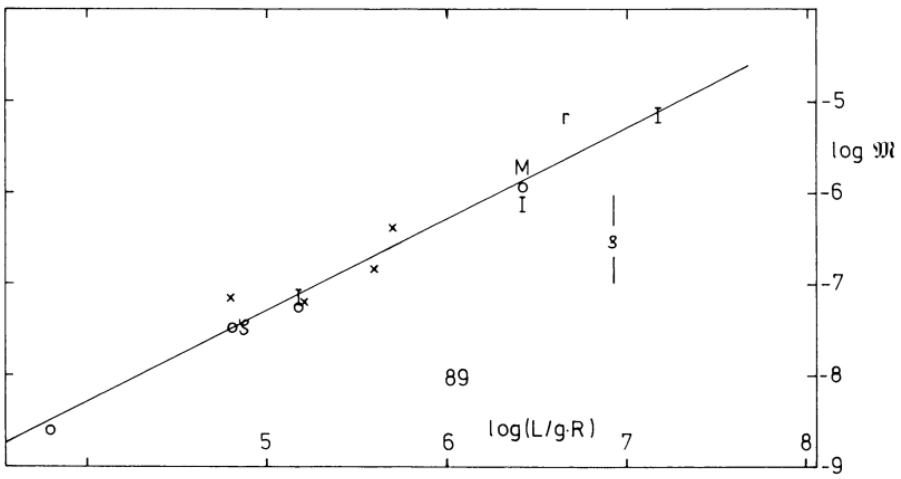

Figure 1.6: *Fig.7 in Reimers (1975)*: observed $\log|\dot{M}|$ (expressed in $\mathrm{M_\odot\,yr^{-1}}$) versus $\log(L/gR)$ (in solar units). Different symbols refer to mass loss rates obtained from independent studies. The sample only includes population I red giants. The solid line represents the relation reported in equation (1.9).

The empirical mass loss rates could be represented quite well by the relation:

$$\left(\frac{\dot{M}}{\mathrm{M}_\odot\,\mathrm{yr}^{-1}}\right) = -4\times10^{-13}\frac{L/\mathrm{L}_\odot}{(g/\mathrm{g}_\odot)(R/\mathrm{R}_\odot)} \tag{1.9}$$

We can consider the definition of escape velocity $v_{\mathrm{esc}} = \sqrt{2gR}$ in equation (1.9) and rearrange it as:

$$\frac{1}{2}\dot{M}v_{\mathrm{esc}}^2 = -2\times10^{-6}L \tag{1.10}$$

Equation (1.10) reveals an idealized physical analogy that can be associated to the observed mass loss rates. Suppose an idealized framework in which mass ejection consists of material moving from the stellar surface to infinity. If the gas stops at infinity, matter leaves the surface at the escape velocity v_{esc}. Now, if we assume that the energy source powering the outflow is a fixed fraction of the total luminosity, the conservation of mechanical energy would exactly reduce to an equation of the same form as (1.10). This result indicates that $\dot{M}$ depends on stellar parameters in the same manner as the idealized scenario where, for *all* stars, a fixed fraction of the stellar luminosity is used to expel matter from the surface, at the escape velocity. This constant fraction is of the order of 10^{-6}, as can be seen in equation (1.10).

Another interesting result found by Reimers is the correlation between the infrared silicate excess and the ratio L/gR, as can be seen in figure 1.7. The infrared silicate excess is an indicator of the amount of dust contained in the circumstellar envelope, since it is the color index obtained by computing $(3.5) - (11.4)$, where the former is the magnitude at $3.5\,\mu$m and the latter is the magnitude at $11.4\,\mu$m. A high value of $(3.5) - (11.4)$ indicates a dust excess in the circumstellar envelope. This result is indicative of the fact that dust might be connected with mass loss processes (see section 1.2.3 for further discussions).

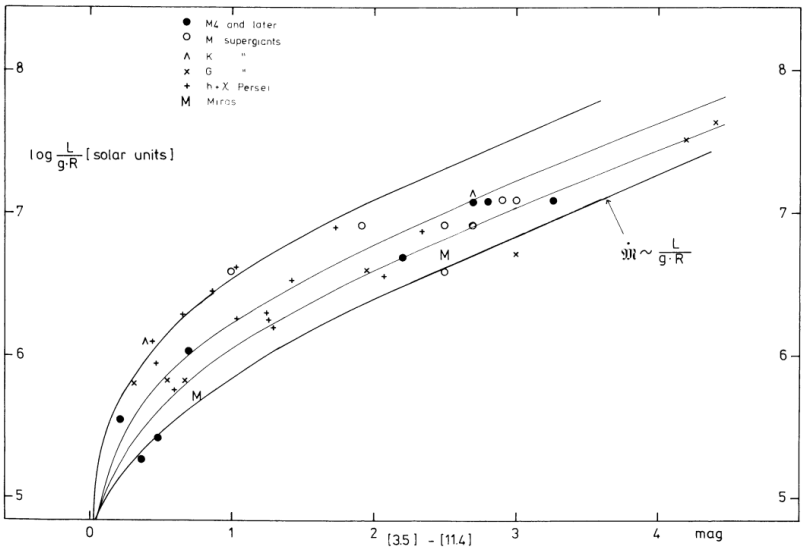

Figure 1.7: *Fig.8 in Reimers (1975)*: $\log(L/gR)$ (in solar units) versus infrared silicate excess (3.5) - (11.4). Different symbols refer to different sources. The solid lines are theoretical silicate excesses computed by assuming $\dot{M} \propto L/gR$.

Up to 1975, there was no direct measurement of mass loss in population II stars and the sample used to obtain the empirical law (1.9) consisted of PopI red giants.

However, still Reimers (1975) suggested that the same relation could also hold for PopII. In fact, Heasley and Mengel (1972) computed total mass losses up to the RGB tip on the basis of equation (1.9). The calculation for a PopII star with initial mass $0.85\,\mathrm{M}_\odot$ yielded an integrated mass loss of $\Delta M = 0.2\,\mathrm{M}_\odot$, which is consistent with the observational constraint found by Rood (1973) in the CMD of globular clusters. Therefore, it is plausible that the mechanism powering mass loss is the same in PopI and PopII stars, unless the latter lose a relevant fraction of their mass in a very rapid evolutionary phase (e.g. the helium flash).

The main limitation of relation (1.9) was already recognized by Reimers: this mass loss prescription must be intended as a semi-empirical law, where it was taken the simplest functional dependence on global stellar parameters giving the dimension of a mass loss rate. There are no solid physical arguments behind this relation and none of the complex processes which could influence mass ejection were considered.

1.2.2 Applications and limitations of the Reimers' law

It was soon realized that equation (1.9), integrated along the RGB for globular cluster stars, would predict too much mass loss. Stars would lose the whole envelope before reaching the RGB tip. For this reason, an efficiency parameter η_R was introduced:

$$\left(\frac{\dot{M}}{\mathrm{M}_\odot\,\mathrm{yr}^{-1}}\right) = -4\times10^{-13}\eta_\mathrm{R}\frac{L/\mathrm{L}_\odot}{(g/\mathrm{g}_\odot)(R/\mathrm{R}_\odot)} \tag{1.11}$$

where η_R is a free parameter, typically assumed to be constant. By adopting $\eta_\mathrm{R} \simeq 0.3 - 0.4$, equation (1.11) could match the integrated mass loss constrained by the HB morphology in globular clusters. Moreover, with the same values of η_R, stars lose an additional $\sim 0.1\,\mathrm{M}_\odot$ along the asymptotic giant branch (AGB). In this way, also the lack of very bright AGB stars in globular clusters could be explained. This is the main success of the Reimers' law: though being relatively simple, it can simultaneously reproduce the HB and AGB extensions in globular clusters, by adopting similar values for η_R (Greggio and Renzini 2011). In the past, observational constraints on mass loss were not precise enough to test different mass loss prescriptions and Reimers' law has remained the main reference in stellar models for the past decades. However, there are various indications which clearly suggest that Reimers' mass loss rate (1.11) fails in reproducing other aspects of both AGB and RGB mass loss. For the former, I follow the review by Greggio and Renzini (2011).

- **Limitations of the Reimers' law for AGB mass loss.**
  Equation (1.11) used for AGB stars with masses $4\,\mathrm{M}_\odot \lesssim M \lesssim 8\,\mathrm{M}_\odot$ wrongly predicts that such stars would not experience enough mass loss and their cores would reach the Chandrasekhar limit, thus exploding due to the onset of a thermal runaway process triggered by carbon ignition, typical of type Ia supernovae. This is well refuted by two observational facts: first, the fact that a significant fraction of AGB stars would reach the Chandrasekhar limit would imply the existence of very luminous AGB stars ($L \sim 50000\mathrm{L}_\odot$). The first observations on the Magellanic Clouds showed instead that the brightest AGB stars reach luminosity of the order of $\sim 15000 - 20000\mathrm{L}_\odot$. Secondly, in the current sample of observed supernovae, there is no event that can be attributed to carbon detonation occurring inside a hydrogen-rich envelope. Moreover, the properties of planetary

nebulae (PNe) are suggestive of tremendous mass loss in very advanced stages of the AGB. The typical mass, velocity and radius of PNe are $\sim 0.2\,M_\odot$, $\sim 0.1\,M_\odot$ and $\sim 20\,\mathrm{km\,s^{-1}}$, respectively. Therefore, the typical rate which produces the PN shell is of the order of $10^{-5}\,M_\odot\,\mathrm{yr}^{-1}$, a factor of ~ 10 larger than predicted by (1.11).

- **Limitations of the Reimers' law for RGB mass loss.**
With recent and precise observational constraints coming from asteroseismic techniques, we are now demonstrating that Reimers' prescription does not work, if a single free parameter η_R is assumed. K. Brogaard et al. (2024) compared different estimates of integrated mass loss on different stellar populations (see figure 1.8). We can see that different efficiency factors η_R must be considered to account for the estimated ΔM measured in different stellar populations. This clearly suggests that Reimers prescription is not able to simultaneously explain RGB mass loss for stars belonging to different environments.

  Another puzzling question is the dependence on metallicity. If we stick to the Reimers' law, we can clearly see that an increasing metallicity should imply higher mass loss rates along the RGB. This is due to two reasons:

  - at fixed luminosity, more metal-rich stars are generally bigger, which implies a lower surface gravity. Other things being equal, this would mean a higher mass loss rate (see equation 1.11);
  - metallicity has also an impact on the extension of the RGB: at increasing metallicity, the RGB tip occurs at higher luminosities. Thus, there would be an additional phase of the evolution where the magnitude of the mass loss rate would further increase (indeed, it is the phase right before the tip where the absolute value of $\dot{M}$ is the highest, at least in the Reimers' prescription).

  Mass-loss estimates in GCs suggest that mass loss increases with metallicity, consistent with the general behaviour predicted by the Reimers' law and other mass loss prescriptions. However, there are new indications that mass loss could instead be a decreasing function of metallicity, as claimed by K. Brogaard et al. (2024) on the α-rich population of MW field stars and recently by Li (2025) on a sample of *Kepler* red giants. Some suggestions have now been proposed about the possibility that mass loss could first be an increasing function of metallicity, then decreasing after some specific threshold in [Fe/H].

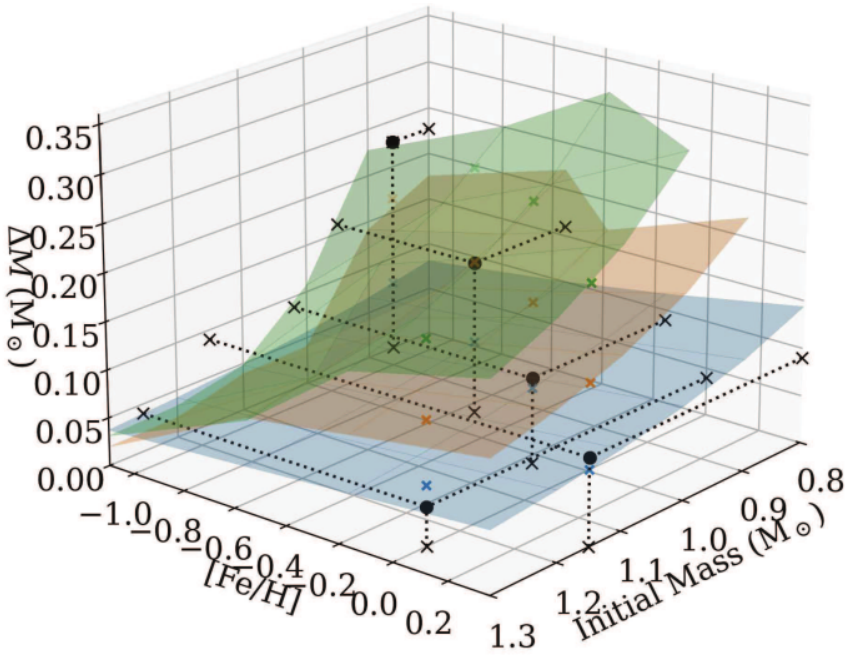

Figure 1.8: *Fig.5 in K. Brogaard et al. (2024)*: Comparison between observational estimates of integrated RGB mass loss in different populations to that predicted by the Reimers' law (blue: $\eta_R = 0.2$, orange: $\eta_R = 0.4$, green: $\eta_R = 0.6$). The black dots represent the inferred integrated mass loss by using asteroseismic techniques. Moving along the [Fe/H] axis, from left to right, the following integrated mass loss estimates are shown: the GC M4 inferred by Tailo et al. (2022); two sub-populations of field stars belonging to the α-rich sequence of the MW, inferred by K. Brogaard et al. (2024); the open cluster M67, inferred by Stello et al. (2016) and the old open cluster NGC 6791, inferred by Miglio, K. Brogaard, et al. (2012).

1.2.3 Radiatively-driven vs thermal winds

The growing number of difficulties in explaining the observational evidence with the current modelling is a sign of the poor understanding of RGB mass loss mechanisms. Among the theories which have focused on mass loss as a steady process, we can distinguish two main "families": radiation pressure on dust grains and dissipation of energy (e.g., mechanical or magnetic) which heats the stellar chromosphere/corona, leading to gas evaporation. In this paragraph, I introduce both these two processes.

- **Radiation pressure on dust grains**
  The correlations found between mass loss and dust infrared emission already mentioned in sections 1.1.1 and 1.2.1 suggested that mass loss in cool giants could be connected with circumstellar dust envelopes. The work done by Gehrz and Woolf (1971) is one of the first proposing a possible mechanism where dust grains could originate gas outflows. The idea consisted in the fact that dust particles — *condensed* in solid form — could be accelerated by pressure exerted by stellar photons. This condensation can occur if two conditions are satisfied: first, stellar photons should not be too energetic, otherwise the dust temperature would be too high; secondly, the gas density should instead be high, otherwise the vapor pressure on dust would be too low. The first condition is not satisfied in the photospheric layers or below, so the formation of dust grains must necessarily

occur on a region well above the photosphere. To satisfy both conditions, dust condensation must occur in much extended stellar atmospheres and RGB stars close to the tip were thought to be compatible with this scenario. The onset of the outflow was described as follows: when dust grains form, radiation pressure rapidly accelerates them up to a terminal velocity and, after this point, further momentum imparted to the dust would accelerate the surrounding gas.

Another reason why radiation pressure on dust has been considered as a promising scenario is the fact that mass loss in massive hot stars can be well described by gas outflows powered by radiation pressure (Greggio and Renzini 2011). In fact, gas acquires momentum from photons thanks to resonant absorptions. The mass loss rate predicted by theory well matches with observations of hot massive stars and with nuclei of planetary nebulae. The success of radiatively-driven winds for hot stars suggested that similar mechanisms could be occurring in cool giants.

While it is clear that dust and mass loss are certainly connected, their exact interplay is still not properly established. We are still not sure whether dust drives winds or it is formed within them (Greggio and Renzini 2011). Moreover, if mass loss was fully determined by dust, we would observe a very strong increase of mass loss with metallicity, due to the higher abundance of elements forming dust. This strong trend is not observed, since there are also indications of a decreasing ΔM with increasing [Fe/H] (see section 1.2.2). On the other hand, the estimates of the integrated mass loss in GCs do not show a strong increase of ΔM with [Fe/H]: it is $\sim 0.2\,\mathrm{M}_\odot$ for metal-poor GCs ([Fe/H] $\simeq -2.3$), whereas the upper limit for metal-rich GCs ([Fe/H] $\simeq 0$) is $\Delta M \sim 0.3\,\mathrm{M}_\odot$ (Greggio and Renzini 2011).

- **Thermal winds**
  Another idea around which a huge amount of literature has been produced since the early '60s is based on the hypothesis that RGB mass loss is due to *thermal winds*, similar to what is observed in the Sun. Theories that have tried to explain RGB mass loss under this assumption share the fundamental idea that some kind of energy input dissipates in the outer atmosphere of red giants. This leads to heating of chromospheric and/or coronal gas, thus favouring evaporation. The physical processes of dissipation are very complicated, and quantitative predictions are still not possible, not even for the Sun.

  For this reason, there is no solid theory describing mass loss from RGB stars as a thermal wind. However, it is still important to keep on studying this hypothesis, since only radiation pressure on dust cannot explain the observed mass-loss estimates, as explained above. Moreover, the recent developments in both observations and simulations are motivating us to search for a better understanding of the physical quantities which could drive thermal winds. In the light of these reasons, this project focuses on mass loss mechanisms belonging to the "family" of thermal winds.

Chapter 2

Stellar Winds as Steady Evaporative Processes

2.1 Classical hydrodynamic theories of stellar winds

Weymann (1963)'s review is a useful reference to understand the main properties of the classical hydrodynamic theories of mass loss. In this paragraph, I refer to such review, in order to introduce the main properties of these models, with a particular emphasis on isothermal flows, whose solutions were discussed by Parker (1958) as a possible description of the solar wind. Most of these theories were developed on the basis of the following assumptions:

a. Matter moves out under an inverse-square gravitational field;

b. The flow is spherically symmetric and everywhere steady in time;

c. Viscous forces are negligible;

d. The pressure tensor is isotropic;

e. Gas pressure and gravity are the only agents exerting forces on the gas.

Under these assumptions, the hydrodynamic equations governing the flow are:

$$\rightarrow \text{mass conservation:} \quad \frac{1}{r^2}\frac{\mathrm{d}(r^2\rho V)}{\mathrm{d}r} = 0 \tag{2.1}$$

$$\rightarrow \text{Euler equation:} \quad \frac{\mathrm{d}}{\mathrm{d}r}\left(\frac{V^2}{2}\right) = -\frac{1}{\rho}\frac{\mathrm{d}P}{\mathrm{d}r} - \frac{GM}{r^2} \tag{2.2}$$

$$\rightarrow \text{energy equation:} \quad V\left(\frac{\mathrm{d}X}{\mathrm{d}r} + \frac{3}{2\rho}\frac{\mathrm{d}P}{\mathrm{d}r} - \frac{5P}{2\rho^2}\frac{\mathrm{d}\rho}{\mathrm{d}r}\right) = \frac{\mathrm{d}Q}{\mathrm{d}t} \tag{2.3}$$

where ρ is the gas density; V is the radial velocity; P is the gas pressure and M is the mass enclosed within the radius r. The quantity X refers to any extra internal energy of the gas besides that due to translational motion of particles. $\frac{\mathrm{d}Q}{\mathrm{d}t}$ is the rate of heat flow into the gas, per unit mass and per unit time (it is negative if the gas loses energy). This term involves three types of heat gain or loss: absorption and/or emission of radiation; energy exchange due to thermal conduction and from convective motion within the flow; dissipation of mechanical energy, that is conversion of energy

of organized motion (e.g., acoustic waves, shocks, hydromagnetic waves) into thermal energy.

Let us now focus on isothermal winds (i.e., the temperature of the outflowing gas is assumed to be everywhere constant, due to heating mechanisms). Under this assumption, by using the equation of state for a perfect gas and the mass conservation equation (2.1), the Euler equation can be written as:

$$V\frac{\mathrm{d}V}{\mathrm{d}r} = \frac{k_\mathrm{B}T_0}{\mu m_\mathrm{p}}\left(\frac{1}{V}\frac{\mathrm{d}V}{\mathrm{d}r} + \frac{2}{r}\right) - \frac{GM}{r^2} \tag{2.4}$$

where T_0 is the uniform temperature of the wind, μ is the molecular mean weight (assumed to be constant). Equation (2.4) can eventually be solved to obtain $V(r)$, if an initial condition to the wind velocity is provided. We can introduce the set of dimensionless variables:

$$\xi \equiv \frac{r}{r_0} \quad ; \qquad \psi \equiv \frac{\frac{1}{2}m_\mathrm{p}V^2}{k_\mathrm{B}T_0} \quad ; \qquad \lambda \equiv \frac{GMm_\mathrm{p}}{r_0 k_\mathrm{B}T_0} \tag{2.5}$$

which are used to write equation (2.4) in a much more compact form:

$$\psi' = \frac{2\mu\psi\left(\dfrac{2\xi}{\mu} - \lambda\right)}{2\mu\psi - 1} \tag{2.6}$$

where $\psi' \equiv \xi^2\frac{\mathrm{d}\psi}{\mathrm{d}r}$. Equation (2.6) allows us to qualitatively understand the character of the solutions, depending on the initial condition on ψ. If we focus on winds starting with low velocities, the denominator at the RHS of equation (2.6) is negative. Therefore:

$$\psi'(\xi) \geq 0 \text{ for } \xi \leq \frac{\mu\lambda}{2} \quad ; \qquad \psi'(\xi) < 0 \text{ for } \xi > \frac{\mu\lambda}{2} \tag{2.7}$$

which is the behaviour sketched in figure 2.1. The asymptotic behaviour for $\xi \to \infty$ is $\psi \propto \xi^{-4}$, which is equivalent to say that the wind velocity decreases as $V \propto r^{-2}$.

Now, suppose we increase the initial velocity of the wind. For some specific initial conditions, at $\xi = \frac{\mu\lambda}{2}$, the normalized kinetic energy reached by the wind can be $\psi = \frac{1}{2\mu}$. In this special case, the wind does not decelerate and the velocity continues to grow for $\xi > \frac{\mu\lambda}{2}$, thus becoming supersonic. Solutions of this kind are named *critical solutions*: they are the only ones where the wind starts at a subsonic speed and gets accelerated up to supersonic velocities at larger distances. For the critical solutions of the isothermal model, the asymptotic behaviour of the wind velocity is $V \propto \sqrt{\ln\xi}$, for $\xi \to \infty$.

The Parker's isothermal model (Parker 1958) has equivalent solutions to those which I have just described. In the years that followed, he also developed more advanced models, in which a decreasing temperature with distance was considered. However, the main result remained the same: only the critical solution is able to satisfy physically plausible boundary conditions — large densities, large kinetic pressure and low bulk velocities at the base of the corona, together with low densities, low pressure and high bulk velocities at infinity.

Though being quite idealized, the Parker's model was able to predict the main properties of the *solar* wind. For instance, it predicted the supersonic wind velocity at a distance of 1 astronomical unit from the Sun and it inspired further theoretical work, not only on the solar wind itself, but also on other plasma flows.

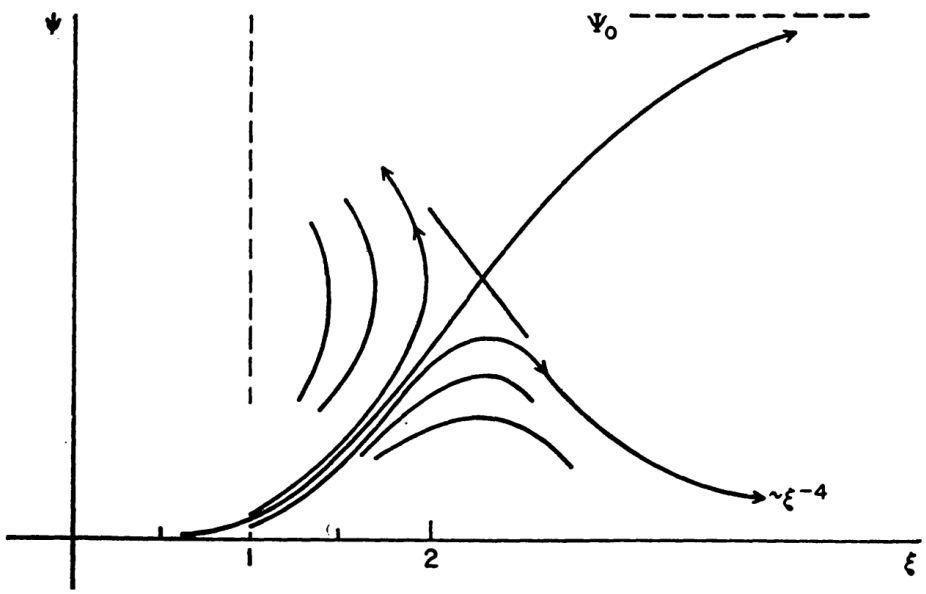

Figure 2.1: *Fig.3 in Weymann (1963)*: Sketch of the isothermal solutions for $\psi(\xi)$, corresponding to different initial conditions for the wind velocity. The solution passing through the point $\psi = \frac{1}{2\mu}$ and $\xi = \frac{\mu\lambda}{2}$ is one of the critical solutions.

2.2 Weymann's model for coronal evaporation in red giants

Given the success of the Parker's hydrodynamical model in describing some observed properties of the solar wind, it was suggested that RGB mass loss could be driven by similar mechanisms. The work done by Weymann (1960) pointed towards this direction: the aim was to build a hydrodynamical model for coronal evaporation, specifically for red giant stars. The author considered the *mechanical energy of acoustic waves* — generated by turbulent convection — as a candidate energy input of the wind. Indeed, it was suggested that heating of the coronal gas could be driven by dissipation of acoustic waves, at the base of the corona. As already mentioned at the end of section 1.2.3, the evaporation of the heated gas would be the nature of the stellar wind. The main result of Weymann's work was that only supersonic flows could produce mass loss rates that are relevant from an evolutionary point of view. In this paragraph, I will present the most crucial points which led the author to this conclusion.

To justify the hypothesis that acoustic energy might be the source of mass ejection, Weymann (1960) proposed the following reasoning. He considered α Herculis as a reference (concerning mass loss, it was the best-studied supergiant at that time) and, from its global parameters, he stated that a "significant" mass loss rate would be of $\sim 1.6 \times 10^{-7}\,\mathrm{M}_\odot\,\mathrm{yr}^{-1}$ or higher. By "significant", the author meant a mass loss rate which is equal or higher than the rate at which hydrogen is converted into helium. Such a rate would require a fraction of $\sim 8 \times 10^{-6}$ of the total luminosity, to sustain mass ejection. Thanks to measures of turbulent velocities in the photosphere of the Sun and other stars, it was known that the ratio of acoustic to radiative flux was constant and about 0.01. Therefore, the acoustic energy could meet the energy requirement by a factor of over 1000. However, as Weymann noted, this estimate does not account for potential dissipation of acoustic waves deeper down in the stellar chromosphere.

Nonetheless, acoustic energy was considered as a sufficient energy source to sustain the wind.

The physical assumptions at the basis of Weymann (1960)'s analysis are:

- the mechanical energy is deposited in a thin layer above the surface, so beyond some point (not very far above the surface of the star), there is no significant deposition of mechanical energy. In other words, the dissipative processes are assumed to occur on a thin layer above the surface of the star and there is no further dissipation of mechanical energy on larger distances;

- at the base of the corona, the gas is assumed to have a density around 10^{-16} - $10^{-15}\,\mathrm{g\,cm^{-3}}$ and to be heated up to a temperature in the range 10^5 - $10^6\,\mathrm{K}$. These were the typical known conditions of chromospheric/coronal gas for the Sun.

- the assumptions on the flow are the same as those reported at the beginning of section 2.1. Therefore, the hydrodynamic equations are exactly (2.1), (2.2) and (2.3).

To obtain the differential equation for the wind velocity, it is possible to eliminate the pressure and density derivatives in the energy equation (2.3) by using equations (2.1) and (2.2). After some manipulation, it is possible to obtain:

$$\frac{\mathrm{d}V}{\mathrm{d}r} = \frac{1}{c_\mathrm{s}^2(\mathcal{M}^2-1)}\left[V\left(\frac{2c_\mathrm{s}^2}{r}-\frac{GM}{r^2}\right)-(\gamma-1)\frac{\mathrm{d}Q}{\mathrm{d}t}\right] \tag{2.8}$$

where γ is the specific heat ratio, $\mathcal{M} \equiv V/c_\mathrm{s}$ is the Mach number and c_s is the sound speed, defined as:

$$c_\mathrm{s}^2 \equiv \gamma\frac{P}{\rho} \tag{2.9}$$

Two interesting properties can already be found in equation (2.8):

- An energy loss ($\frac{\mathrm{d}Q}{\mathrm{d}t} < 0$) decelerates the flow, if it moves at subsonic velocities ($\mathcal{M} < 1$); on the contrary, it accelerates the flow if the motion is supersonic ($\mathcal{M} > 1$). The opposite effects hold in the presence of an energy gain ($\frac{\mathrm{d}Q}{\mathrm{d}t} > 0$);

- If the wind starts at subsonic speeds, it cannot be accelerated to supersonic velocities, unless some specific initial conditions to the wind velocity makes the term between square brackets vanish at the exact position where $\mathcal{M} = 1$. These are the so-called critical solutions, which were already discussed in section 2.1 for the isothermal model.

Within the framework of the Weymann's analysis, for reasons that will not be addressed in this work, radiation loss is the dominant factor contributing to $\frac{\mathrm{d}Q}{\mathrm{d}t}$ in equation (2.8), since it is more important than conduction and convection terms. Therefore, only radiation losses were considered in the term $\frac{\mathrm{d}Q}{\mathrm{d}t}$. To this aim, the author studied two limiting cases: an upper limit to radiation loss was given by assuming that there is no energy gain by photoionization and all de-excitations are radiative, rather than collisional; the case with the weakest radiation loss was instead set by assuming that only free-free and free-bound emission of hydrogen and helium are important, other cooling processes being compensated for by radiative absorption and collisional de-excitation.

The former case was referred to as "strong" and the latter as "weak" radiation-loss assumptions. Weymann performed numerical integrations of equations (2.1), (2.2) and (2.8) in both the limiting cases. Concerning initial conditions, he performed the computation using a grid of initial temperatures T_0 ranging from 10^5 K to 10^6 K and initial Mach numbers $\mathcal{M}_0 = 0.1 - 1.5$. Figures 2.2a and 2.2b show some examples of the solutions for subsonic flows and supersonic flows, respectively (see solid lines). The adiabatic solutions (dashed lines) were also reported by Weymann, for comparison.

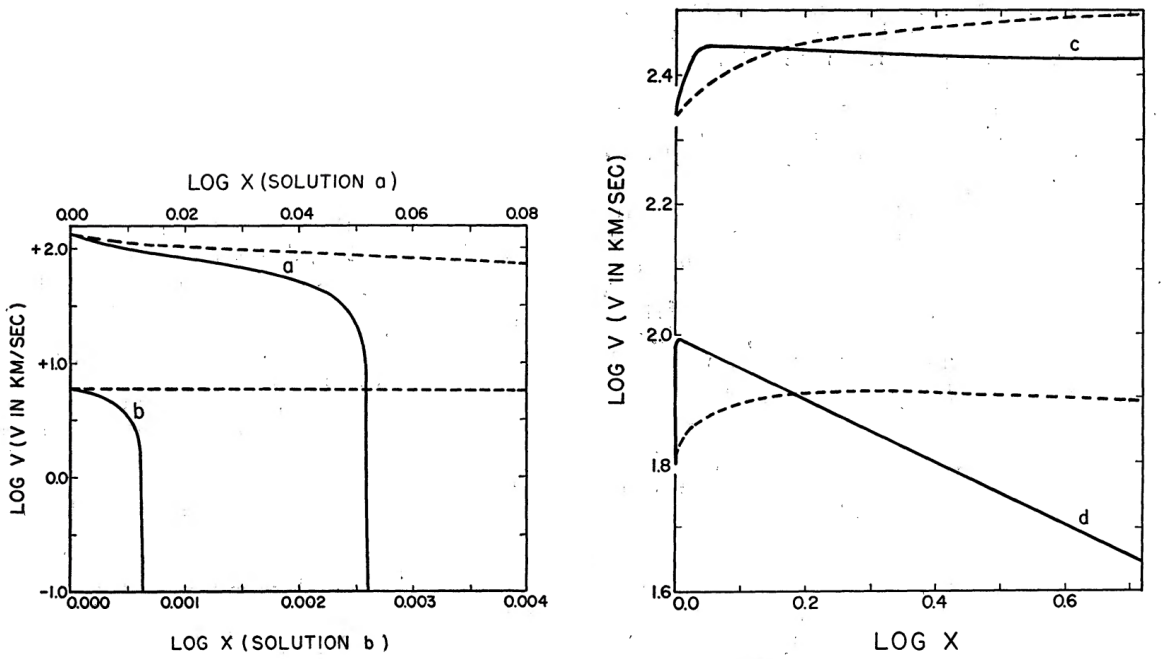

(a) *Fig. 3A in Weymann (1960)* (b) *Fig. 3B in Weymann (1960)*

Figure 2.2: *Left panel.* Wind radial velocity as a function of the distance normalized to the radius at the base of the flow ($x \equiv r/r_0$), for subsonic flows. The solid lines refer to non-adiabatic solutions, under the weak radiation-loss assumption (see text for details); the dashed curves are adiabatic solutions, whose properties are not addressed in this work. The solution "a" has initial conditions $\mathcal{M}_0 = 0.9$ and an initial temperature T_0 chosen so that the ratio between the potential energy and the thermal energy at the base of the flow (i.e., at $\log x = 0$) is 0.12. The solution "b" has initial conditions $\mathcal{M}_0 = 0.1$ and a gravitational over thermal energy ratio of 0.73 at $\log x = 0$. The initial density is $\rho_0 = 10^{-16}\,\mathrm{g/cm^3}$ in both cases.
Right panel. As in panel (a), but for supersonic flows. The non-adiabatic solutions are computed using the strong radiation-loss assumption. The solution "c" has initial conditions $\mathcal{M}_0 = 1.5$ and the ratio between the potential energy and the thermal energy at $\log x = 0$ is 0.12. The solution "d" has initial conditions $\mathcal{M}_0 = 1.03$ and a gravitational over thermal energy ratio of 0.65, at $\log x = 0$. The initial density is $\rho_0 = 10^{-16}\,\mathrm{g/cm^3}$ in both cases.

Due to the presence of the radiation-loss term, both the subsonic and supersonic flows are characterized by a sharp drop in temperature on the earliest phase of the flow. However, the kinetic energy behaves very differently:

- as expected from equation (2.8), the radiation-loss term decelerates the gas in the case of subsonic flows (see figure 2.2a). Therefore, almost all the initial energy

of the gas is lost through the emission of radiation and it cannot escape further out;

- the opposite happens for supersonic flows. Here, the inner region of the flow is characterized by a sharp increase of the kinetic energy, caused by radiation losses. If the gas was initially accelerated to sufficiently high velocities, it can be further pushed by the steep pressure gradient, eventually escaping from the star (see solution "c"). Other solutions with an initial Mach number just slightly above 1, and a lower initial temperature, may instead be too slow to be further pushed by the pressure gradient. Weymann suggested that the solution "d" could be close to the limit below which flows cannot be pushed away from the star.

In the light of these results, Weymann concluded that only supersonic solutions could eventually be acceptable as a possible explanation for mass loss in red giant stars. In other words, if coronal evaporation was the mechanism originating mass loss, supersonic flows would be the only solutions predicting significant wind velocities, extending further out from the star. However, except for some specific solutions (such as "d"), the calculated velocity of the wind was predicted to be of the order of $50 - 100$ $\mathrm{km\,s^{-1}}$, well above the estimated $10 - 25$ $\mathrm{km\,s^{-1}}$ from the observations on α Herculis, done by Deutsch (1956) and Deutsch (1960). This result led Weymann to *reject* this coronal evaporation model as a potential explanation of mass loss in red giants. In the next section, I will summarize further problems of classical thermal wind theories of mass loss, as well as the various difficulties encountered in modelling such phenomena.

2.3 Limitations of classical thermal wind models

In his review, Weymann (1963) pointed out that a temperature of $\sim 10^5$ K at the base of the corona would lead to strong emission lines (such as Hα lines), which were not observed in the spectra of circumstellar envelopes. Moreover, a primary difficulty was still finding a physical process able to simultaneously explain the heating of gas and the relatively small widths of the circumstellar lines, indicative of a *cold* wind. As already mentioned, dissipation of acoustic waves was considered as one of the best candidates, but it was hard to imagine which precise physical process could explain both the coronal gas heating and the overall low temperature of the winds. Secondly, the role of magnetic fields: besides dissipation of acoustic energy, also magnetohydrodynamic (MHD) waves carry some energy that in principle could dissipate, thus contributing to power the wind. This problem was not addressed at all, since the knowledge on magnetic field strengths and configuration in red giant stars was still at a very rudimentary state in the early '60s. However, it was clear already in those years that dissipation of acoustic waves is probably not the only mechanism which drives mass loss.

In the years that followed, many different models including dissipation of MHD waves were developed and it was shown that dissipation of acoustic waves is surely not enough to entirely account for a steady mass loss from giant stars. For instance, Hartmann and MacGregor (1980) showed that the shocks generated by the steepening of sound waves dissipate over too short lengthscales, of the order of few pressure scale heights. Since this damping lengthscale sets the region where waves are effective in accelerating the flow, the dissipation of acoustic energy alone was discarded as a plausible origin of stellar winds, except for the stars with the lowest surface gravity. The

role of acoustic waves and the shocks generating from them might then be extending the hydrostatic portion of the lower atmosphere, rather than driving a steady stellar wind. On the contrary, it was shown that dissipation of Alfvén waves might create stellar outflows with mass loss rates compatible to the observational estimates.

It is now widely accepted that magnetic fields play a crucial role in mass loss processes, but the exact physical mechanisms are still matter of study. Indeed, many different heating mechanisms in the stellar corona have been proposed. Narain and Ulmschneider (1990) were able to list a very large number of possible heating mechanisms, from the classical acoustic wave heating to dissipative processes involving e.g. fast and slow MHD waves, Alfvén waves and magnetic reconnection.

Other mass loss theories involve magnetic fields, but not as in the standard picture of dissipative processes in the stellar corona. For instance, the recent work done by MacDonald and Mullan (2025) suggests that mass loss might be due to reconnection of magnetic loops which rise up from the stellar interior. According to this theory, a shear instability induced by rotation on the regions beneath the lower convective boundary of the stellar envelope might produce such magnetic loops, which can be pushed upwards after the removal of the steep gradient left by the deep penetration of convection (i.e., after the so-called RGB bump — when the hydrogen-burning shell reaches the sharp discontinuity in the hydrogen mass fraction profile). After reaching the surface, these magnetic loops could expand in the low-density atmosphere and eventually reconnect. This might pinch off the feet points of the loop, thus removing some plasma from the stellar surface. The mass loss rate predicted with this model is consistent within a factor of ~ 2 with the observed mean rate (after the RGB bump) of three different stellar populations (see references in MacDonald and Mullan 2025).

Returning back to the role of acoustic energy, I have so far discussed mechanisms focusing only on its dissipation. However, it has been suggested that oscillations themselves could possibly have sufficiently large amplitudes to produce accelerations comparable to the low surface gravity of giant stars. In this scenario, the pulsational acceleration itself might contribute significantly to mass ejection from the stellar surface. For example, the work done by Mosser et al. (2013) on evolved red giants showed that the pulsational acceleration is equal to the surface gravity for $\nu_{\max} \simeq 0.2\,\mu$Hz. This result could be the potential explanation of strong mass loss claimed by Glass et al. (2009) on AGB stars displaying oscillations with periods longer than 60 days, which corresponds to $\nu_{\max} \simeq 0.2\,\mu$Hz.

As it stands out from this brief overview, a huge number of different processes have been proposed throughout the years as a possible explanation of mass loss. We are now aware that mass loss in RGB stars is surely a very complicated process which involves hydrodynamic and MHD waves, magnetic fields and possibly also dust grains (see section 1.2.3). The main idea that motivated this project is reviewing the role of acoustic energy in mass loss from RGB stars, in the light of the recent developments on modelling stellar atmospheres — thanks to the advent of *3D simulations*. Indeed, 3D models can now give us more accurate information on the physical processes occurring in the near-surface layers of stars (see section 4.1 for more details). The main reference to pursue the aim of this project has been the mass loss prescription developed by Fusi-Pecci and Renzini (1975) (FPR, hereafter), which links the mass loss rate along the RGB with the total acoustic power produced in the convective envelope. The physical arguments behind the FPR mass loss prescription and its implementation in 1D models will be discussed in the next chapter.

Chapter 3

FPR mass loss prescription

The work of Fusi-Pecci and Renzini (1975) consists in building a *parametric* prescription of the mass loss rate, rather than modelling a potential physical mechanism involving the acoustic energy as a mass loss source. It is only based on the idea that acoustic waves provide the energy input for the wind, but it does not specify which exact physical mechanism is operating. For this reason, the FPR mass loss rate can still be a valuable reference in stellar models where RGB mass loss is assumed to be powered by some mechanisms involving the acoustic energy.

In section 3.1, I will describe the physical foundations of the FPR mass loss. This will be followed in section 3.2 by the description of its implementation in the 1D stellar evolutionary code Module for Experiments in Stellar Astrophysics (MESA) (Paxton et al. 2011). These models will be referred to as "standard FPR models", to distinguish them from the 1D simulations constructed on the basis of 3D simulations. The section 3.3 will be focused on describing the limitations of the FPR approach, which will justify and lay the groundwork for the use of 3D simulations, entirely discussed in chapter 4.

3.1 Physical foundations

Suppose an idealized scenario where, at any given time, the total acoustic power produced by convective motions within the stellar envelope is entirely used to remove matter from the surface, at the escape velocity. Therefore, the conservation of mechanical energy reads:

$$\frac{1}{2}\dot{\mu}_{\rm wind}v_{\rm esc}^2 - \frac{GM\dot{\mu}_{\rm wind}}{R} = 0 \quad \text{so that} \quad L_{\rm ac} - \frac{GM\dot{\mu}_{\rm wind}}{R} = 0 \tag{3.1}$$

where $\frac{1}{2}\dot{\mu}_{\rm wind}v_{\rm esc}^2$ is the rate of kinetic energy gained by the wind; M and R are the mass and the radius of the star; $L_{\rm ac}$ is the total acoustic power produced by convective motions. The rate of mass lost by the star is given by $\dot{\mu} \equiv -\dot{\mu}_{\rm wind}$. Therefore, equation (3.1) can be written as:

$$\dot{\mu} = -\frac{R}{GM}L_{\rm ac} \tag{3.2}$$

The mass loss rate given by equation (3.2) must be intended as an upper limit to the real mass loss rate, which is defined as:

$$\dot{M} = \eta_{\rm FPR}\dot{\mu} \tag{3.3}$$

where $\eta_{\rm FPR}$ is an efficiency factor. All the complex processes that actually drive mass loss are encapsulated in this factor, which is not known a priori. As for the Reimers' mass loss, the FPR efficiency factor is treated as a *constant free parameter*, to be adjusted on the basis of mass-loss estimates from observations.

As can be seen in equation (3.2), the whole problem of computing mass loss rates along the RGB reduces to the computation of $L_{\rm ac}$, the rate of acoustic energy radiated by the entire convective envelope. To compute this physical quantity, Fusi-Pecci & Renzini considered the Lighthill's theory for generation of sound (Lighthill 1952) due to fluctuating fluid motions. This theory, combined with the assumption of isotropic turbulence (Proudman 1952), is used to derive the expression for the rate of acoustic energy generated by turbulent convection, per unit volume:

$$P_{\rm ac} = 40\frac{\rho}{\lambda}\frac{v_{\rm conv}^8}{c_{\rm s}^5} = 40\frac{\rho v_{\rm conv}^3}{\lambda}\mathcal{M}_{\rm t}^5 \tag{3.4}$$

where ρ is the gas density; λ is a characteristic lengthscale of turbulence; $v_{\rm conv}$ is the characteristic velocity of convective motions; $c_{\rm s}$ is the sound speed; $\mathcal{M}_{\rm t}$ is the turbulent Mach number, defined as $\mathcal{M}_{\rm t} \equiv v_{\rm conv}/c_{\rm s}$. Then, the total acoustic power $L_{\rm ac}$ emitted by the star can be computed as the volume integral of $P_{\rm ac}$ throughout the whole convective envelope. From Fusi-Pecci and Renzini (1975):

$$L_{\rm ac} = \frac{1}{2}\int_V P_{\rm ac}{\rm d}V \tag{3.5}$$

Given its importance for the FPR mass loss prescription, in the next section I briefly summarize the most important aspects of Lighthill's theory and the various steps needed to recover the expression for the acoustic power per unit volume, reported in equation (3.4). This is important not only to understand what is the physical explanation of this expression, but also to clarify the various assumptions underlying it. What follows is based on section 4.1 of the review by Samadi (2000) on Lighthill's theory.

3.1.1 Lighthill's theory

Lighthill (1952) developed a theory to determine the generation of acoustic waves induced by motion of matter within a homogeneous fluid. In stars, this assumption is equivalent to *neglecting the radial stratification* of the gas. Therefore, the self-gravitational force acting on the gas is zero. In this framework, the motion of gas is governed by:

$$\rightarrow \text{mass conservation:} \quad \frac{\partial\rho}{\partial t} + \frac{\partial(\rho u_i)}{\partial x_i} = 0 \tag{3.6}$$

$$\rightarrow \text{equation of motion:} \quad \frac{\partial(\rho u_i)}{\partial t} + \frac{\partial(\rho u_j u_i)}{\partial x_j} = -\frac{\partial p}{\partial x_j} + \frac{\partial \tau_{ij}}{\partial x_j} \tag{3.7}$$

where the index i is summed over and $j = 1, 2, 3$. The term τ_{ij} is the ij-component of the viscous stress tensor. By applying the time derivative to equation (3.6), the spatial derivative $\frac{\partial}{\partial x_j}$ to (3.7) and combining the two, we obtain:

$$\frac{\partial^2\rho}{\partial t^2} - \frac{\partial^2(\rho u_i u_j)}{\partial x_i \partial x_j} = \frac{\partial^2}{\partial x_i \partial x_j}(p\delta_{ij} - \tau_{ij}) \tag{3.8}$$

Then, we write the density ρ and pressure p as the sum between their equilibrium value and their fluctuation, i.e. $\rho = \rho_0 + \delta\rho$ and $p = p_0 + \delta p$. Moreover, we neglect the viscosity effects and set $\tau_{ij} = 0$[1]. . After these substitutions and some manipulation:

$$\frac{\partial^2 \delta\rho}{\partial t^2} - c_\mathrm{s}^2 \frac{\partial^2 \delta\rho}{\partial x_i \partial x_i} = \frac{\partial^2 T_{ij}}{\partial x_i \partial x_j} \tag{3.9}$$

where c_s is the sound speed, which is constant within a homogeneous perfect gas and T_{ij} is the so-called *Lighthill tensor*, defined as:

$$T_{ij} \equiv \rho u_i u_j + (\delta p - c_\mathrm{s}^2 \delta\rho)\delta_{ij} \tag{3.10}$$

If the fluid is static ($\boldsymbol{u} = 0$), equation (3.9) reduces to the propagation equation of sound waves in a homogeneous medium — i.e., $\frac{\partial^2 \delta\rho}{\partial t^2} - c_\mathrm{s}^2 \frac{\partial^2 \delta\rho}{\partial x_i \partial x_i} = 0$ — provided that entropy fluctuations are neglected, so that the density and the pressure perturbations are related as $\delta p = c_\mathrm{s}^2 \delta\rho$. However, if the fluid is not static, acoustic waves are instead governed by the propagation equation in the more general form reported in (3.9), where it stands out that fluid motions constitute a *source term* for acoustic waves. Explicit solutions of (3.9) exist only if the source term T_{ij} can be expressed independently of ρ. This can be accomplished under the following conditions:

- entropy fluctuations are neglected, so that $\delta p = c_\mathrm{s}^2 \delta\rho$;
- the velocity field is of *turbulent* origin, which is indeed the actual condition of convective motions within the envelopes of red giants. In this framework, it is possible to define the turbulent Mach number as $\mathcal{M}_\mathrm{t} \equiv v_\mathrm{turb}/c_\mathrm{s}$, where v_turb is a characteristic velocity of turbulence. It is possible to show, after some considerations not reported in this work, that the density fluctuations due to turbulent motions scale as $\sim \rho_0 \mathcal{M}_\mathrm{t}^2$. Therefore, if we assume that $\mathcal{M}_\mathrm{t}$ is low (which is a good assumption in the bulk of the convection zone of giant stars), it is reasonable to approximate $\rho u_i u_j \simeq \rho_0 u_i u_j$ in the definition of the Lighthill tensor (3.10).

In the light of these assumptions, the propagation equation (3.9) can be reduced to:

$$\frac{\partial^2 \delta\rho}{\partial t^2} - c_\mathrm{s}^2 \frac{\partial^2 \delta\rho}{\partial x_i \partial x_i} = \frac{\partial^2 T_{ij}}{\partial x_i \partial x_j} \simeq \frac{\partial^2}{\partial x_i \partial x_j}(\rho_0 u_i u_j) \tag{3.11}$$

A general solution to this partial differential equation (PDE) can be obtained by using the Green's function method. The form of this general solution is complicated and particularly difficult to solve numerically. However, it can be greatly simplified if the *far field* approximation is considered. In this context, "far field" means that we study acoustic waves only on regions far from the turbulent motions originating them. In this simplified case, the solution reads:

$$\delta\rho(\boldsymbol{x}, t) = \frac{1}{4\pi c_\mathrm{s}^4 |\boldsymbol{x}|} \frac{x_i x_j}{x^2} \int_V \frac{\partial^2}{\partial t^2} T_{ij}\left(\boldsymbol{y}, t - \frac{|\boldsymbol{x} - \boldsymbol{y}|}{c_s}\right) \mathrm{d}^3 y \tag{3.12}$$

[1]This approximation is valid in the stellar context, since the molecular viscosity is indeed very low. For instance, the typical Reynolds number close to the near-surface convection zone of the Sun is $\mathrm{Re} \sim 10^{12}$ (Philidet 2021). In general, Re is much larger than unity in stars, so the viscous effects are negligible.

Let λ be the characteristic lengthscale of turbulent eddies and $v_{\rm turb}$ their characteristic velocity. An approximate form of equation (3.12) can be obtained by doing the following order-of-magnitude estimates:

$$T_{ij} \sim \rho_0 v_{\rm turb}^2 \;\; ; \;\; \frac{\partial}{\partial t} \sim \frac{v_{\rm turb}}{\lambda} \;\; ; \;\; \int_V {\rm d}^3 y \sim \lambda^3 \tag{3.13}$$

which substituted in (3.12) lead to:

$$\delta\rho(\boldsymbol{x},t) \approx \rho_0 \frac{\lambda}{4\pi|\boldsymbol{x}|} \mathcal{M}_{\rm t}^4 \tag{3.14}$$

The rate of acoustic energy passing through a given point $\boldsymbol{x}$, per unit surface — the so-called *acoustic intensity*[2] — is given by:

$$\mathcal{J} = \frac{c_{\rm s}^3}{\rho_0} \langle (\delta\rho)^2 \rangle \tag{3.15}$$

where $\langle (\delta\rho)^2 \rangle$ is the average of the squared density fluctuation at the point $\boldsymbol{x}$. Then, the total rate of acoustic energy passing through a sphere of radius $|\boldsymbol{x}|$ is approximately:

$$W_{\rm ac} \equiv 4\pi |\boldsymbol{x}|^2 \cdot \mathcal{J} \tag{3.16}$$

Using the estimated $\delta\rho$ reported in equation (3.14), we can determine an approximated relation which links the total acoustic power with the characteristic physical quantities of the fluid:

$$W_{\rm ac} \approx \rho_0 v_{\rm turb}^3 \lambda^2 \mathcal{M}_{\rm t}^5 \tag{3.17}$$

The approximated rate of acoustic power generated *locally* per unit volume can then be obtained:

$$P_{\rm ac} \sim \frac{W_{\rm ac}}{\lambda^3} = \rho_0 \frac{v_{\rm turb}^3}{\lambda} \mathcal{M}_{\rm t}^5 = \frac{\rho_0}{\lambda} \frac{v_{\rm turb}^8}{c_{\rm s}^5} \tag{3.18}$$

A detailed analysis by Proudman (1952) was aimed at finding a proper numerical coefficient to the relation (3.18), which in fact just shows an approximated functional dependence on the main physical quantities. To reach this objective, he assumed turbulence to be *isotropic*, which means that all the directional information is lost as the kinetic energy is transferred from the largest scales to the smallest ones. Proudman derived a coefficient of the order of 40. We can finally recognize that equation (3.18) has the same form as the relation reported in (3.4), provided that the convective velocity is similar to the characteristic turbulent velocity.

The above overview on Lighthill's theory has shed more light on the physical origin of equation (3.4). Let me now return back to the work of Fusi-Pecci and Renzini (1975). They integrated the density of acoustic power $P_{\rm ac}$ throughout the volume of various envelope models, corresponding to different initial low-mass stars having different initial chemical compositions. For these models, they were able to find the upper limit $\dot{\mu}$. Then, by means of known theoretical evolutionary tracks on the HR

[2] In its general definition, the acoustic intensity is a vector field defined as $\boldsymbol{I} = (\delta p)\boldsymbol{u}$ (see Lighthill 1978 for a complete discussion). A justification of equation (3.15) can be obtained from this definition, by computing $\langle |\boldsymbol{I}| \rangle = \langle (\delta p) |\boldsymbol{u}| \rangle$.

diagram, they derived a scaling relation that links the idealized $\dot{\mu}$ with the main global stellar parameters:

$$\dot{\mu} = (-10^{-10.38}\mathrm{M}_\odot\,\mathrm{yr}^{-1})\left(\frac{\alpha}{1.5}\right)^{3.52}\left(\frac{Z}{10^{-3}}\right)^{-0.04}\left(\frac{M}{0.8\,\mathrm{M}_\odot}\right)^{-1.4}\left(\frac{L}{\mathrm{L}_\odot}\right)^{1.92} \tag{3.19}$$

where α is the mixing length parameter, defined as $\alpha = \frac{\lambda}{H_p}$ (with H_p being the pressure scale height); Z is the mass fraction of metals. Note the strong dependence on luminosity: this is the dominant factor which makes $|\dot{\mu}|$ peak right at the very upper part of the RGB, close to the helium flash. Besides working on the upper limit of giant mass loss rates, the authors also independently worked on a solar envelope model, to derive the corresponding upper limit to the mass loss rate:

$$\dot{\mu}_\odot = -10^{-10.60}\left(\frac{\alpha}{1.5}\right)^{2.77} \tag{3.20}$$

By combining this equation with the observed mass loss rate of the Sun, the FPR efficiency factor could be estimated:

$$\eta_{\mathrm{FPR},\odot} \equiv \frac{(\dot{M})_\odot}{\dot{\mu}_\odot} \approx (8 \pm 3) \times 10^{-4}\left(\frac{\alpha}{1.5}\right)^{-2.77} \tag{3.21}$$

While for the Sun it was possible to derive an estimate of the efficiency factor, the same could not be done for RGB stars, because the theories on stellar coronas were not developed enough to allow firm conclusions about the value of η_{FPR} for red giants (Fusi-Pecci and Renzini 1975). Therefore, FPR adjusted η_{FPR} a posteriori, on the basis of the RGB mass-loss estimates constrained in Rood's studies on the HB morphology of globular cluster ($\Delta M \simeq 0.2\,\mathrm{M}_\odot$, see section 1.1.2). Efficiencies $\eta_{\mathrm{FPR}} \approx \eta_{\mathrm{FPR},\odot}$ could match the observed HB morphology. For instance, by fixing $\eta_{\mathrm{FPR}} = 6 \times 10^{-4}$, they could reproduce the observed HB position of the globular cluster M3.

In a following study, Fusi-Pecci and Renzini (1976) discussed another interesting result concerning their mass loss prescription. They proved that both FPR and Reimers' mass loss can fulfill the observed requirement of an integrated RGB mass loss of $\Delta M \simeq 0.2\,\mathrm{M}_\odot$, provided that the efficiency factors are chosen so that $\eta_{\mathrm{FPR}} \approx \eta_{\mathrm{FPR},\odot}$ for the former and $\eta_{\mathrm{R}} \simeq 0.4$ for the latter. Such η_{R} was well within the uncertainty range known at that time, $\eta_{\mathrm{R}} = [1/3 - 3]$. This result supported the idea that the energy associated to acoustic waves could really be the source of mass loss in RGB stars.

3.2 Implementing the standard FPR mass loss

Computation of the acoustic power L_{ac}. To implement the FPR mass loss in MESA, I built a custom subroutine that computes the volume integral throughout the whole convective envelope of the acoustic power per unit volume (equation 3.4). This subroutine was implemented in the FORTRAN script `run_star_extras.f90` and is called by MESA at each timestep, so that the rate of mass loss is updated at each timestep of the evolution of the star.

The physical quantities appearing in equation (3.4) are autonomously computed by the MESA code and can be used in `run_star_extras.f90`. Therefore, it was relatively

straightforward to compute the radial profile of $P_{\rm ac}$. The MLT mixing length λ and the convective velocity $v_{\rm conv}$ are defined at cell faces, instead the sound speed $c_{\rm s}$ is given at cell centers. Therefore, I estimated the values of λ and $v_{\rm conv}$ at cell centers by considering the mid point between two consecutive cell-face values of such arrays. This was needed to properly combine these quantities with $c_{\rm s}$ for computing the profile of the acoustic power density $P_{\rm ac}$.

To compute the volume integral of $P_{\rm ac}$, the subroutine needs to find the boundaries of the convective envelope, which are determined according to the Schwarzschild criterion. In particular, it selects the mass coordinates of the boundaries of the outermost convective zone — i.e., the cumulative mass of the star at the bottom and at the top of the convective envelope. This was done by using the arrays `s% cz_bot_mass` (`s% cz_top_mass`), which are autonomously constructed by MESA and contain the bottom (top) mass coordinates of all the convective zones. By selecting the outermost values of `s% cz_bot_mass` and `s% cz_top_mass`, the subroutine determines the mass coordinates at the bottom and at the top of the outer convective envelope.

To compute the volume integral (3.5), $P_{\rm ac}$ was converted into an energy density per unit mass by computing $P_{\rm ac}/\rho$. Physically, for each pair of consecutive cells `k` and `k+1`, this quantity is the acoustic power generated within the volume contained between the spherical shells `k` and `k+1`, divided by the mass enclosed within this volume.

Finally, the calculation performed at each timestep is:

$$L_{\rm ac} = \frac{1}{2}\int_V P_{\rm ac}{\rm d}V = \frac{1}{2}\int_{m_{\rm cz,bot}}^{m_{\rm cz,top}} \frac{P_{\rm ac}}{\rho}{\rm d}m \simeq \frac{1}{2}\sum_{\texttt{k}_{\rm bot}}^{\texttt{k}_{\rm top}-1} \frac{P_{\rm ac}(\texttt{k+1/2})}{\rho(\texttt{k+1/2})}[m(\texttt{k+1}) - m(\texttt{k})] \quad (3.22)$$

where $m_{\rm cz,bot}$ and $m_{\rm cz,top}$ are the mass coordinates at the envelope boundaries; `k+1/2` is the cell center between the outer cell faces `k` and `k+1`; $m(\texttt{k})$ is the mass enclosed within the outer cell face `k`. Finally, at each timestep, the total acoustic power $L_{\rm ac}$ is then used in combination with the radius R and the total mass M as given by equation (3.2) to compute the upper limit to the rate of mass loss $\dot{\mu}$.

Efficiency factor $\eta_{\rm FPR}$. The last step to compute the actual mass loss rate is fixing an efficiency parameter $\eta_{\rm FPR}$ and scale the upper limit $\dot{\mu}$ by that factor. On the same line as the FPR approach, I adopted a single and constant efficiency parameter $\eta_{\rm FPR}$. I considered the solar $\eta_{\rm FPR,\odot}$ reported in equation (3.21) and evaluated it assuming a mixing length parameter of $\alpha = 2$ (the default value used by MESA):

$$\eta_{\rm FPR} = \eta_{\rm FPR,\odot}\big|_{\alpha=2} = 8\times10^{-4}\left(\frac{2}{1.5}\right)^{-2.77} = 3.6\times10^{-4} \quad (3.23)$$

This value has been adopted for all the models, regardless of their initial mass and initial chemical composition (see section 5.4 for further discussions on the efficiency parameter). In all the models, I let the star start to lose mass at the end of the MS stage.

Construction of the grid. The grid of standard FPR models covers the following parameters:

- initial mass $M_{\rm in} = 0.8\,{\rm M}_\odot$, $0.9\,{\rm M}_\odot$, $1.0\,{\rm M}_\odot$;

- initial [Fe/H] = −2.00, −1.50, −1.00, −0.50, 0.00, +0.20;
- initial helium mass fraction $Y = 0.24$, 0.26, 0.28, 0.30.

totalling to 72 models. The quantity [Fe/H] was used to compute the initial mass fraction of metals Z. The Asplund metal abundances and relative opacity tables were adopted for all the models (Asplund et al. 2009). The derivation of Z from [Fe/H] was done in two different ways, depending on the value of [Fe/H].

[Fe/H] > −1.0 . For these models, the simplest definition of Z was used, where the α-enhnacement is assumed to scale as in the Sun — $[\alpha/\mathrm{Fe}] = 0.0$. In this framework, [Fe/H] is related to Z through:

$$\log \frac{Z}{Z_\odot} = [\mathrm{Fe/H}] \tag{3.24}$$

where $Z_\odot = 0.015553$ is the initial metal mass fraction that reproduces the Asplund solar metallicity.

[Fe/H] ≤ −1.0 . For the most metal-poor stars — with [Fe/H] ≤ −1.0 — I considered the α-enhanced opacity tables and used the Salaris correction (Salaris, Chieffi, and Straniero 1993) to estimate the contribution to the metal mass fraction by α-elements:

$$[\mathrm{M/H}] = [\mathrm{Fe/H}] + \log\left(0.6387 \cdot 10^{[\alpha/\mathrm{Fe}]} + 0.3613\right) \tag{3.25}$$

where $[\alpha/\mathrm{Fe}]$ is the alpha-enhancement; the numerical coefficients are calculated on the basis of the Asplund metal mixture. The ratio $[\alpha/\mathrm{Fe}]$ is assumed to be +0.4 for all models with [Fe/H] ≤ −1.0. I made this choice to be consistent with the FPR3D models that I will introduce in the next chapter. This consistency was necessary to perform meaningful comparisons between the standard FPR and FPR3D models. From equation (3.25), it is possible to derive the initial metal abundance Z through:

$$[\mathrm{M/H}] = \log\left(\frac{Z/X}{Z_\odot/X_\odot}\right) \tag{3.26}$$

where X and $X_\odot$ are the initial mass fractions of hydrogen of the examined model and of the Sun, respectively. The Asplund solar calibration is used for the solar values: $X_\odot = 0.717008$ and $Z_\odot = 0.015553$.

For any given pair of [Fe/H] and $[\alpha/\mathrm{Fe}] = +0.4$, it is possible to derive [M/H], which in turn can be used to compute Z through equation (3.26). In fact, by requiring $X = 1 - Y - Z$ and combining (3.25) and (3.26), we obtain:

$$Z = \frac{C(1-Y)}{1+C} \tag{3.27}$$

with $C \equiv (Z_\odot/X_\odot)10^{[\mathrm{M/H}]}$. Therefore, at fixed [Fe/H] and $[\alpha/\mathrm{Fe}] = +0.4$, it is possible to derive Z for any given value of Y within the covered range $Y = 0.24 - 0.30$.

The mixing length parameter. The choice of the mixing length parameter α has a great impact on the standard FPR mass loss, because it determines the mixing-length of convection λ which is an important factor in the computation of the total acoustic power $L_{\rm ac}$. For this project, given the use of the Asplund metal mixture and relative opacity tables, I set the mixing length parameter to its Asplund solar value: $\alpha = \alpha_\odot = 1.967534$. For further discussions on the choice of the mixing length parameter, see section 5.4.

Overshooting. Concerning the evolutionary phases close to the RGB tip, overshooting was added to make a more realistic and smoother transition between the convective zone triggered by the helium flash and the upper, thin radiative zone below the hydrogen-burning shell. I used the diffusive exponential scheme for overshooting and set `overshoot_f = 0.025` and `overshoot_f0 = 0.005` (see the MESA documentation for an exhaustive explanation of these parameters).

Stopping conditions. All the models start from the pre-main sequence phase. The main condition to determine the point where MESA stops the evolution of the star was set to the zero-age core-He burning (ZACHeB) — i.e., the beginning of the stable He burning within a non-degenerate core. To save time and computing resources, models exceeding a stellar age of 16 Gyr were stopped. This is well above the estimated age of the Universe and models reaching an age higher than this threshold cannot be considered as physically informative. From now on, unless stated differently, diagrams and results refer to models which did not exceed this maximum age.

3.2.1 General properties of standard FPR models

In this section, I present the main and general results of the standard FPR models.

Almost all of the total RGB mass loss is concentrated over the rapid evolutionary phases *right before the helium flash*. This can be seen for instance in the panels of figure 3.1, where I report the evolutionary properties of one stellar model as a reference. The absolute value of the mass loss rate $|\dot{M}|$ reaches very high values — of the order of $10^{-8} - 10^{-7}\,\mathrm{M}_\odot\,\mathrm{yr}^{-1}$ — on the high-luminosity portion of the RGB. This behaviour was actually expected and consistent with the strong dependence of $\dot{M}$ with luminosity found by Fusi-Pecci and Renzini 1975 (see the scaling law 3.19).

Another interesting property found for all the standard FPR models is the location inside the star where most of the acoustic energy is produced. Studying this property is important for two reasons:

1. to identify over which regions acoustic waves are mostly produced and why;

2. to justify the approach of using 3D hydrodynamic simulations for improving the FPR mass loss prescription. In fact, as I will explain more extensively in section 4.1, these 3D hydrodynamic simulations consist in small boxes, placed around the superadiabatic region and probing only a small and superficial portion of the entire convective envelope. For this reason, if the regions where most of the acoustic energy is produced were not around the superadiabatic zone, but rather located deeper down in the envelope, any information extracted from 3D atmosphere simulations could not be used for the scopes of this project.

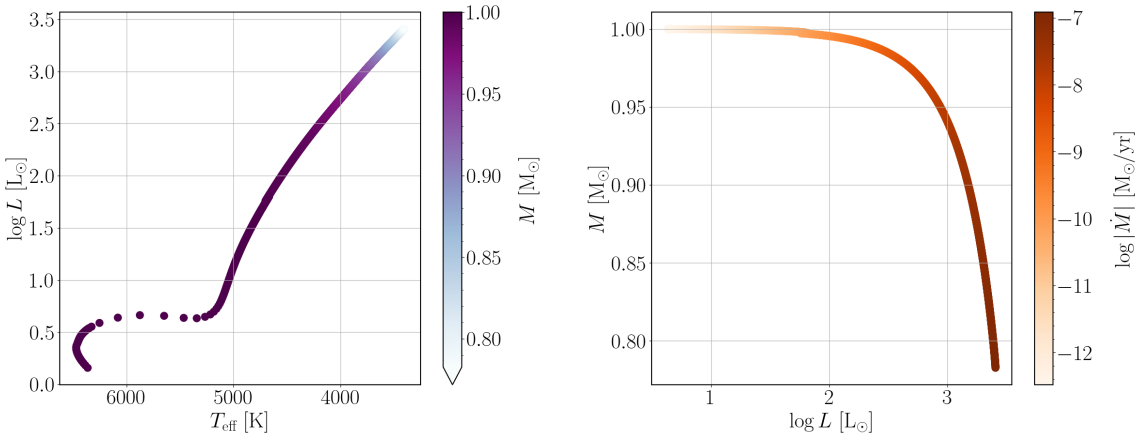

Figure 3.1: Evolutionary properties of the stellar model with initial mass $M_{\rm in} = 1.0\,\mathrm{M}_\odot$, $Y = 0.28$ and $[\mathrm{Fe/H}] = -0.50$. *Left panel*: evolutionary track on the HR diagram from MS to the RGB tip, colorized by stellar mass. *Right panel*: Mass of the star M versus $\log(L/L_\odot)$. The color bar represents the logarithm of the absolute value of the mass loss rate.

By looking at figure 3.2, we can see that the vast majority of the total acoustic power is produced in the superadiabatic region. This is due to the behaviour of the turbulent Mach number $\mathcal{M}_{\rm t}$, which exactly peaks on that region. The turbulent Mach number has a great impact in determining the amount of acoustic power generated locally, as it appears to a power of five in equation (3.4). The peak of $\mathcal{M}_{\rm t}$ occurs in this zone for two reasons:

- from the bottom to the top of the convective envelope, the density of the gas decreases and becomes low at the top of the convective zone. Therefore, to carry the same amount of convective flux (roughly), $v_{\rm conv}$ must increase as we approach the surface, reaching its maximum on the superadiabatic region;
- the gas temperature decreases as we move towards the top of the envelope. Thus, the sound speed is relatively low in correspondence of the superadiabatic region.

These two facts combined together make the turbulent Mach number $\mathcal{M}_{\rm t}$ peak where the convective efficiency drops.

Besides justifying the approach of using 3D simulations to search for a better treatment of acoustic power, the fact that most of this energy is produced over this thin and superficial zone of the envelope further motivates the effort of using 3D hydrodynamic simulations to search for a better treatment of this quantity. Indeed, this is the region where the FPR prescription is mostly affected by its limitations. An extensive discussion of the limitations of the FPR mass loss prescription and the reasons why they specifically regard the near-surface layers is given in section 3.3.

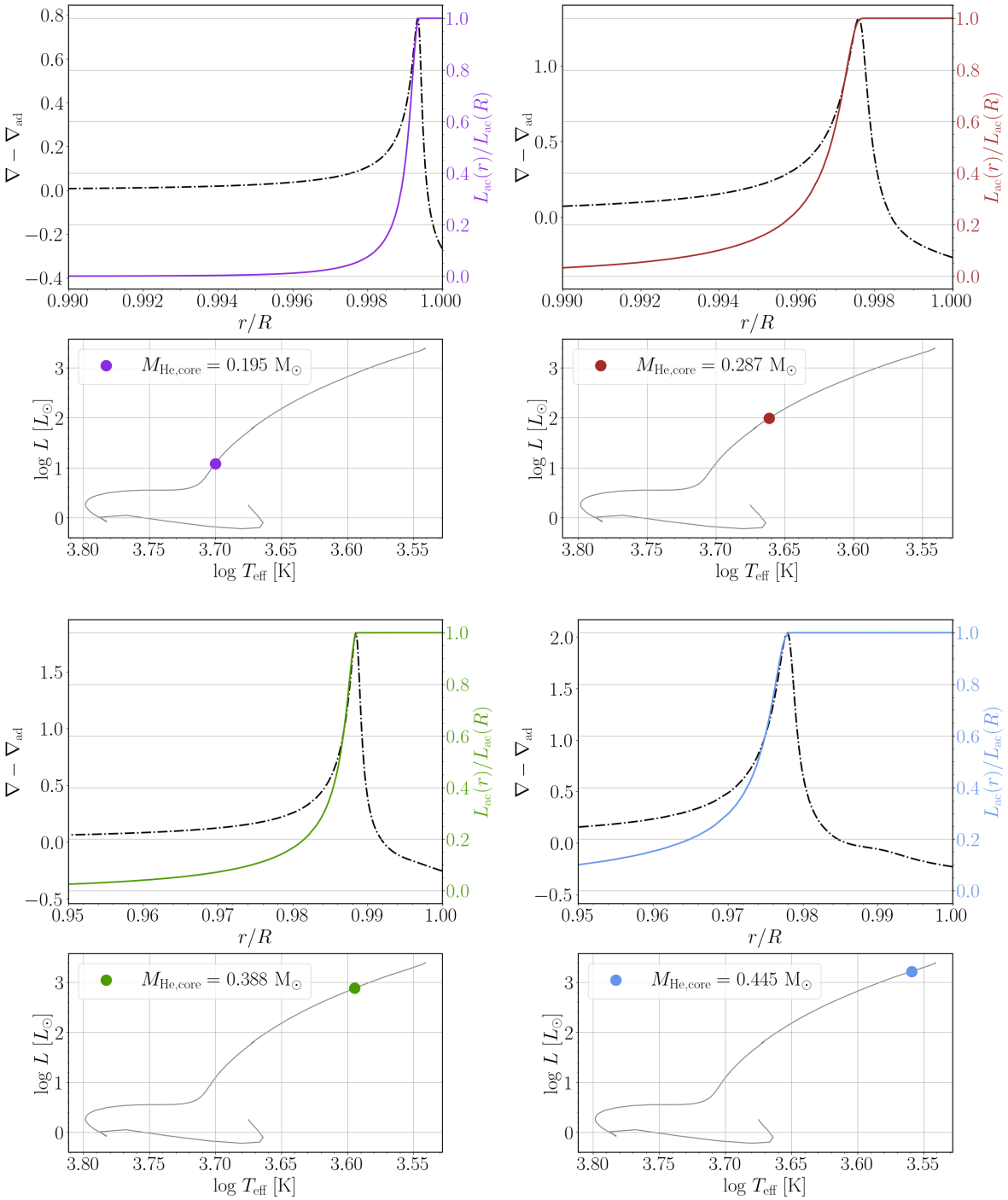

Figure 3.2: Each of the four panels relate to the same star at four different evolutionary stages. The initial mass is $M_{\rm in} = 0.9\,{\rm M}_\odot$, initial He abundance $Y = 0.26$ and [Fe/H] $= -1.00$.

For each panel: *Top subplot*: profile of the superadiabatic gradient $\nabla - \nabla_{\rm ad}$ (dot-dashed black line) and of the cumulative acoustic power normalized to the total $L_{\rm ac}$: $L_{\rm ac}(r)/L_{\rm ac}(R)$ (colorized solid line). The horizontal axis shows the distance from the center, normalized to the stellar radius R. *Bottom subplot*: evolutionary track on the HR diagram, from the pre-main sequence up to the RGB tip (grey solid line). The single point indicates the location on the RGB where the profiles $\nabla - \nabla_{\rm ad}$ and $L_{\rm ac}(r)/L_{\rm ac}(R)$ were extracted. The legend shows the mass of the He core at that evolutionary stage.

3.2.2 The total integrated mass loss ΔM along the RGB

In this last section, I present the results of the total integrated mass loss along the RGB for the standard FPR models.

Depending on their initial mass and chemical composition, stars terminate their RGB phase in two different ways:

- For the lowest-mass stars ($M_{\rm in} = 0.8\,{\rm M}_\odot$), the mass loss along the RGB is so high that almost all of these models terminate their ascent along the RGB before reaching the helium flash. This happens because they lose their entire envelope, ending their evolution as He white dwarfs (see figure 3.3a).

- Almost all of the $M_{\rm in} = 0.9\,{\rm M}_\odot$ and $M_{\rm in} = 1.0\,{\rm M}_\odot$ models reach instead the ZACHeB. Only one model (represented by the blue curve) with $M_{\rm in} = 0.8\,{\rm M}_\odot$, $Y = 0.30$ and [Fe/H] $= -2.00$ does so. This is also the only model not experiencing a regular He flash at the tip of the RGB, but rather a *late* flash (see figure 3.3b). It is the only model displaying an intermediate behaviour between stars losing their whole envelope and those which easily reach the ZACHeB through a regular flash.

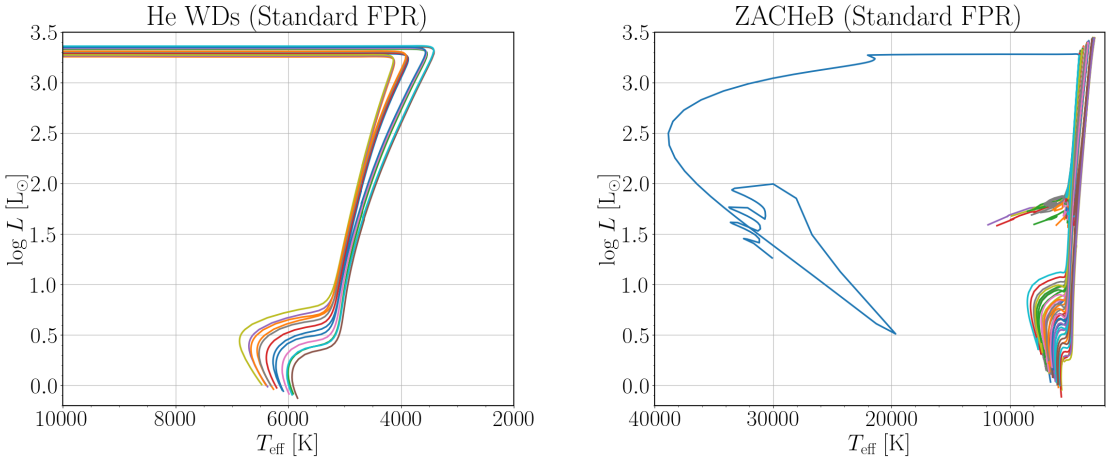

(a) (b)

Figure 3.3: Evolutionary tracks on the HR diagram (from main sequence) of the standard FPR models. *Left panel*: $M_{\rm in} = 0.8\,{\rm M}_\odot$ models losing the entire convective envelope before the helium flash, thus becoming He white dwarfs. *Right panel*: models reaching the ZACHeB. The blue curve reaching very high effective temperatures represents the model with $M_{\rm in} = 0.8\,{\rm M}_\odot$, $Y = 0.30$ and [Fe/H] $= -2.00$, experiencing a late helium flash.

The only models with [Fe/H] $= +0.20$ which did not exceed a stellar age of 16 Gyr are ($M_{\rm in} = 1.0\,{\rm M}_\odot$, $Y = 0.28$) and ($M_{\rm in} = 1.0\,{\rm M}_\odot$, $Y = 0.30$). These models also have some numerical problems when they reach the He flash, as the star starts to do abrupt oscillations, drawing a non-physical stripe. The period over which the star undergoes the He flash is negligible in terms of the contribution to the total RGB mass loss, since this evolutionary stage is very rapid (though having the highest mass loss rate). For

this reason, these models were anyway included in this analysis and truncated right at the beginning of the He flash[3].

The total integrated mass loss ΔM has been taken as the difference between the initial mass of the star and its mass at the highest-luminosity point reached along the RGB. This point is also the evolutionary stage where the effective temperature $T_{\rm eff}$ of the star is at its minimum. Whether the star experiences the He flash at the tip, or a late flash, or it leaves the RGB because the whole convective envelope has been lost, the point where $T_{\rm eff}$ equals its minimum flags the end of the RGB. Therefore, in any case, I computed the total integrated mass loss along the RGB as:

$$\Delta M = M_{\rm in} - M\big|_{T_{\rm eff}=T_{\rm eff,min}} \tag{3.28}$$

In figure 3.4, we can study how the integrated mass loss along the RGB changes with varying the initial [Fe/H] and Y. Except for the top-left panel, where almost all the stars have lost their entire envelope, it is possible to note a clear trend in ΔM against variations in both [Fe/H] and Y.

- at fixed Y, we observe an increase of ΔM with increasing [Fe/H] until a value of [Fe/H] $\simeq -0.5$. The trend inverts for stars with [Fe/H] $\gtrsim -0.5$.
- at fixed [Fe/H], the total mass loss ΔM decreases if we increase the initial He mass fraction. In particular, the magnitude of this decrease appears to be constant when Y is increased by $\Delta Y = +0.02$ at each step (especially for $M_{\rm in} = 1.0\,{\rm M}_\odot$ models). In other words, the total mass loss ΔM decreases *linearly* with initial He mass fraction.

I will give further and more detailed discussions on these results in sections 5.1 and 5.3.

[3]The oscillations might originate from a bad treatment of mixing around the shell separating the convective envelope and the deeper radiative region. Perhaps, the convective envelope ingests some He and the resulting rapid change in the chemical composition causes the spurious and abrupt oscillations of luminosity and effective temperature. Adding undershooting at the bottom of the convective envelope might alleviate these numerical oscillations. In fact, undershooting is used in stellar models to account for the extra length traveled by downward-directed convective cells of gas, which cross the bottom boundaries of convective zones. Accounting for this effect would ensure a more realistic and less steep transition between the upper convective envelope and the deeper radiative zone. However, I would like to stress the fact that the predicted total RGB mass loss would not change relevantly, since the He flash is a very rapid evolutionary phase. This is the reason why these models were anyway included in the present analysis.

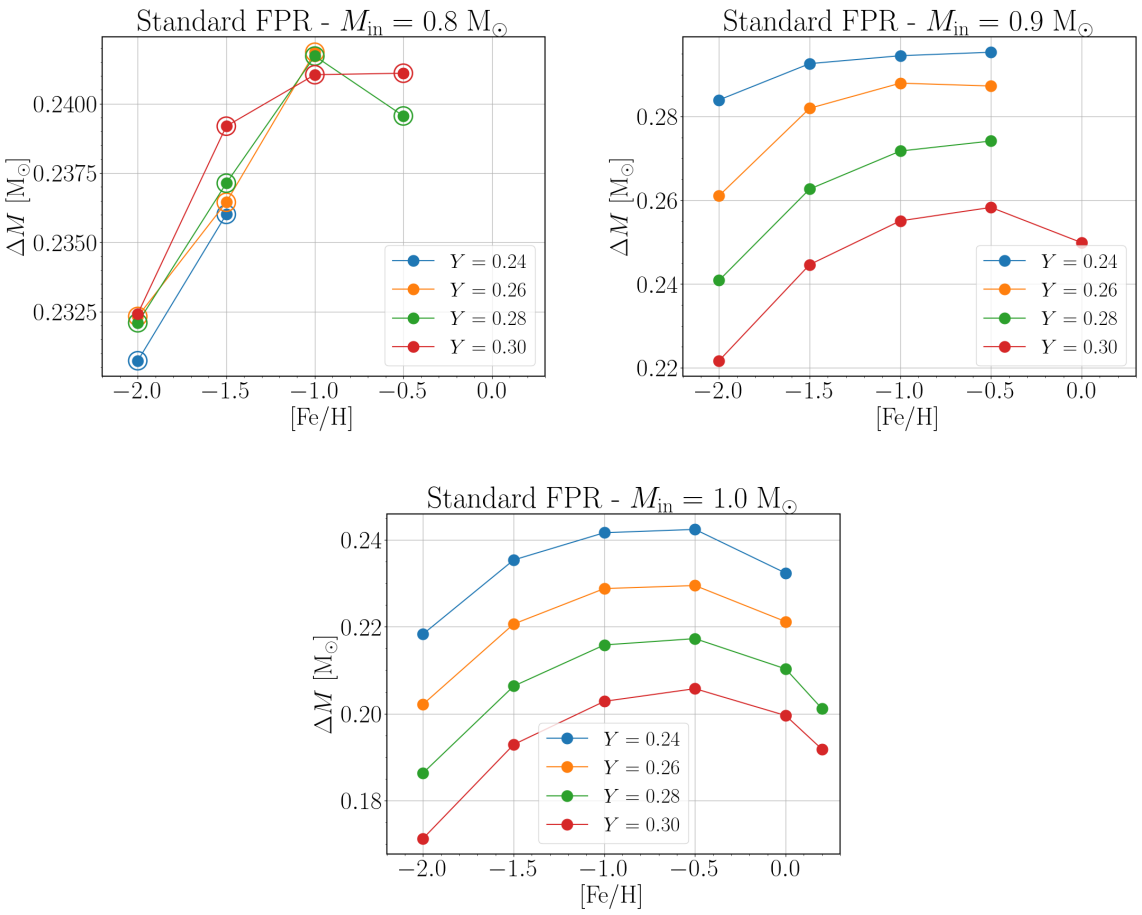

Figure 3.4: Total integrated mass loss ΔM along the RGB as a function of [Fe/H], for different initial He abundances. The encircled points represent models which lost their envelope before reaching the tip of the RGB, ending their evolution as helium white dwarfs. The other points represent models which have reached the ZACHeB, either through a regular He flash at the RGB tip or through a late He flash. The missing models are those having exceeded the maximum age of 16 Gyr. *Top-left panel*: Models with initial mass $M_{\rm in} = 0.8\,{\rm M}_\odot$. *Top-right panel*: Models with initial mass $M_{\rm in} = 0.9\,{\rm M}_\odot$. *Bottom panel*: Models with initial mass $M_{\rm in} = 1.0\,{\rm M}_\odot$.

3.3 Limitations of the FPR mass loss

Although the FPR approach has a more physical foundation than Reimers', it is affected by various limitations imported by the Lighthill's theory and by the use of MLT. In this paragraph, I describe why some assumptions are not representative of the real conditions in convective envelopes of giant stars. To describe the limitations of MLT, I follow section 1.2.2 of Philidet (2021).

Far-field approximation. The far-field approximation used to recover (3.12) is not physically consistent, because the generation of acoustic waves occurs locally, close to turbulent convective motions.

Isotropic turbulence. The assumption of isotropic turbulence that was needed to recover equation (3.4) is not an accurate description of how turbulent motions actually behave in the convective envelope of stars. This can be clearly noted in 3D hydrodynamic simulations, which show a very complex dynamics of convective cells. For instance, Kitiashvili et al. (2016) performed a 3D simulation of the entire convective envelope of a $1.47\,\mathrm{M}_\odot$ star and their velocity maps do not show the presence of regular turbulent eddies. In figure 3.5, we can in fact note the presence of fast downflows which extend in the deeper interior as elongated plumes. Upflows are instead slower and spread over more extended regions. We can also note the presence of faster and narrow upflows surrounding the downward-traveling plumes (i.e., the bright filaments surrounding dark areas in the velocity maps of figure 3.5).

No stratification. The assumption of homogeneous fluid in Lighthill's theory is not suitable for the stellar interiors, as stars are radially stratified. This approximation mostly fails in near-surface layers, specifically around the *super-adiabatic* region — where the convective efficiency in the energy transport drops (see next paragraph for details). This can be seen in figure 3.6, where the pressure scale height H_p drops right at the location where the superadiabatic gradient $\nabla - \nabla_{\mathrm{ad}}$ peaks[4].

The use of MLT. In the standard MLT, convection is assumed to consist of vertical columns of gas, some of which move upwards and other downwards. Each column is considered as a set of individual small volumes of gas, referred to as gas bubbles. Each gas bubble has its own velocity and temperature and, at a given depth, there will be gas bubbles moving upwards and downwards. At a given depth, all the bubbles have the same velocity.

We consider a bubble rising from a depth $z - s$ up to z. Throughout this motion, the pressure of the bubble remains in equilibrium with the surrounding pressure p_0. However, the temperature of the bubble changes, and consequently its density varies as well. In most of the convection zone, the energy exchange between the bubble and the surrounding medium is negligible, since the bubble undergoes an adiabatic expansion while rising upwards (see below for details). At depth z, the difference between the bubble temperature and the background temperature is given by:

$$\Delta T(s) = \frac{T_0}{H_p}(\nabla - \nabla_{\mathrm{bubble}})s \tag{3.29}$$

where T_0 is the background temperature; H_p is the pressure scale height of the background gas; ∇ and ∇_{bubble} are the temperature gradients of the background and the bubble, respectively:

$$\nabla \equiv \left(\frac{\mathrm{d}\ln T_0}{\mathrm{d}\ln p_0}\right) \quad ; \quad \nabla_{\mathrm{bubble}} \equiv \left(\frac{\mathrm{d}\ln T}{\mathrm{d}\ln p}\right)_{\mathrm{bubble}} \tag{3.30}$$

To onset a convective instability, $\nabla > \nabla_{\mathrm{bubble}}$ must hold, otherwise the bubble temperature at depth z would be lower than T_0. On the basis of the perfect gas law, this would imply a higher density than the background ρ_0, (since $p_{\mathrm{bubble}} = p_0$), which would

[4]The pressure scale height H_p is defined as the upward radial distance over which the gas pressure decreases by a factor of e: $H_p \equiv -(\frac{\mathrm{d}\ln p}{\mathrm{d}z})^{-1}$. Therefore, a decrease of H_p indicates a stronger stratification.

cause the bubble to fall back to the original depth $z - s$. Since we are interested in studying convective motions, we consider the case where $\nabla > \nabla_{\rm bubble}$. From equation (3.29), using the Newton's second law — where the force pushing the bubble is the buoyancy force — and the perfect gas law, it is possible to compute the velocity of the gas at depth z, after traveling the distance s:

$$v(s) = \left[\frac{g(\nabla - \nabla_{\rm bubble})}{H_p}\right]^{1/2} s \tag{3.31}$$

where g is the gravitational acceleration. Equations (3.29) and (3.31) can be used to evaluate the convective flux, which is given by $F_{\rm c} = \rho_0 c_p v \Delta T$ (for a detailed justification of this expression, see Philidet 2021). However, before doing the proper substitutions, we have to average over all the bubbles, since (3.29) and (3.31) only refer to one gas bubble with a travel distance s. Let λ be the average distance over which gas bubbles travel before being assimilated to their new environment. Now, at any given layer z, we assume that bubbles generate at depth $z - \lambda/2$ and dissolve at depth $z + \lambda/2$ (or vice versa). Therefore, we consider $s = \lambda/2$ as an average distance traveled in equations (3.29) and (3.31). We can now substitute $\Delta T(\lambda/2)$ and $v(\lambda/2)$ in the expression of $F_{\rm c}$ and obtain:

$$F_{\rm c} = \frac{\rho_0 c_p T_0 \sqrt{g}}{H_p^{3/2}} (\nabla - \nabla_{\rm bubble})^{3/2} \left(\frac{\lambda}{2}\right)^2 \tag{3.32}$$

Provided that the background physical conditions of the gas are known, to compute the convective flux $F_{\rm c}$ we would need the temperature gradient of the bubble $\nabla_{\rm bubble}$ and the averaged length traveled λ. The latter is exactly the quantity which appears in the expression of the acoustic power per unit volume used by FPR (equation 3.4). When using MLT (e.g., in 1D simulations of stellar evolution), the average length λ is a parameter fixed a priori and adjusted to values matching the horizontally-averaged physical quantities of 3D hydrodynamic simulations of convection. Usually, the parametric prescription is implemented in terms of the mixing-length parameter $\alpha = \lambda/H_p$. Besides the approach of calibrating α to reproduce the results of 3D simulations, it is also common to adopt the "solar" mixing length parameter — i.e., adjusted to reproduce the effective temperature and the radius of the Sun, in models with $1.0\,{\rm M}_\odot$ and solar metallicity. However, there is no physical argument supporting the universal use of the solar value for any kind of star.

Using the expression for $\Delta T(\lambda/2)$, it is possible to compute the ratio between the enthalpy transported by convection and the enthalpy lost through radiation. This quantity is the so-called *convective efficiency*:

$$\Gamma \equiv \frac{h_{\rm gain}}{h_{\rm loss}} = \frac{\nabla - \nabla_{\rm bubble}}{\nabla_{\rm bubble} - \nabla_{\rm ad}} \tag{3.33}$$

where $\nabla_{\rm ad}$ is the adiabatic temperature gradient. Note that $\nabla_{\rm bubble}$ must be higher than $\nabla_{\rm ad}$, otherwise the cooler background would heat up the bubble, violating the second law of thermodynamics. Böhm-Vitense (1958) derived the following estimate for the convective efficiency:

$$\Gamma = \frac{\rho_0^2 c_p T_0 \kappa_{\rm R} \lambda v}{24 \sigma T^4} \tag{3.34}$$

where $\kappa_{\rm R}$ is the mean Rosseland opacity. The convective envelope can be distinguished in two different regions, depending on how efficient is convection in carrying energy:

- in the bulk of the convection zone, the density ρ_0 and the opacity κ_{R} are high. Therefore, $\Gamma \gg 1$, so convection carries energy very efficiently. By looking at (3.33), we see that this condition can be satisfied only if $\nabla_{\mathrm{bubble}} \simeq \nabla_{\mathrm{ad}}$. Physically, this means that the bubble keeps most of its enthalpy while moving upwards — it almost rises adiabatically — and that amount will be transferred to the background only when the bubble dissolves. Since $\nabla_{\mathrm{bubble}} \simeq \nabla_{\mathrm{ad}}$, with the latter being a known quantity, the convective flux as given by equation (3.32) depends on λ only (assuming the equilibrium quantities ρ_0, T_0, g, H_p and ∇ to be known). The fact that $F_{\mathrm{c}} \simeq F_{\mathrm{c}}(\lambda)$ in the deeper portions of the convective envelope makes acceptable the application of MLT over those regions;

- in near-surface layers, the convective efficiency drops to values of the order of 1. In such regions, a non-negligible portion of the bubble enthalpy is lost to radiation and $\nabla_{\mathrm{bubble}} > \nabla_{\mathrm{ad}}$. This is indeed the relatively thin superadiabatic region. The gradient ∇_{bubble} is not a known quantity here, which makes determining the convective flux F_{c} much more complicated than in the bulk of the convection zone. This makes the MLT unsuitable to model convection in the outermost layers of convective envelopes.

In the light of these considerations, we can conclude that the standard MLT is already a rough modeling of convection, as it is based on a free parameter α which must always be adjusted ad-hoc. However, the approach is still acceptable in the deeper convection zone, whereas numerous complications arise when MLT is used to model near-surface convection. Besides the reasons explained above, see for example the multiple scales of gas motions and asymmetries between upflows and downflows of figure 3.5, which MLT is unable to predict. In addition, the convective velocity predicted by MLT abruptly drops to zero at the boundary layers separating convective zones from radiative regions, leading to non-physical hard boundaries without overshooting. Moreover, MLT also predicts incorrect pressure and density stratification in near-surface layers (Zhou et al. 2025). This originates the mismatch between predicted and observed oscillation frequencies of $p-$modes (the so-called surface effect, see J. Christensen-Dalsgaard et al. 1996).

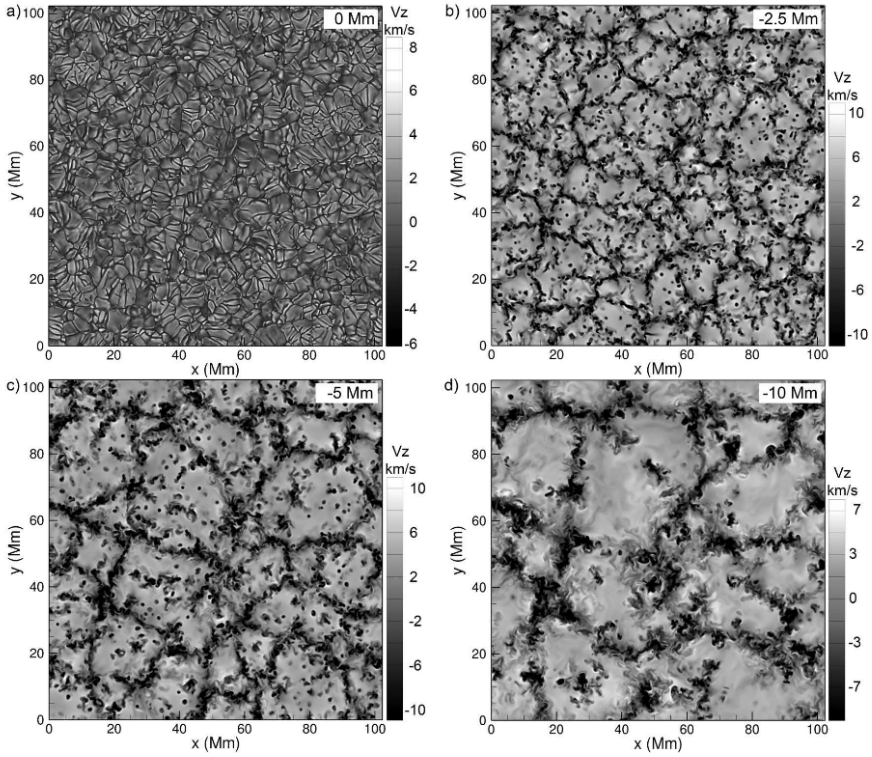

Figure 3.5: *Adapted from fig.1 in Kitiashvili et al. (2016)*: Horizontal sections of the map of the vertical velocity, at three different depths below the stellar surface (the top-left panel is a section of the surface).

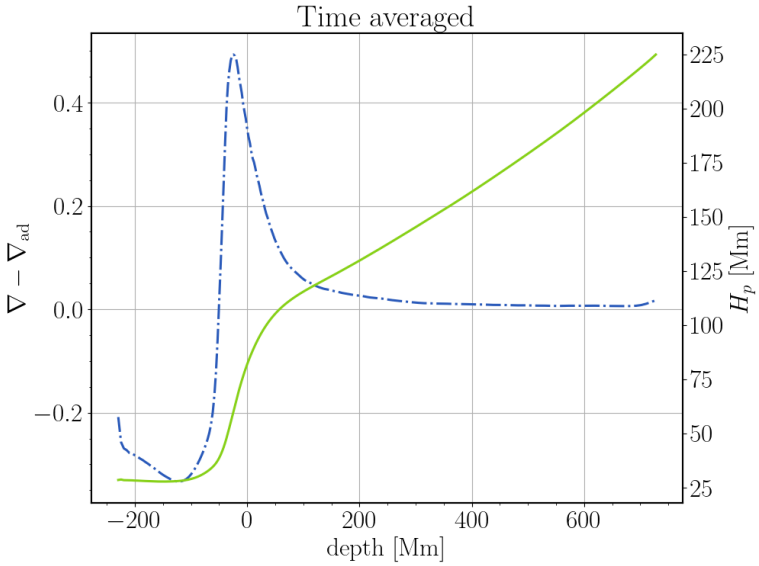

Figure 3.6: Horizontal averages at different depths of the superadiabatic gradient $\nabla - \nabla_{\rm ad}$ (blue dot-dashed line) and the pressure scale height H_p (green solid line). The surface of the star is on the left. All the quantities are time-averaged over all the snapshots. The examined quantities are taken from a 3D atmosphere model of a giant star of the STAGGER grid (Magic et al. 2013) with $\log g = 2.0$ (in cgs units), targeted effective temperature $T_{\rm eff,target} = 4500\,{\rm K}$ and [Fe/H] $= -0.5$.

Chapter 4

Acoustic Energy in 3D Simulations

4.1 Why use 3D simulations

- Scope of the project -

In view of the limitations affecting the computation of the acoustic power per unit volume $P_{\rm ac}$ in the FPR approach, the core of this project is to use 3D hydrodynamic simulations of stellar atmospheres to obtain a more realistic estimate of the acoustic energy. This will be used to derive a new formulation of the FPR prescription, as I explain in this section.

The simulations used for this project focus on a small box within the whole convective envelope, covering the layers around the superadiabatic region and the deeper zones below it. For this reason, these are named "*box-in-a-star*" simulations, which are obtained by solving the hydrodynamic equations from first principles, without relying on the MLT parametrization. Therefore, the dynamical structure of turbulent convective motions is much more accurate than that obtained by using 1D simulations. Moreover, the generation of acoustic waves naturally stands out from convection, as it happens in real stars. It is also possible to follow the temporal evolution of generation, propagation and damping of such waves.

I outline below the methods and steps performed to use box-in-a-star simulations with the purpose of improving the FPR formulation:

1. extracting the acoustic energy from all the 3D atmosphere models of the giant stars in the Stagger grid (Magic et al. 2013). Then, search for a relation linking the acoustic energy with stellar parameters (i.e., with effective temperature $T_{\rm eff}$, surface gravity g and [Fe/H]);

2. for the reasons explained in 4.3.1, I will calculate the acoustic energy per unit area, accumulated inside each simulated box. The main goal of the analysis is using such new relations in MESA: the structure of the FPR mass loss prescription will not change and the only quantity that will be modified is the total acoustic power $L_{\rm ac}$ in equation (3.2). From now on, I will indicate this mass loss prescription with the term *FPR3D*. The models where this prescription is implemented will be named as "FPR3D models";

3. chapter 5 will be focused on the interpretation and discussion of the obtained results, which will be compared with standard FPR models and a grid of MESA

simulations where the Reimers' mass loss was implemented. Additionally, a comparison will be performed with the most recent constraints obtained from observations.

4.2 The STAGGER grid

This grid was constructed by Magic et al. (2013) on the basis of the STAGGER-code, in pure radiation-hydrodynamics mode — i.e., ignoring magnetic fields. This code solves the time-dependent hydrodynamic equations for the conservation of mass, momentum and energy equation in a compressible flow. The interaction between matter and radiation is also considered, accounting for the radiative transfer equation. The curvature of the star is neglected, so that the code works on a Eulerian rectangular mesh. This mesh is *staggered* — i.e., the thermodynamic variables of internal energy per unit volume, density and temperature are cell-centered, whereas the three components of momentum are defined at cell faces. The approach of neglecting the sphericity of the star is justified by the fact that the volume covered by the 3D box is a very small fraction of the whole size of the star. For instance, the vertical size of the simulated box for the atmosphere of a star with $\log g = 1.5$ is $\sim 10\%$ of its typical stellar radius.

In figure 4.1 we can see the *targeted* models of the STAGGER grid. "Targeted" refers to the desired effective temperature a model is expected to reach. This is close, but not precisely the actual effective temperature models converge to. The covered range in effective temperature is $T_{\rm eff,target} = 4000 - 7000\,\mathrm{K}$, with a step of 500 K; the surface gravity spans from $\log g = 1.5$ to $\log g = 5$ (in cgs units), while the iron abundance [Fe/H] ranges from -4.0 to -1.0 with a step of 1.0, then from -0.5 to $+0.5$ with a step of 0.5. For models with [Fe/H] ≤ -1.0, an α-enhancement of $[\alpha/\mathrm{Fe}] = +0.4$ is used. Also, a simulation of the solar atmosphere is present, including the non-solar metallicity analogs. Given the framework of this project, I focused only on atmosphere models of giant stars ($\log g \leq 4.0$).

The dataset on which the present work was based contain the *geometrical*, horizontal averages of the physical quantities (`.havn` extension). This means that, for each red giant simulation of this dataset, I had access to a binary file (in the IDL save format — `.sav` extension) containing the averages of several physical quantities across different horizontal sections of the 3D cube — i.e., at different depths. Other output dataset from 3D hydrodynamic simulations contain instead horizontal averages taken at constant optical depth (either at fixed wavelength or considering the mean Rosseland opacity). I did not use these outputs in the present work and all the results are taken from geometrical horizontal averages.

In the considered dataset, 10 red giant atmosphere models are not available (see table 4.1). Moreover, not all the available simulations converged to a proper *thermal relaxation* — i.e., a quasi-stationary equilibrium state. Therefore, a further selection was needed to exclude them from the following analysis. A model which did not reach a correct convergence can be identified by looking at the behaviour of the effective temperature with the snapshots of the simulation. A model should be rejected if $T_{\rm eff}$ does not oscillate around a constant value, or if the fluctuations are too large. The general criterion I adopted to consider a given model as not properly converged is:

$$\sigma(T_{\rm eff}) \geq 25\,\mathrm{K} \qquad \text{or} \qquad |m| > 0.8 \tag{4.1}$$

where $\sigma(T_{\rm eff})$ is the standard deviation of the effective temperature values at different

snapshots, m is the slope of the linear best-fit of the curve $T_{\rm eff} = T_{\rm eff}(\texttt{snap})$. Four models were discarded on the basis of the above criterion (listed in table 4.1). Figure 4.2 shows two examples of the time evolution of $T_{\rm eff}$. This is the criterion adopted to select only models which reached a satisfactory convergence, but it should not be interpreted as a strict rule. In fact, to be conservative in my selection, I also discarded a few models which do not fall in the condition (4.1) but are either close to it, or have other kinds of irregularities. A complete description is given in table 4.1.

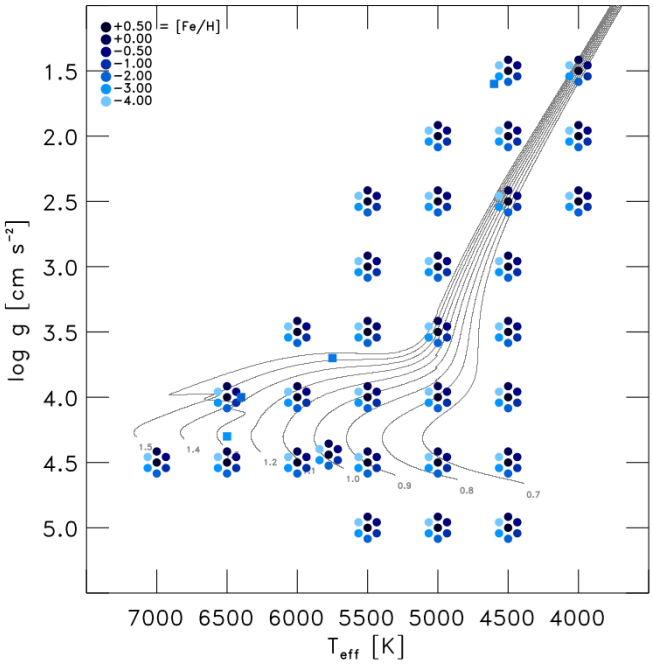

Figure 4.1: *Fig.1 of Magic et al. (2013)*: Kiel diagram of the STAGGER grid models for stellar atmospheres. The effective temperatures refer to their targeted values. Colors refer to different [Fe/H]. The squared points outside the regularly-spaced grid represent four additional stars. The grey solid lines are evolutionary tracks of stars with masses from 0.7 to 1.5 $M_\odot$, with solar metallicity.

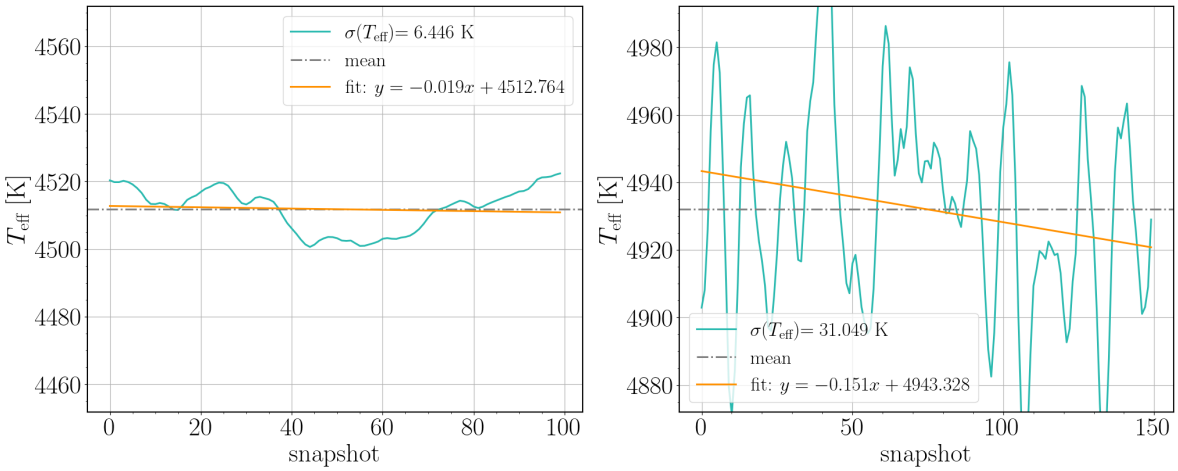

Figure 4.2: Behaviour of the effective temperature with snapshots. The orange solid line is the linear best fit, whose parameters are reported in the legend. The dot-dashed grey line is the mean effective temperature over the entire time span. The legend also contains the standard deviation of the effective temperature values. *Left panel*: converged model with [Fe/H] $= -2.0$, $\log g = 3.5$ and targeted effective temperature $T_{\rm eff,target} = 4500$ K. *Right panel*: not converged model (on the basis of the criterion 4.1) with [Fe/H] $= 0.0$, $\log g = 2.0$ and $T_{\rm eff,target} = 5000$ K.

$(T_{\mathrm{eff,target}}, \log g)$	[Fe/H]				
	−4.0	−1.0	−0.5	0.0	+0.5
(4000, 1.5)	issue				missing
(4000, 2.5)	issue				
(4500, 1.5)			missing	missing	missing
(4500, 2.0)					issue
(4500, 3.0)	issue				
(4500, 3.5)	issue				
(5000, 2.0)			not conv.	not conv.	missing
(5000, 2.5)					not conv.
(5500, 2.5)		missing	missing	missing	missing
(5500, 3.0)					missing
(6000, 3.5)				issue	issue
(6500, 4.0)					not conv.

Table 4.1: List of red giant models not included in this work. The targeted effective temperatures $T_{\mathrm{eff,target}}$ are in units of K, the logarithm of surface gravities $\log g$ are in cgs. "Missing" stands for models whose `.havn.sav` file is not present in the dataset; "not conv." stands for not converged; "issue" flags discarded models because of other irregularities: for [Fe/H] = −4.0: the model (4000, 1.5) was discarded because of NaNs spotted in the file; (4000, 2.5) shows a clear decreasing trend of T_{eff} with snapshots, even though the slope of the line is less steep than that of the selection criterion reported in equation (4.1); (4500, 3.0) and (4500, 3.5) have irregular horizontal averages of energy fluxes, not compatible with those reported in fig. 26 of Magic et al. (2013). [Fe/H] = 0.0: the model (6000, 3.5) was rejected because $\sigma(T_{\mathrm{eff}})$ is very close to the threshold of 25 K — $\sigma(T_{\mathrm{eff}}) = 23.7$ K — and particularly noisy time evolution of T_{eff}. [Fe/H] = +0.5: (4500, 2.0) and (6000, 3.5) were discarded because they have too few snapshots (3 and 26, respectively).

Accounting for the missing files and for the discarded models, the number of red giant atmosphere simulations used for this project totals to 126. All the following discussion and results refer to these studied 126 models. From now on, when I refer to the effective temperature $T_{\rm eff}$ of a given model, I mean the average calculated over the entire time span of that simulation. The targeted effective temperature will always be referred to as $T_{\rm eff,target}$.

4.3 The acoustic energy per unit area

The quantity I extracted from the `havn.sav` files is the horizontal average of the *vertical acoustic flux*, defined as:

$$\langle \boldsymbol{F_{ac}} \rangle \big|_z \equiv \big[\langle p_{\rm th} v_z \rangle - \langle p_{\rm th} \rangle \langle v_z \rangle \big] \hat{\boldsymbol{e}}_{\boldsymbol{z}} \tag{4.2}$$

where z is the considered depth, $p_{\rm th}$ is the thermal gas pressure, v_z is the vertical component of the vector field (upflows are assumed to have positive sign) and $\hat{\boldsymbol{e}}_{\boldsymbol{z}}$ is the vertical unit vector pointing towards the surface. Physically, this quantity is the average energy carried by acoustic waves through the horizontal section at depth z, per unit area. The angle brackets indicate the horizontal average done across the plane at depth z. The definition (4.2) is consistent with the standard definition of acoustic flux, which is:

$$\boldsymbol{F_{ac}} \equiv p'_{\rm th} \boldsymbol{v} \tag{4.3}$$

where $p'_{\rm th}$ is the pressure perturbation and $\boldsymbol{v}$ is the velocity vector field. At a given depth, if we assume the ensemble average of pressure to be equal to $\langle p_{\rm th} \rangle$, it is possible to recover the expression (4.2) by just considering the vertical component of $\boldsymbol{v}$ and set $p'_{\rm th} = p_{\rm th} - \langle p_{\rm th} \rangle$.

For each model, after having extracted $\langle \boldsymbol{F_{ac}} \rangle \big|_z$, I proceeded with a time average of this quantity over the whole time duration of the simulation. As a reference, I report in figure 4.3 an example of the typical trend of the vertical acoustic flux with depth. The behaviour of the curve is very similar in all the other models. The drop of the acoustic flux towards the surface is consistent with a fully radiative emergent flux, as described by Magic et al. (2013) (i.e., the total flux emerging from the surface is equal to the radiative flux $\sigma T_{\rm eff}^4$, where σ is the Stefan-Boltzmann constant). For the geometrical horizontal averages, the total energy flux is conserved throughout the vertical extension of the box. Therefore, $\sigma T_{\rm eff}^4$ represents the total energy flux even below the surface. The total energy flux is the sum between various energy fluxes (see Magic et al. 2013 for details), one of which is the acoustic flux. Below the photosphere, the ratio $\langle F_{\rm ac} \rangle \times (\sigma T_{\rm eff}^4)^{-1}$ suggests that the contribution of the acoustic flux to the total flux is small. This ratio is consistent with the typical value of ~ 0.04 reported by Magic et al. (2013). Another important result which stands out from each simulation is that the module of $\langle \boldsymbol{F_{ac}} \rangle \big|_z$ is higher at the bottom than at the top of the 3D box. This is indicative of an *accumulation* of acoustic power inside the simulated box. This amount of energy will be used to construct the FPR3D prescription, as explained in the next paragraphs.

4.3.1 Computation from the vertical acoustic flux

With the aim of computing the total acoustic power $L_{\rm ac}$ to be used in FPR3D models, it would be interesting to calculate this quantity for each red giant atmosphere

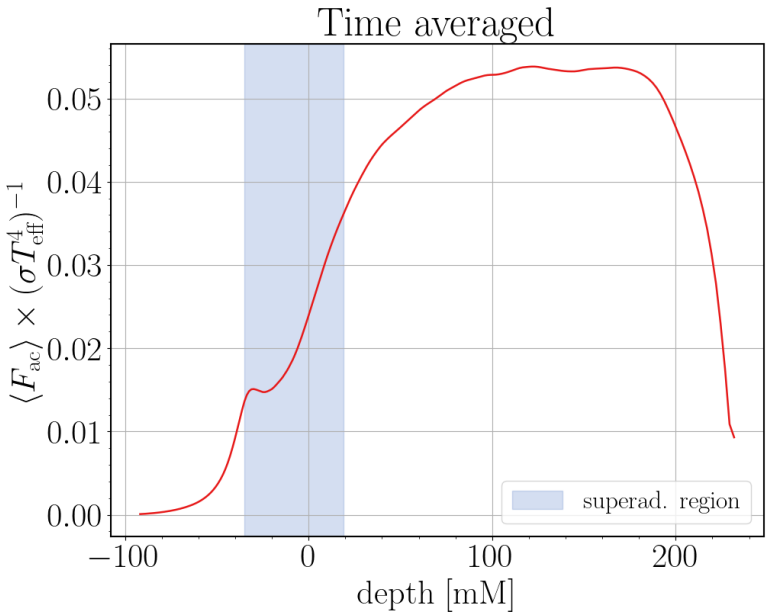

Figure 4.3: Module of the time- and horizontally-averaged vertical acoustic flux (normalized to the radiative flux $\sigma T_{\rm eff}^4$) as a function of depth. The surface of the star is on the left. The shaded area indicates the width of the superadiabatic region at 10% of the $\nabla - \nabla_{\rm ad}$ maximum. The examined model has [Fe/H] $= -0.5$, $\log g = 2.5$ and effective temperature $T_{\rm eff} = 5054\,\mathrm{K}$.

model. One can indeed use the vertical acoustic flux to compute the total acoustic power accumulated inside each single simulated 3D box. Then, one could assume this single, near-surface 3D cube to be representative of any analogous region, wherever its location, and therefore replicable over the whole stellar surface. Finally, by knowing the surface covered by the box and the radius of the star, the acoustic power accumulated inside that small region could be integrated over the whole stellar surface. If we neglect the contribution to the generation of sound waves by regions not probed by 3D hydrodynamic simulations (which is a very good approximation, see section 3.2.1), this quantity can be interpreted as the *global* acoustic power $L_{\rm ac}$ produced by convection across the whole star. However, this computation cannot be done just by using the information coming from 3D simulations: an atmosphere model of the Stagger grid is defined only by its metallicity, its effective temperature and its surface gravity. Any combination of only these three pieces of information is not sufficient to derive the stellar mass and the radius. The latter is necessary to calculate the global acoustic power $L_{\rm ac}$, which therefore remains impossible to compute just by using the information provided by a given model of the Stagger grid. Further independent constraints should be used to estimate the stellar radius associated to each red giant atmosphere simulation (for example, assigning a proper stellar luminosity or assuming the mass of the star a priori). In view of these considerations, I did not focus my analysis on the computation of $L_{\rm ac}$, but rather on the calculation of the total acoustic power produced *per unit area*. How this quantity was used for the construction of the FPR3D prescription is given in section 4.4. Below, I explain how this quantity was computed and the various assumptions underlying that.

For each simulated 3D cube, to compute the total acoustic power per unit area generated inside the simulated box, I considered the wave energy equation in its general

form derived by Unno et al. (1989):

$$\frac{\partial}{\partial t}(\rho e_W) + \nabla \cdot \boldsymbol{F_W} = \rho \delta T \frac{\partial \delta S}{\partial t} - \Phi' \frac{\partial \rho'}{\partial t} \tag{4.4}$$

where ρ is the density; e_W is the acoustic power per unit mass; $\boldsymbol{F_W}$ is the acoustic flux — here defined as $\boldsymbol{F_W} \equiv p'\boldsymbol{v} + \rho \boldsymbol{v} \Phi'$; δT and δS respectively are the temperature and entropy perturbations; Φ' is the perturbation of the gravitational potential and ρ' is the density perturbation. Assuming that acoustic waves do not exchange energy with the surrounding medium ($\frac{\partial \delta S}{\partial t} = 0$) and using the Cowling approximation ($\Phi' = 0$)[1], I could simplify (4.4) to:

$$\frac{\partial}{\partial t}(\rho e_W) = -\nabla \cdot \boldsymbol{F_W} \tag{4.5}$$

The total acoustic power is then obtained by integrating (4.5) over the volume of the box:

$$W_{\rm ac,box} \equiv \int_{V_{\rm box}} \frac{\partial}{\partial t}(\rho e_W) {\rm d}V = -\int_{V_{\rm box}} \nabla \cdot \boldsymbol{F_W} {\rm d}V = -\int_{\partial V_{\rm box}} \boldsymbol{F_W} \cdot {\rm d}\boldsymbol{S} \tag{4.6}$$

I denote the horizontal Cartesian coordinates with x and y and the vertical coordinate as z. Considering that boundary conditions along the $x-$ and $y-$ coordinates are periodic, equation (4.6) reduces to:

$$W_{\rm ac,box} = \int_{\partial V_{\rm box,bot}} [\boldsymbol{F_W}(x,y,z) \cdot \hat{\boldsymbol{e}}_{\boldsymbol{z}}] {\rm d}x{\rm d}y - \int_{\partial V_{\rm box,top}} [\boldsymbol{F_W}(x,y,z) \cdot \hat{\boldsymbol{e}}_{\boldsymbol{z}}] {\rm d}x{\rm d}y \tag{4.7}$$

where $\partial V_{\rm box,bot}$ and $\partial V_{\rm box,top}$ respectively are the bottom and top surfaces of the box. At each value of z, I assume the acoustic flux to be everywhere equal to the time- and horizontally-averaged vertical acoustic flux: $\boldsymbol{F_W}(x,y,z) \simeq \langle \boldsymbol{F}_{\rm ac} \rangle \big|_z$. Therefore:

$$W_{\rm ac,box} \simeq S_{\rm box} \big(\langle F_{\rm ac} \rangle \big|_{z_{\rm bot}} - \langle F_{\rm ac} \rangle \big|_{z_{\rm top}} \big) \tag{4.8}$$

where $S_{\rm box}$ is the area of the 3D cube's base; $\langle F_{\rm ac} \rangle \big|_{z_{\rm bot}}$ and $\langle F_{\rm ac} \rangle \big|_{z_{\rm top}}$ are the modules of $\langle \boldsymbol{F_{\rm ac}} \rangle \big|_z$ at the bottom and top of the box, respectively. Finally, the total acoustic power generated per unit area within the box is:

$$E_{\rm ac,box} \equiv W_{\rm ac,box} / S_{\rm box} = \langle F_{\rm ac} \rangle \big|_{z_{\rm bot}} - \langle F_{\rm ac} \rangle \big|_{z_{\rm top}} \tag{4.9}$$

The first and last 5 horizontal sections of the box should not be considered as physically informative, since they are *ghost zones* — i.e., layers used to enforce boundary conditions for high-order derivatives in the vertical direction (Magic et al. 2013). The "bottom" and "top" layers of equation (4.9) refer to the 3D cube already deprived of these boundary zones.

[1] Assuming $\frac{\partial \delta S}{\partial t} = 0$ is not fully self-consistent with the use of 3D hydrodynamic simulations. In fact, the energy exchange between convection and propagating sound waves is considered by the code while solving the 3D hydrodynamic equations. However, accounting for these effects in the present analysis would be very complicated and out of this project's reach. The Cowling approximation is instead a very common approach in asteroseismology and consists in neglecting the perturbation of the gravitational potential. This is reasonable for modes with high angular degree l or high radial order n, which indeed have a small Φ' (J. Christensen-Dalsgaard 2014).

4.3.2 Dependence on stellar properties

After having computed $E_{\rm ac,box}$ for each simulated atmosphere of the grid, I studied how this quantity changes with stellar properties. In particular, for each fixed [Fe/H], I analyzed how $E_{\rm ac,box}$ changes across the plane ($\log T_{\rm eff}$, $\log g$). On the other hand, for each pair of fixed ($\log T_{\rm eff,target}$, $\log g$), I studied the behaviour of $E_{\rm ac,box}$ with [Fe/H].

Let me first present how $E_{\rm ac,box}$ changes across the plane ($\log T_{\rm eff}$, $\log g$), at fixed [Fe/H]. These graphs are reported from figure 4.4 to 4.10. For the most metal-rich models — [Fe/H] = -0.5, 0.0, $+0.5$ — we can note that $\log E_{\rm ac,box}$ is almost constant with $\log g$ and *linearly* increasing with $\log T_{\rm eff}$. This evidence is less clear for the most metal-poor models — [Fe/H] = -4.0, -3.0, -2.0, -1.0 — where points are more scattered, therefore showing a less tight correlation. In the light of these results, it is reasonable to think that the total acoustic power per unit area could depend on g and $T_{\rm eff}$ through a *power law*:

$$\log E_{\rm ac,box} = \log A + \alpha \log g + \beta \log T_{\rm eff} \quad \Longrightarrow \quad E_{\rm ac,box} = A g^{\alpha} T_{\rm eff}^{\beta} \tag{4.10}$$

where A is the normalization, α is expected to be close to 0 and $\beta > 0$. At each fixed [Fe/H], I performed a three-parameter, linear fit on the $(\log T_{\rm eff}, \log g)$ plane — with $T_{\rm eff}$ being the actual effective temperature, not the targeted value. The unknown parameters are the logarithm of the normalization $\log A$ and the exponents α and β. The power law (4.10) has been considered as the model to be fitted. The best-fit parameters are reported in table 4.2.

[Fe/H]	**Best-fit parameters**		
	$\boldsymbol{\log A}$	$\boldsymbol{\alpha}$	$\boldsymbol{\beta}$
-4.0	-5.10 ± 2.10	$+0.10 \pm 0.04$	$+3.76 \pm 0.57$
-3.0	-1.59 ± 1.81	$+0.14 \pm 0.04$	$+2.79 \pm 0.51$
-2.0	-1.67 ± 1.55	$+0.18 \pm 0.03$	$+2.77 \pm 0.43$
-1.0	-6.66 ± 1.39	$+0.10 \pm 0.03$	$+4.17 \pm 0.39$
-0.5	-8.21 ± 1.15	0.00 ± 0.03	$+4.68 \pm 0.33$
0.0	-11.1 ± 0.9	-0.05 ± 0.02	$+5.52 \pm 0.27$
$+0.5$	-9.57 ± 1.48	0.00 ± 0.03	$+5.06 \pm 0.43$

Table 4.2: Best-fit parameters for the power law (4.10), at fixed metallicity.

Now, I discuss the variation of $E_{\rm ac,box}$ with [Fe/H], at fixed $(\log T_{\rm eff,target}, \log g)$. For *all* the models, the acoustic energy does not show relevant variations with [Fe/H]. I report two examples in 4.11, where we can see that $\log E_{\rm ac,box}$ is *almost flat* with [Fe/H]. This result suggests that [Fe/H] does not have a direct impact on the acoustic energy, at fixed $(\log T_{\rm eff,target}, \log g)$. For this reason, I consider the power laws reported in 4.2 as the definitive relations linking the acoustic energy per unit area $E_{\rm ac,box}$ with the stellar parameters, to be used in the construction of the FPR3D models (see section 4.4).

4.3.3 How the global acoustic power scales with L and M

As explained above, calculating the global acoustic power $L_{\rm ac}$ just by using the properties of 3D hydrodynamic simulations is unfeasible. However, surface gravity g and effective temperature $T_{\rm eff}$ *are not independent along the RGB*. Considering a relation directly linking g with $T_{\rm eff}$ allows to derive a scaling relation for $L_{\rm ac}$ as a function of M and L, as I explain below. This information, combined with equation (3.2), can give us a first qualitative idea on the location along the RGB where most of the mass is expected to be lost by the star, if the acoustic energy per unit area $E_{\rm ac,box}$ coming from 3D hydrodynamic simulations is used.

Belkacem et al. (2013) report a scaling relation obtained with the stellar evolution code CESTAM and linking the surface gravity with the effective temperature along the RGB, which reads:

$$T_{\rm eff} \propto g^{0.07} \tag{4.11}$$

This information, together with the definition of surface gravity and the Stefan-Boltzmann law for the stellar luminosity

$$\begin{cases} g = \frac{GM}{R^2} \\ L = 4\pi R^2 \sigma T_{\rm eff}^4 \end{cases} \tag{4.12}$$

can be used to express the stellar radius R, g and $T_{\rm eff}$ as a function of L and M along the RGB:

$$R \propto \frac{L^{0.69}}{M^{0.19}} \quad ; \quad T_{\rm eff} \propto \left(\frac{L}{M}\right)^{-0.097} \quad ; \quad g \propto \left(\frac{L}{M}\right)^{-1.38} \tag{4.13}$$

Now, if we neglect the generation of acoustic waves in regions deeper than the maximum radial extension of the 3D box and assume that the 3D box is replicable over the whole stellar surface, the total acoustic power $L_{\rm ac}$ is related to the acoustic power per unit area as:

$$L_{\rm ac} = 4\pi R^2 E_{\rm ac} \tag{4.14}$$

where $E_{\rm ac}$ is the acoustic power per unit area, considering the whole stellar surface, which under the above assumption is equal to $E_{\rm ac,box}$. Equation (4.14), combined with the power law (4.10), gives:

$$L_{\rm ac} \propto R^2 g^\alpha T_{\rm eff}^\beta \tag{4.15}$$

I still adopt the structure of the FPR prescription and therefore assume that the global acoustic power is related to the mass loss rate as written in equation (3.2). Therefore, by plugging (4.15) in that relation, we have:

$$\dot{\mu} \propto -\frac{R}{M} L_{\rm ac} \propto -\frac{R^3}{M} g^\alpha T_{\rm eff}^\beta \tag{4.16}$$

Finally, using the three proportionalities (4.13), we obtain a scaling relation which links the idealized $\dot{\mu}$ with mass and luminosity:

$$\dot{\mu} \propto -\frac{L^{2.07}}{M^{1.57}} \left(\frac{L}{M}\right)^{\mathcal{Q}(\alpha,\beta)} \tag{4.17}$$

where $\mathcal{Q}(\alpha,\beta) \equiv -1.38\alpha - 0.10\beta$. The best-fit exponents α and β reported in table 4.2 can be used to define a pair of characteristic values for α and β to evaluate $\mathcal{Q}(\alpha,\beta)$. As

representative values, I assume $\alpha \approx 0$ and $\beta \approx 4$, which therefore imply $\mathcal{Q}(\alpha, \beta) \approx -0.4$. Finally, we can see that:

$$\dot{\mu} \propto -\frac{L^{1.67}}{M^{1.17}} \tag{4.18}$$

Note the dependence on the stellar luminosity: again, even using the acoustic energy from 3D hydrodynamic simulations, we expect most of the mass loss to be concentrated on the highest-luminosity portion of the RGB. Also, the stellar mass has the same effect as in the standard FPR prescription: stars with a higher initial mass are expected to have smaller mass loss rates.

I would like to stress again that R, M and L are not known quantity in the STAGGER grid models. I made this discussion only to derive the qualitative expected trend of the RGB mass loss rate with mass and luminosity, if the acoustic energy from 3D simulations is plugged in the structure of the FPR prescription.

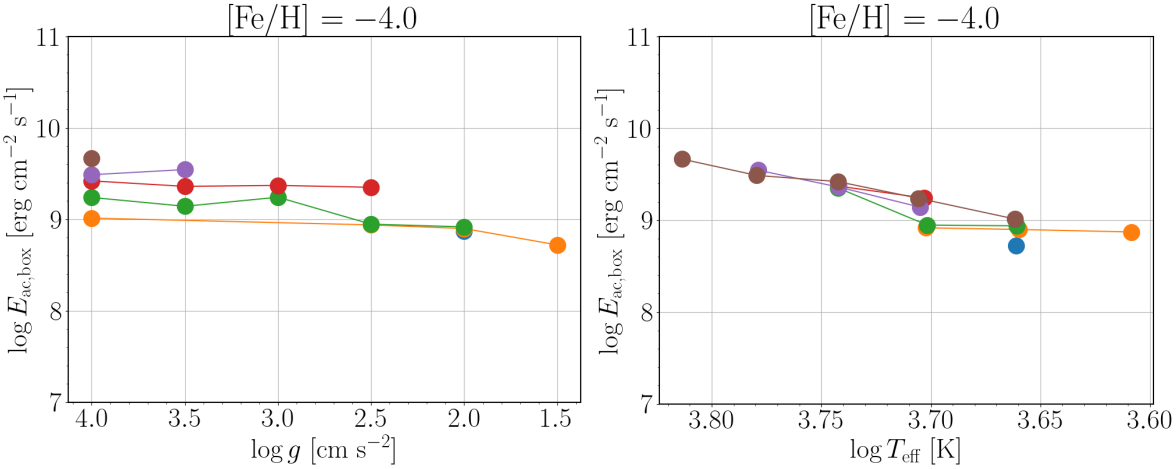

Figure 4.4: Variation of the acoustic power per unit area $E_{\rm ac,box}$ across the plane ($\log T_{\rm eff}$, $\log g$), at fixed [Fe/H] = −4.0. *Left panel*: logarithm of $E_{\rm ac,box}$ as a function of $\log g$, at different effective temperatures. For a better visualization, models having the same targeted effective temperature have been grouped under the same color: blue: 4000 K, orange: 4500 K, green: 5000 K, red: 5500 K, purple: 6000 K, brown: 6500 K. *Right panel*: logarithm of $E_{\rm ac,box}$ as a function of $\log T_{\rm eff}$, at different $\log g$: blue: 1.5, orange: 2.0, green: 2.5, red: 3.0, purple: 3.5, brown: 4.0.

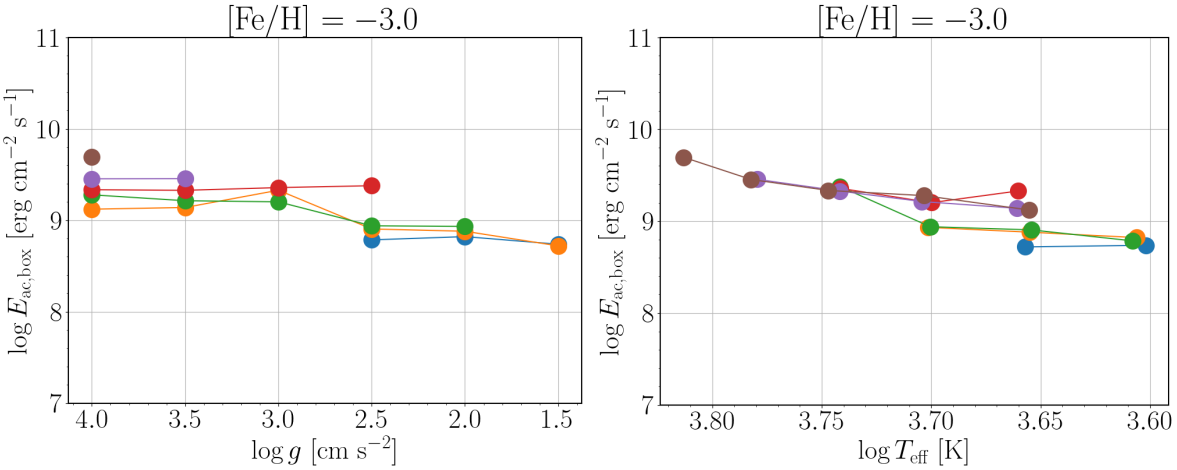

Figure 4.5: Same as figure 4.4, but at fixed [Fe/H] = −3.0.

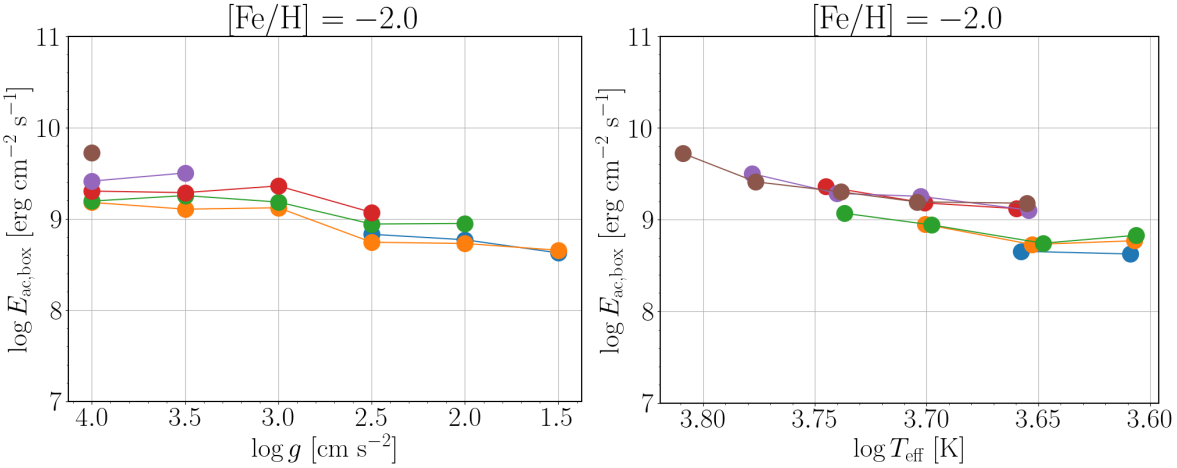

Figure 4.6: Same as figure 4.4, but at fixed [Fe/H] = −2.0.

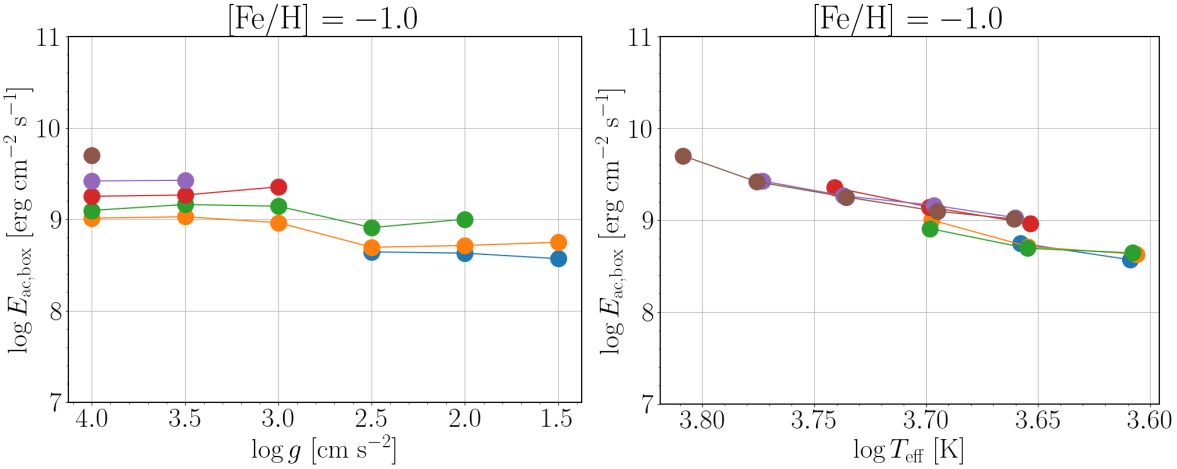

Figure 4.7: Same as figure 4.4, but at fixed [Fe/H] = −1.0.

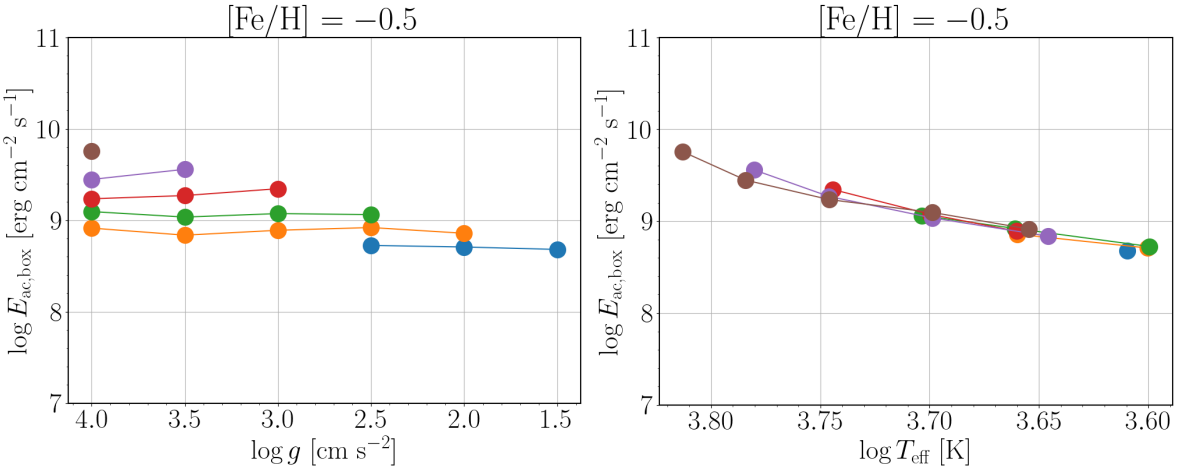

Figure 4.8: Same as figure 4.4, but at fixed [Fe/H] = −0.5.

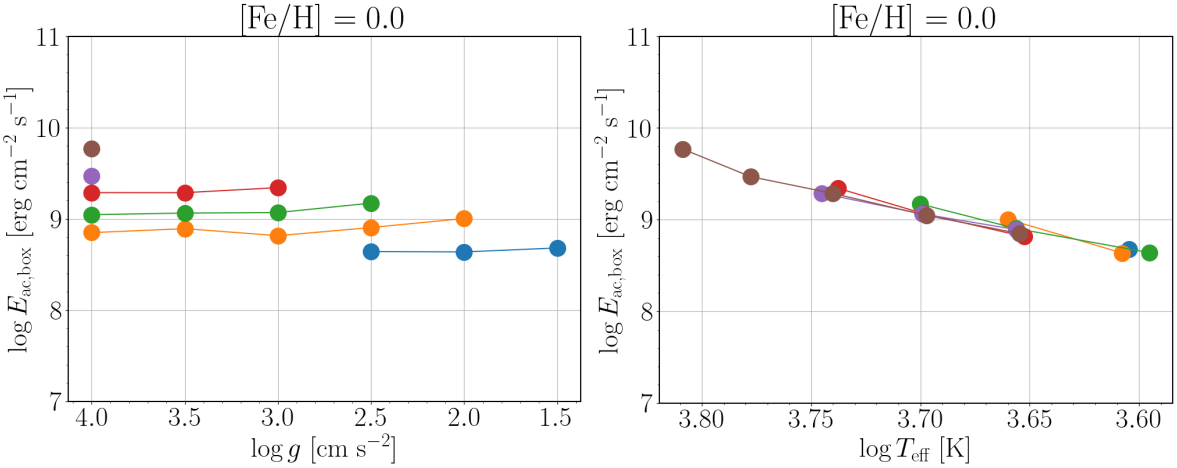

Figure 4.9: Same as figure 4.4, but at fixed [Fe/H] = 0.0.

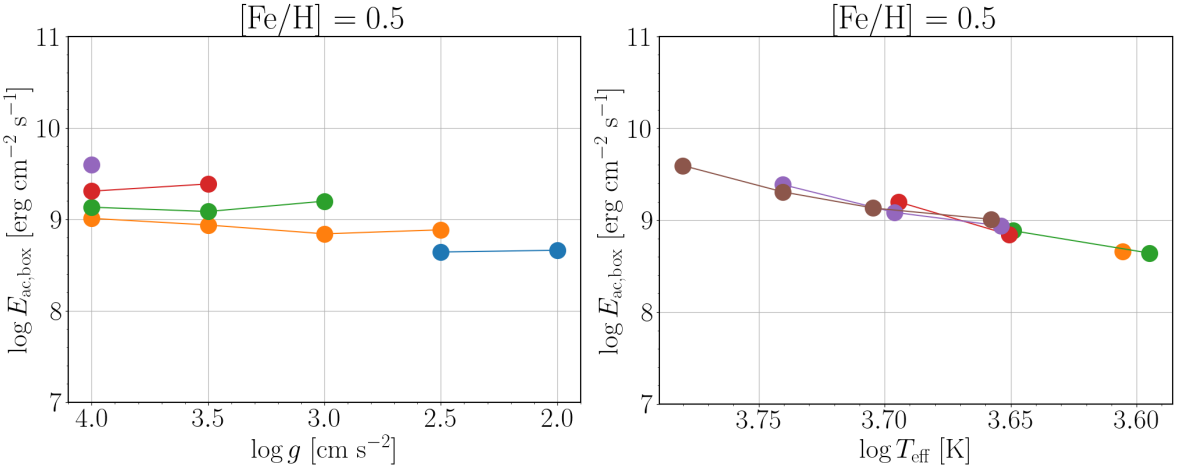

Figure 4.10: Same as figure 4.4, but at fixed [Fe/H] = +0.5.

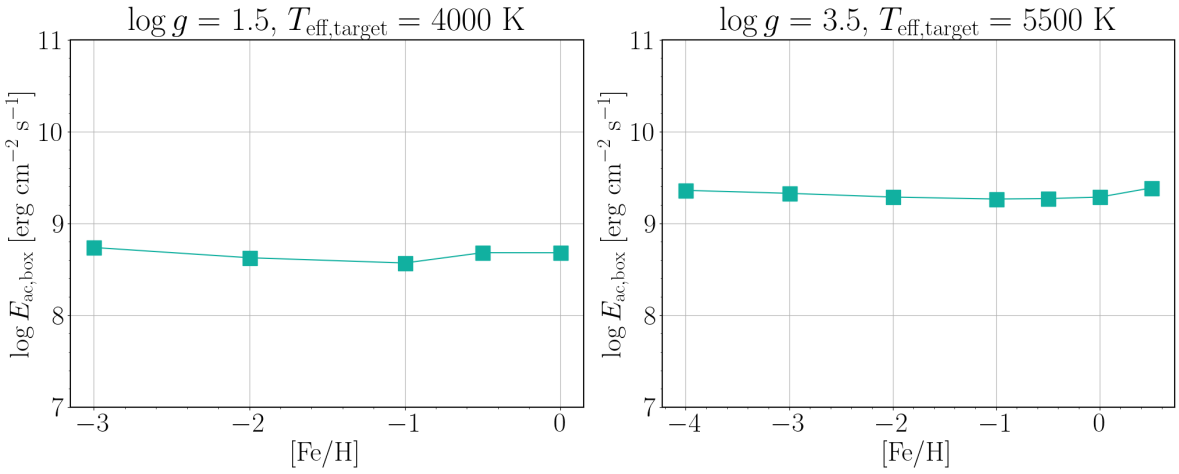

Figure 4.11: Variation of the logarithm of the acoustic power per unit area $E_{\mathrm{ac,box}}$ against [Fe/H], at fixed surface gravity g and targeted effective temperature $T_{\mathrm{eff,target}}$. *Left panel*: $\log g = 1.5$ and $T_{\mathrm{eff,target}} = 4000\,\mathrm{K}$. *Right panel*: $\log g = 3.5$ and $T_{\mathrm{eff,target}} = 5500\,\mathrm{K}$.

4.4 Implementation of the FPR3D mass loss

While it is not possible to obtain the stellar radius R in 3D hydrodynamic simulations of the STAGGER grid, it is instead relatively simple to access the stellar radius in 1D codes of stellar evolution. In fact, in the particular case of MESA, the radius R can be accessed from inside the script `run_star_extras.f90`, which is called at each timestep by the code (see section 3.2 for more details). This allows me to explain the idea behind the FPR3D models: taking the expression for the acoustic power per unit area from 3D hydrodynamic simulations of the STAGGER grid and use it to compute $L_{\rm ac}$ at each timestep of the evolution calculated by MESA. Here is the adopted methodology:

The choices on [Fe/H]. The covered range in [Fe/H] for the FPR3D grid has been constructed on the basis of the available [Fe/H] of the STAGGER models, with the exception of the two most metal-poor ([Fe/H] = −4.00, −3.00) and the most metal-rich ([Fe/H] = +0.50). Therefore, the covered range in the iron abundance for the FPR3D grid models is [Fe/H] = −2.00, −1.00, −0.50, 0.00. I opted not to calculate models with [Fe/H] = −4.00 and [Fe/H] = −3.00 because these stars would have a very low metallicity which is not even observed in the most metal-poor stellar populations. On the other hand, [Fe/H] = +0.5 is above the capability of MESA, since the upper limit to the mass fraction of metals Z is 0.04, which corresponds to [Fe/H] $\simeq$ 0.41 according to equation (3.24).

To be consistent with the α-enhancement adopted in the STAGGER grid models (see section 4.2), I used the options already described in section 3.2 for the standard FPR grid. The opacity tables and metal mixture are identical for both the standard FPR and FPR3D grids. This is essential because it ensures comparability between the two prescriptions. Therefore, any difference between the mass-loss predictions of standard FPR and FPR3D cannot be ascribed to a different treatment of opacity or metal mixture.

Computation of the mass loss rate. Concerning the computation of the mass loss rate, the following steps have been considered:

- implement four different scripts `run_star_extras.f90`, each corresponding to a single [Fe/H] of the covered range −2.00, −1.00, −0.50, 0.00. In these scripts, the acoustic power per unit area is computed by using the power law (4.10), at each timestep of the evolution. The normalization A and the exponents α and β are taken from table 4.2, on the basis of the considered [Fe/H];

- neglect any other contribution to the generation of acoustic waves coming from regions deeper than those probed by the vertical size of the STAGGER 3D boxes;

- assume this acoustic power per unit area to be a *universal* property of the star. In other words, the information extracted from 3D simulations of the STAGGER grid is assumed to be *representative* of the near-surface layers across the entire spherical surface of the star ($E_{\rm ac} = E_{\rm ac,box}$);

- the two assumptions above enable the calculation of the global acoustic power $L_{\rm ac}$ just by doing $L_{\rm ac} = 4\pi R^2 E_{\rm ac}$, at each timestep of the evolution;

- this value of $L_{\rm ac}$ is then plugged in equation 3.2 to compute the upper limit to the mass loss rate $\dot{\mu}$;
- this upper limit is then scaled by the same efficiency factor $\eta_{\rm FPR} = 3.6 \times 10^{-4}$ used for the standard FPR grid, to have the actual mass loss rate $\dot{M}$.

Common settings. Except for the iron abundances [Fe/H] and the computation of the mass loss rate, I constructed the FPR3D grid using the same settings and initial parameters as those of the standard FPR grid (described in section 3.2). Considering the restricted range of [Fe/H] covered by the FPR3D grid, the number of models totals to 48 (against 72 of the standard FPR grid).

4.4.1 The properties of FPR3D models

As expected on the basis of the qualitative argument of section 4.3.3, the FPR3D mass loss is concentrated in the very top part of the RGB, as shown in the example of figure 4.12. This is caused by the increase of luminosity near the tip of the RGB, which leads to high mass loss rates (in absolute value) according to equation 4.18.

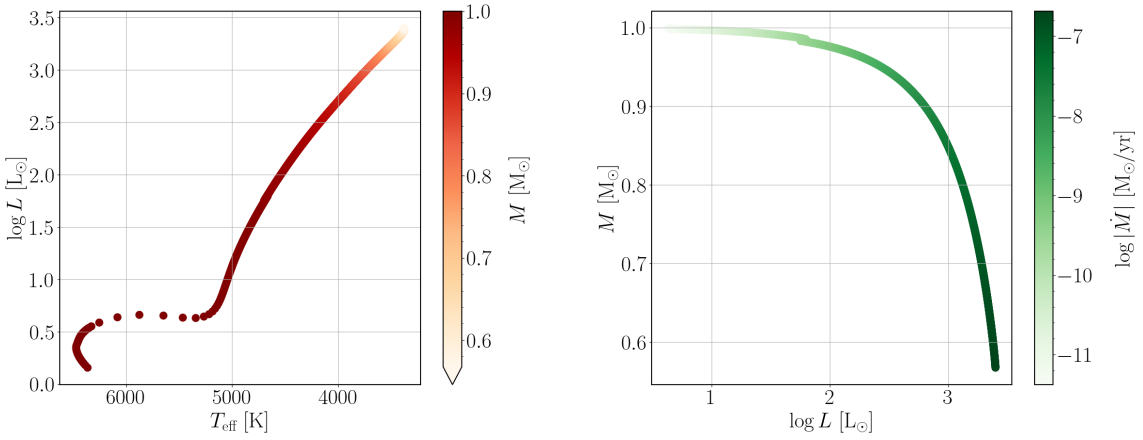

Figure 4.12: Same as 3.1, but with the use of the FPR3D mass loss prescription.

Only 10 models exceeded the maximum threshold set for the stellar age (16 Gyr). Among the remaining 38 models, 27 reached the ZACHeB and 11 ended their evolution as helium WDs. We can note in figure 4.13b that various models experienced a late He flash, compared to only one such model in the standard FPR grid.

The variation of the integrated RGB mass loss against different chemical compositions is reported in the panels of figure 4.14:

- for all the models having reached the ZACHeB, at fixed [Fe/H], we can note again that an increase of Y leads to smaller total RGB mass loss. This is particularly clear for the models with $M_{\rm in} = 0.9,\ 1.0\,{\rm M}_\odot$ and [Fe/H] $= -2.00,\ -1.00$, where ΔM still appears to decrease linearly with Y. This result is similar to what has been obtained for the standard FPR models;

- at fixed Y, the trend of ΔM with [Fe/H] is a *monotonic increase*. This is the major difference between the FPR3D models and the standard FPR's, where ΔM increases with [Fe/H] until a value of [Fe/H] $\simeq -0.5$, above which the opposite trend is observed;

- low-metallicity stars are characterized by a total RGB mass loss comparable to that of the standard FPR analogs (see figure 3.4). Instead, FPR3D models with [Fe/H] $= -0.5$ and [Fe/H] $= 0.0$ show a systematically higher ΔM.

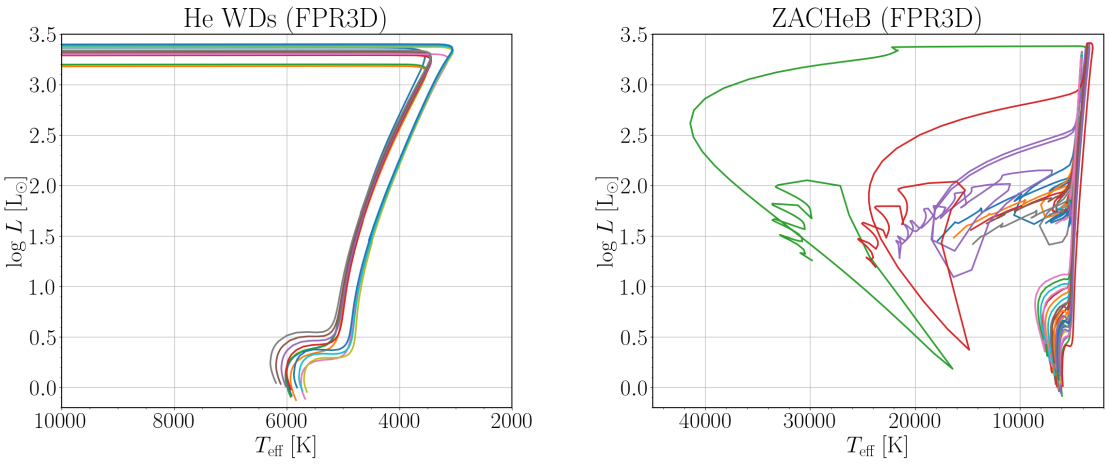

(a) (b)

Figure 4.13: Evolutionary tracks on the HR diagram (from main sequence) of the FPR3D models. *Left panel*: models losing the entire convective envelope before the helium flash, thus becoming He white dwarfs. *Right panel*: models reaching the ZACHeB, either through a regular or late He flash.

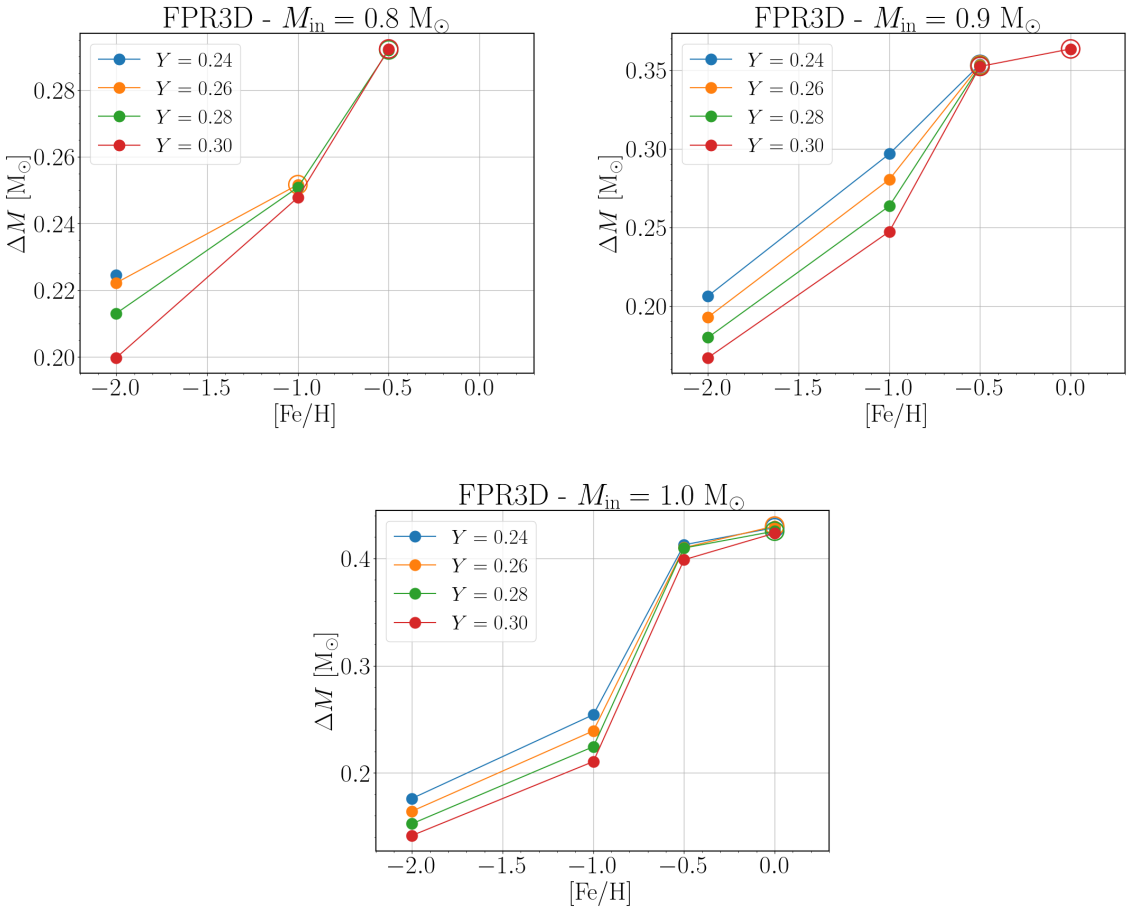

Figure 4.14: Same as figure 3.4, but for FPR3D models. The integrated RGB mass loss ΔM has been computed using the mass difference (3.28).

Chapter 5

Discussion and Conclusions

5.1 Comparison with Reimers' mass loss

In this section, I compare the results of the standard FPR and FPR3D models with a grid of 1D MESA simulations where the Reimers' mass loss was implemented (hereafter, this will be referred to as the "Reimers grid").

The Reimers efficiency factor $\eta_{\rm R}$ was fixed by adopting the following methodology:

1. considering a 1D model in MESA with $M_{\rm in} = 1.0\,{\rm M}_{\odot}$, initial $Y = 0.28$ and $Z = 0.02$, mixing length parameter $\alpha = 2$ and same overshooting settings mentioned in section 3.2;

2. running a standard FPR simulation with the parameters mentioned above and an efficiency factor $\eta_{\rm FPR} = 3.6 \times 10^{-4}$ (see section 3.2). Then, I computed the total RGB mass loss of such star by performing the mass difference (3.28), which resulted in $\Delta M = 0.2210\,{\rm M}_{\odot}$;

3. performing another 1D simulation with the same settings mentioned in point 1, but using the Reimers' mass loss rate (equation 1.11). The efficiency factor $\eta_{\rm R}$ was *calibrated* to obtain the same total RGB mass loss of the standard FPR model mentioned in point 2. The use of an efficiency factor $\eta_{\rm R} = 0.387$ could reproduce such integrated mass loss, as shown in figure 5.1.

This efficiency factor $\eta_{\rm R} = 0.387$ was adopted for all the models of the Reimers grid to calculate the mass loss rate at each timestep of the evolution, by using the relation (1.11).

All the other settings and parameters of the Reimers grid are the same as the standard FPR's, therefore I refer to section 3.2 for a complete description.

Even for the models of the Reimers grid, the largest fraction of the stellar mass is lost over the very last portion of the RGB (see figure 5.2). This was expected, as already mentioned in section 1.2.2. Therefore, the first evident result shared by all the 3 different mass loss rates considered in this project is that most of the mass loss occurs over the rapid evolutionary phases prior to the He flash. However, the total RGB mass loss in the models of the Reimers grid is overall less than the standard FPR and FPR3D analogs (except for models with [Fe/H] = 0.00 and [Fe/H] = +0.20). This can be noted by the fact that *no star* of the Reimers grid lost its whole envelope before reaching the RGB tip: 52 models out of 72 reached the ZACHeB through a regular He flash (see figure 5.3), while the remaining exceeded the maximum age of 16 Gyr.

The two models with $M_{\rm in} = 1.0\,{\rm M}_\odot$, [Fe/H] = +0.20 and $Y = 0.28, 0.30$ have the same numerical problems at the He flash described for the standard FPR analogs. For the same reasons explained in section 3.2.2, these two models were included in the current analysis and truncated at the beginning of the He flash.

In figure 5.4 we can study the variation of the total RGB mass loss ΔM with initial Y and [Fe/H] for the models of the Reimers grid.

- at fixed [Fe/H], we can note the same property observed for the standard FPR and FPR3D models: the total RGB mass loss *linearly* decreases with initial He abundance Y;
- at fixed Y, the total RGB mass loss ΔM *monotonically* increases with [Fe/H]. This was indeed expected, according to the considerations given in section 1.2.2.

To facilitate the comparison between the three different mass loss prescriptions, I superimpose the results of the standard FPR, FPR3D and Reimers models in the graphs 5.5, 5.6, 5.7. I discuss this comparison in sections 5.2 and 5.3.

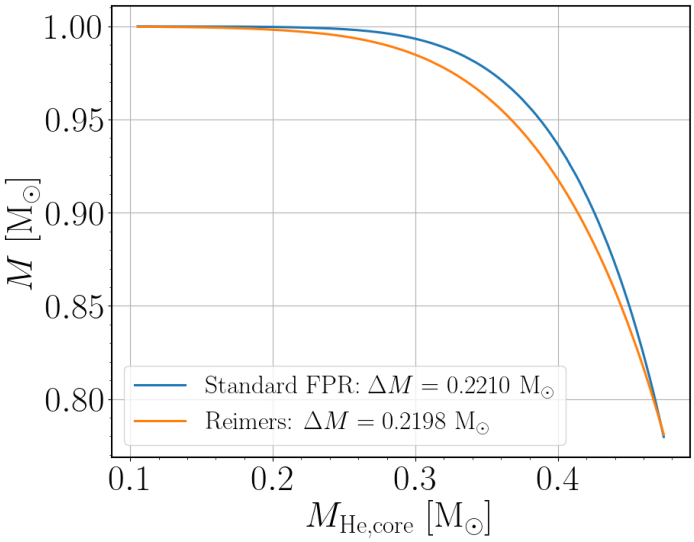

Figure 5.1: Stellar mass as a function of the mass of the He core. The initial parameters are $M_{\rm in} = 1.0\,{\rm M}_\odot$, $Y = 0.28$ and $Z = 0.02$. The blue curve refers to the standard FPR model, whereas the orange line refers to the model where the Reimers' mass loss was implemented. The efficiency factors for the standard FPR and Reimers' mass loss are set to $\eta_{\rm FPR} = 3.6 \times 10^{-4}$ and $\eta_{\rm R} = 0.387$, respectively. The total RGB mass loss corresponding to each model is reported in the legend.

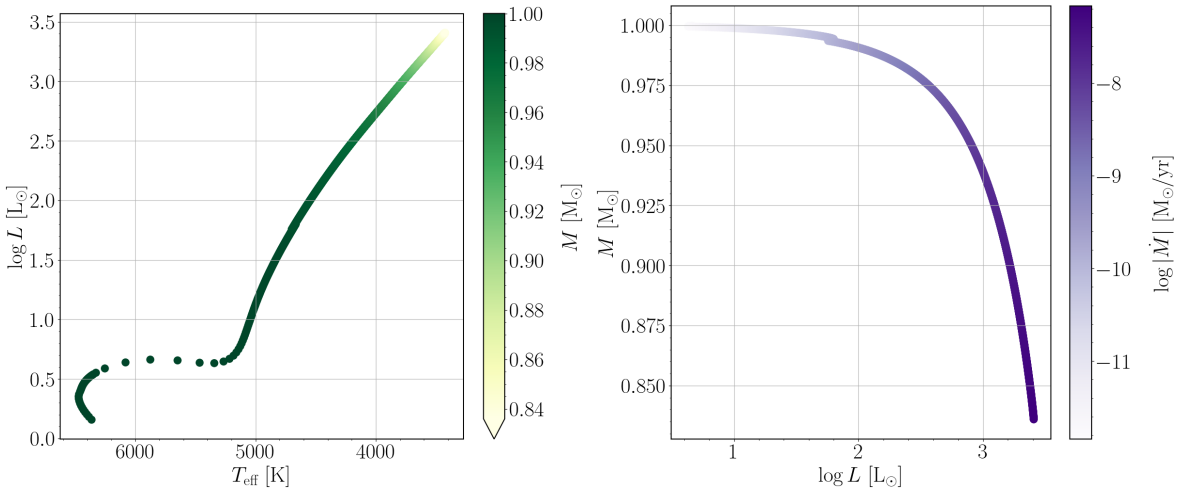

Figure 5.2: Same as figure 3.1, but with the use of the Reimers' mass loss law.

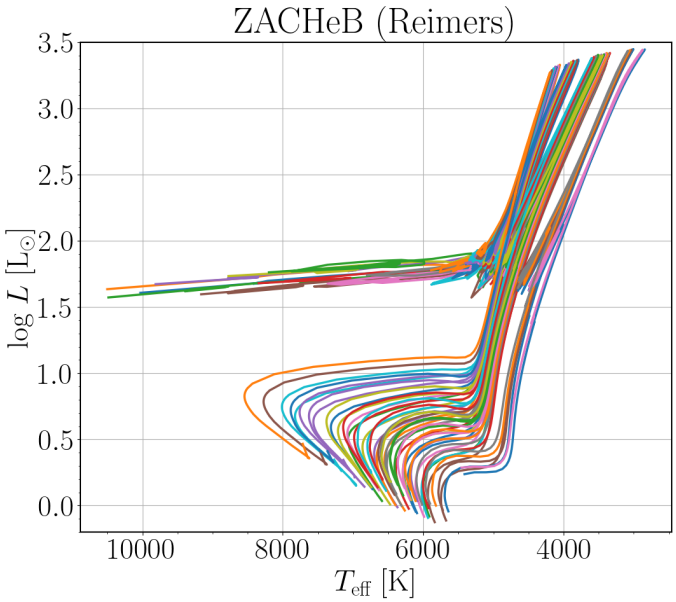

Figure 5.3: Evolutionary tracks on the HR diagram (from main sequence) of the Reimers grid models that reached the ZACHeB and did not exceed the maximum threshold of 16 Gyr for the stellar age.

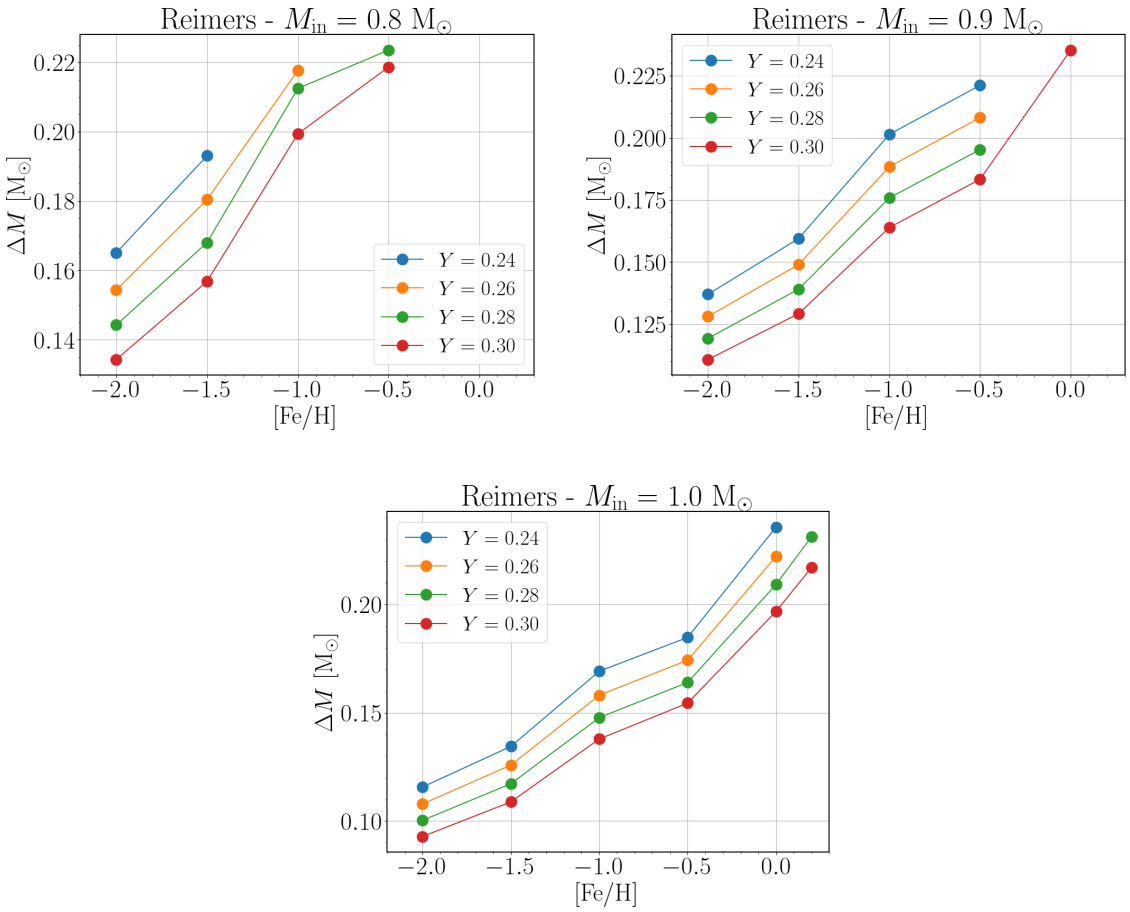

Figure 5.4: Same as figure 3.4, but for the models of the Reimers grid.

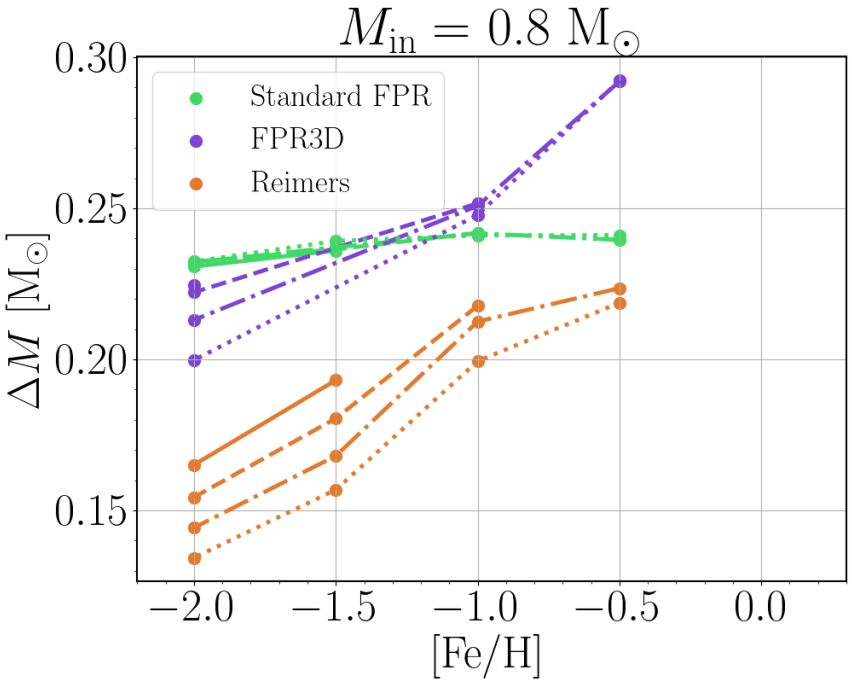

Figure 5.5: Comparison of the total RGB mass loss as a function of [Fe/H] for models with initial mass $M_{\rm in} = 0.8\,{\rm M}_\odot$, at different initial He abundances Y. The lines connect stars that either reached the ZACHeB or lost their whole envelope, ending their evolution as He WDs. The missing points are stars that reached the maximum threshold for the stellar age of 16 Gyr. Solid lines connect models with initial $Y = 0.24$; dashed: $Y = 0.26$; dot-dashed: $Y = 0.28$; dotted: $Y = 0.30$. Green: standard FPR models; purple: FPR3D models; orange: Reimers models.

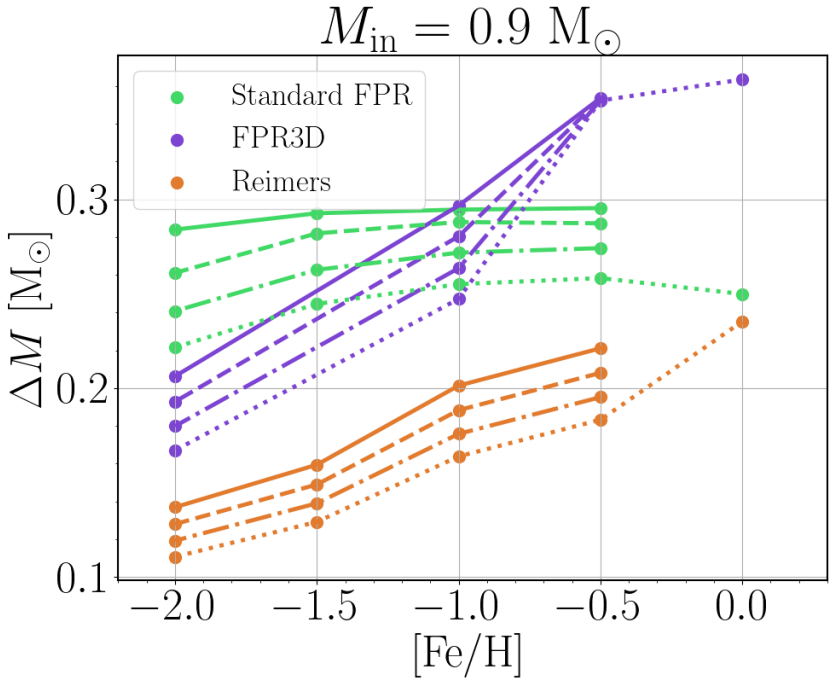

Figure 5.6: Same as figure 5.5, but for models with initial mass $M_{\rm in} = 0.9\,{\rm M}_\odot$.

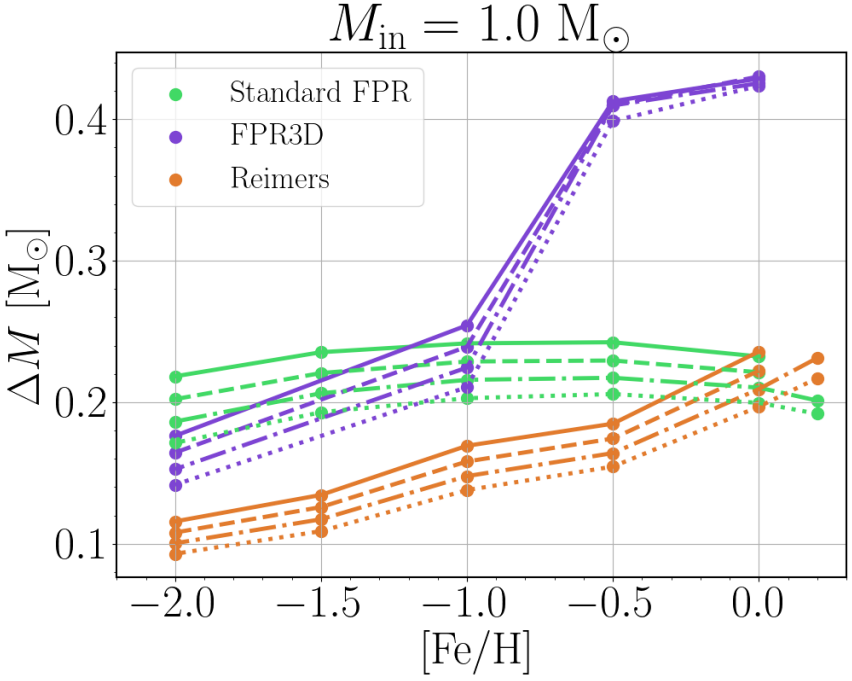

Figure 5.7: Same as figure 5.5, but for models with initial mass $M_{\rm in} = 1.0\,{\rm M}_\odot$.

5.2 The effect of [Fe/H] on the total RGB mass loss

The three mass loss prescriptions have substantially different trends of the total mass loss ΔM against variations in [Fe/H], at fixed Y. The only property shared by standard FPR, FPR3D and Reimers models is an *increase* of the total RGB mass loss ΔM until [Fe/H] $\simeq -1.00$. Above this value, substantially different trends are found: the standard FPR prescription shows a flattening, followed by a decreasing behaviour, whereas the Reimers and FPR3D prescriptions continue to manifest an increase of ΔM with [Fe/H]. The results obtained with the standard FPR grid would support the hypothesis mentioned in section 1.2.2 about the possibility of a non-monotonic trend of ΔM claimed by K. Brogaard et al. (2024) and Li (2025), whereas the FPR3D grid shows a monotonically increasing trend with [Fe/H], which is instead closer to what Reimers' mass loss predicts.

The total RGB mass loss varies with [Fe/H] for two reasons:

- the He flash occurs at higher luminosity when [Fe/H] increases, thus contributing to more mass loss because the star takes more time to complete the final part of the RGB and, in addition, it suffers from even higher mass loss rates (in absolute value) while ascending this additional portion at the top of the RGB;

- since the last portions of the RGB are characterized by the highest mass loss rates, any small variation of $\dot{M}$ over the last few million years prior to the He flash is crucial in determining the final mass of the star at the end of the RGB. The way [Fe/H] impacts on $\dot{M}$ over these stages is different between stars of the standard FPR, FPR3D and Reimers grids. Understanding the origin of these differences is made particularly difficult by the fact that *metallicity is not an explicit parameter* involved in the computation of the mass loss rate $\dot{M}$, in any of the three examined mass loss prescriptions.

In view of the considerations above, I have not further analyzed the influence of [Fe/H] on mass loss, since this would require a very detailed study on how metallicity changes the stellar structure and the evolutionary timescales over the last few million years before the He flash. This will be matter of study for the future developments of this work.

Among the three mass-loss predictions examined in this work, the most intriguing result is the trend of the total RGB mass loss against [Fe/H] found in the standard FPR grid. In fact, as already mentioned in section 1.2.2, recent studies have claimed that ΔM increases with [Fe/H] in the low-metallicity regime, then inverting the trend above a certain value of [Fe/H] (K. Brogaard et al. 2024; Li 2025). Interestingly, the trend found for the standard FPR models (figure 3.4) is similar to that shown in figure 5.8, where it is reported the integrated RGB mass loss estimated in different stellar populations and using independent techniques. Indeed, in the standard FPR diagrams and in figure 5.8, it is possible to recognize an increase of ΔM in the low-metallicity regime, followed by a decrease for [Fe/H] $\gtrsim -0.5$. I will further investigate the origin of this peculiar trend found in the standard FPR models, which currently remains obscure.

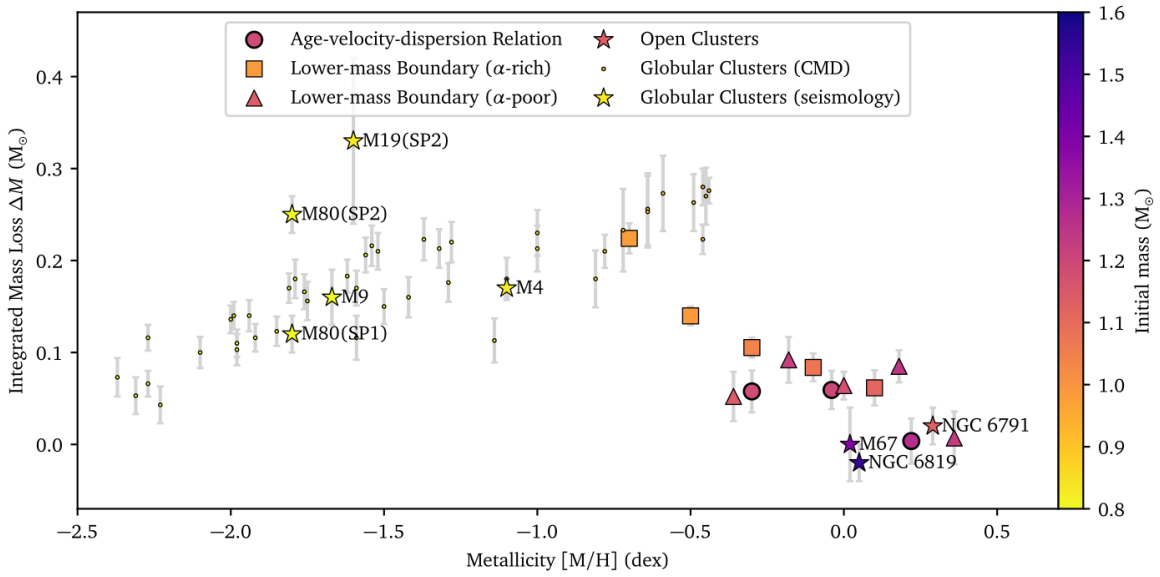

Figure 5.8: *Adapted from figure 7 in Li (2025).* Integrated mass loss along the RGB versus metallicity, color-coded by initial mass. The estimates of the integrated RGB mass loss come from independent techniques, as indicated in the legend. For the estimates obtained from globular clusters, see the references cited by Li (2025). A detailed explanation of the other observational techniques can be found in the same work.

5.3 The effect of Y on the total RGB mass loss

The fact that the total RGB mass loss ΔM linearly decreases with initial He abundance Y (at fixed [Fe/H]) is evident in almost all the models, with the exception of stars with $M_{\rm in} = 0.9, 1.0\,{\rm M}_\odot$, [Fe/H] $= -0.5, 0.0$ of the FPR3D grid and of the models with initial mass $M_{\rm in} = 0.8\,{\rm M}_\odot$ of the standard FPR and FPR3D grids (see figures 5.5, 5.6 and 5.7). This linear decrease of the total RGB mass loss ΔM with initial Y originates from the influence of He on the evolutionary timescales preceding the RGB tip. Indeed, the impact of the He abundance on the cumulative mass lost along most of the RGB is very mild. In this section, I describe the analysis I have performed to achieve these conclusions.

In figure 5.9, as a reference, I report three examples relative to the evolution of the mass loss rate along the RGB, in the standard FPR, FPR3D and Reimers grids. Analogous results are found for other initial masses and different fixed [Fe/H]. We can note that the impact of Y on the mass loss rate is small and confined in the lowest portion of the RGB (below the RGB bump). In particular, an increased Y seems to generate a slightly higher $|\dot{M}|$. While approaching the tip, even these subtle differences reduce and all stars converge to almost the same mass loss rates. However, it has to be noted that these stars have significantly different ages at the RGB tip: from $Y = 0.24$ to $Y = 0.30$ (with a step $\Delta Y = +0.02$), the age at the tip is $t_{\rm age,tip} = 7.84$, 6.87, 6.01 and 5.25 Gyr. Given their shorter evolutionary timescales along the RGB, it is reasonable to suggest that the total mass loss of He-rich stars might be *less* than He-poor stars', though having a slightly higher $|\dot{M}|$ over most of the RGB. Could this be the explanation to the linear decrease of the total RGB mass loss ΔM with initial Y? To answer this question, we have to look closer at the very final stages of the evolution

— a few million years preceding the He flash — since this is the phase characterized by the highest mass loss.

From figure 5.10, we can see that the standard FPR, FPR3D and Reimers models share the same properties concerning the last few million years of the evolution along the RGB:

- let us consider the point when $|\dot{M}| = 10^{-8}\,\mathrm{M}_{\odot}\,\mathrm{yr}^{-1}$ (the zero-point on the abscissa). The cumulative mass lost up to that point is essentially the same, *regardless of the initial* Y. A very slight difference can be seen: up to the point when $|\dot{M}| = 10^{-8}\,\mathrm{M}_{\odot}\,\mathrm{yr}^{-1}$, He-poor stars have lost slightly more mass than He-rich stars. However, the differences are very subtle and negligible;

- for each curve, if we look at the value of $(M_{\mathrm{in}} - M)$ at the point when $|\dot{M}| = 10^{-8}\,\mathrm{M}_{\odot}\,\mathrm{yr}^{-1}$ and we compare it to $(M_{\mathrm{in}} - M)$ when the RGB phase ends, we can note that the vast majority of mass loss occurs over the last $\sim 4 - 5\,\mathrm{Myr}$ preceding the He flash. This timescale is 2 orders of magnitudes lower than the entire duration of the RGB: the stars examined in figures 5.9 and 5.10 take $\approx 490 - 710\,\mathrm{Myr}$ (from the most He-rich to the most He-poor star) to reach the RGB tip from the terminal age main sequence (TAMS);

- from the point when $|\dot{M}| = 10^{-8}\,\mathrm{M}_{\odot}\,\mathrm{yr}^{-1}$, He-rich stars take *less time* to reach the He flash than He-poor stars. We can see that, from the point when $|\dot{M}| = 10^{-8}\,\mathrm{M}_{\odot}\,\mathrm{yr}^{-1}$, the He flash is anticipated by $\approx 0.20 - 0.25\,\mathrm{Myr}$ for each increase in the initial He abundance $\Delta Y = +0.02$. This results in the smaller total mass loss already noted for all the three mass loss prescriptions. Finally, I can conclude that the linear decrease of the total RGB mass loss ΔM is due to the *shorter time* required for the star to reach the helium flash, if the initial He mass fraction Y is increased. The physical reasons behind this property can be found in Salaris and Cassisi (2005): He-rich stars have higher interior temperatures due to the increase in the mean molecular weight, which in turn implies a lower electron degeneracy level within the core, throughout the RGB. As a consequence, the star experiences the helium flash at lower He core mass. This explains the less time required to reach the He flash. Moreover, considering that the He core mass and the luminosity along the RGB are strictly correlated, a less massive He core at the flash implies a lower luminosity at the RGB tip (which is indeed found, see figure 5.11).

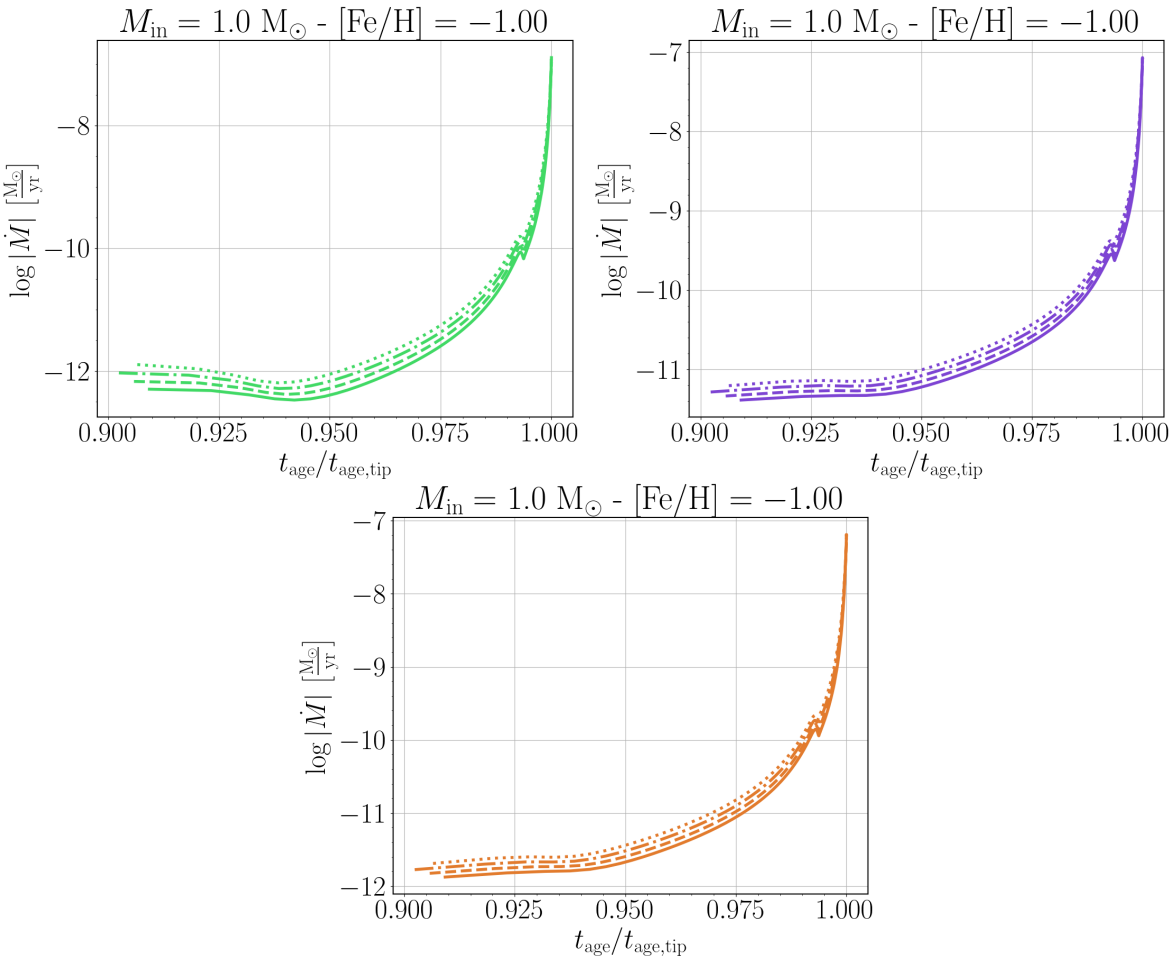

Figure 5.9: Logarithm of the absolute value of the mass loss rate as a function of age (from the beginning to the end of the RGB), normalized to the RGB-tip age. The examined stars have an initial mass of $M_{\rm in} = 1.0\,{\rm M}_\odot$ and [Fe/H] = −1.00. The solid curves refer to an initial $Y = 0.24$; dashed: $Y = 0.26$; dot-dashed: $Y = 0.28$; dotted: $Y = 0.30$. *Top-left panel*: standard FPR models. *Top-right panel*: FPR3D models. *Bottom panel*: Reimers models.

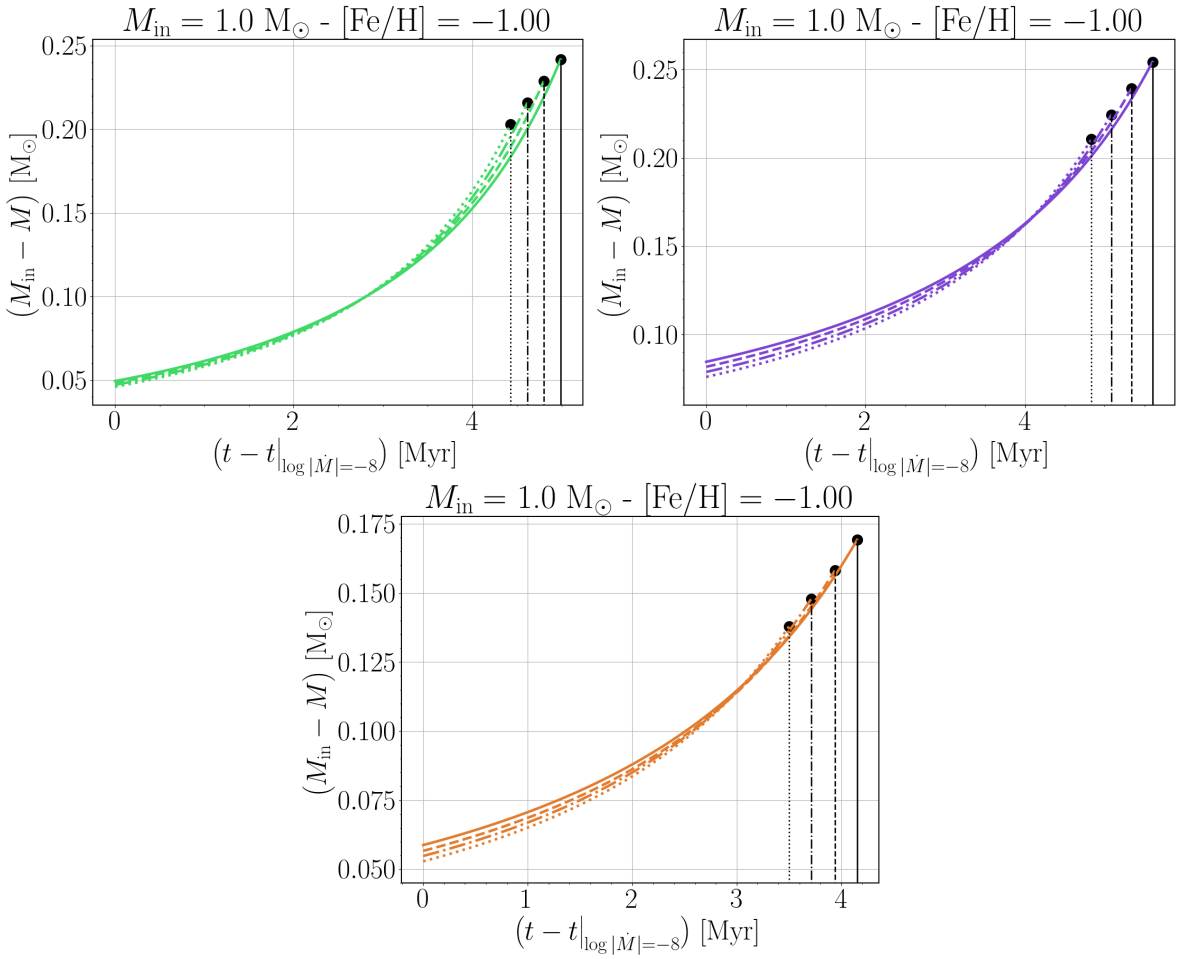

Figure 5.10: Cumulative mass loss $(M_{\rm in} - M)$ as a function of age, subtracted by the age of the star when $|\dot{M}| = 10^{-8}\,{\rm M}_\odot\,{\rm yr}^{-1}$. The examined stars have an initial mass of $M_{\rm in} = 1.0\,{\rm M}_\odot$ and [Fe/H] $= -1.00$. The solid curves refer to an initial $Y = 0.24$; dashed: $Y = 0.26$; dot-dashed: $Y = 0.28$; dotted: $Y = 0.30$. For each star, the black point and the associated vertical black line indicate the time when the star reached the RGB tip. *Top-left panel*: standard FPR models. *Top-right panel*: FPR3D models. *Bottom panel*: Reimers models.

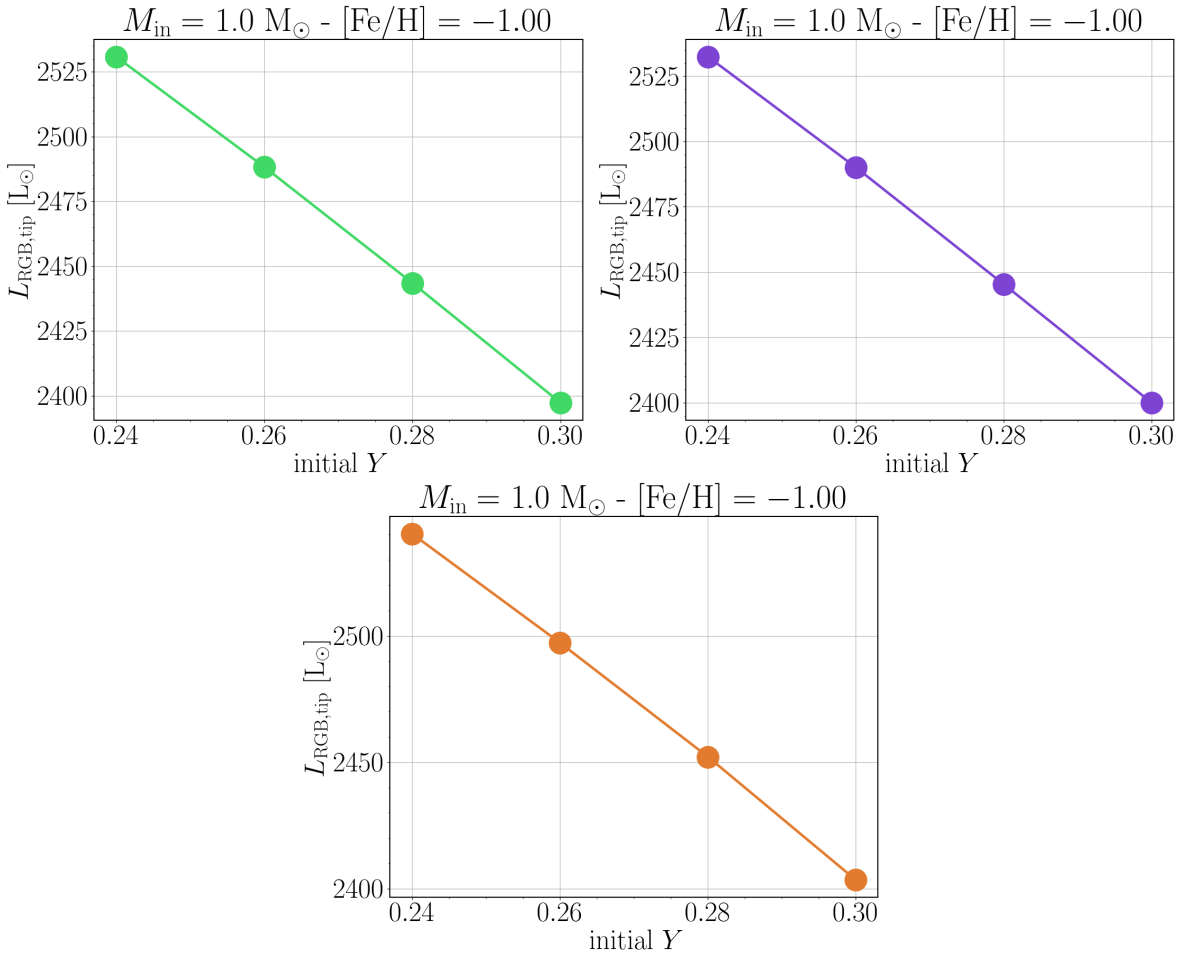

Figure 5.11: Luminosity at the RGB tip as a function of the initial He mass fraction Y, for stars with an initial mass of $M_{\rm in} = 1.0\,{\rm M}_\odot$ and [Fe/H] = −1.00. *Top-left panel*: standard FPR models. *Top-right panel*: FPR3D models. *Bottom panel*: Reimers models.

5.4 Limitations and future developments

5.4.1 Plan for the near-future work

In this section, I describe the planned steps that will be done in the near future on the basis of the work presented in this manuscript.

The impact of metallicity. The unclear dependence of the total RGB mass loss on [Fe/H] (for standard FPR and FPR3D models) will be further investigated. In particular, it will be analyzed the influence of [Fe/H] on the stellar structure and evolutionary timescales over the last few million years of the RGB phase, at fixed initial He abundance Y. Special focus will be placed on the standard FPR models, in order to study the reasons behind the decreasing trend of ΔM found for [Fe/H] $\gtrsim -0.5$, which resembles that obtained by Li (2025).

The role of the MLT parameter α. Studying the impact of α is important because it has a relevant influence on the stellar structure throughout its evolution. In particular, an increase in α leads to a higher effective temperature and a lower stellar radius throughout the entire RGB (up to the tip). Therefore, the MLT parameter α is expected to have a substantial indirect impact in modifying the total RGB mass loss. Moreover, for the particular case of the standard FPR prescription, the mixing length parameter directly enters in the expression for the acoustic power generated locally per unit volume (equation 3.4). These considerations support the idea of putting more effort in understanding the impact of the mixing length parameter on mass loss along the RGB. Different values of the mixing length parameter α will be explored. In particular, I will consider existing relations connecting the mixing length parameter α with the initial chemical composition of the star.

5.4.2 Limitations and potential future directions

This final section is focused on the prospects and the potential developments that could be performed in the long term.

Extrapolation to $\log g < 1.5$. As already mentioned in section 4.2, the 3D atmosphere models of the Stagger grid with the lowest surface gravity have $\log g = 1.5$. Therefore, the Stagger grid does not cover the upper part of the RGB, which is the evolutionary phase mostly affected by mass loss (as a reference, see the Stagger-grid coverage compared to the evolutionary track in the Kiel diagram of figure 5.12). To compute the mass loss rate along the upper portion of the RGB for the FPR3D models, I had to *extrapolate* the best-fit power laws of table 4.2 in the latest evolutionary phases, when the surface gravity decreases down to $\log g < 1.5$. This is the major limitation of the present work. Let me describe two tentative ideas that could eventually help to address this limitation:

- the natural solution would be having more 3D hydrodynamic simulations of giant atmospheres at $\log g < 1.5$. However, building box-in-a-star simulations at these very low surface gravities is very challenging. This is because the size of convective cells scales with pressure scale height (Lebzelter et al. 2012), which becomes huge when g decreases down to such low values. For this reason, by reducing $\log g$ to

the typical values of red supergiants (e.g., Betelgeuse), the convective cells would be so large that the whole atmosphere would only contain a few of them. As a result, sphericity effects start to be relevant when $\log g$ is diminished down to the typical values found at the very top of the RGB, and this makes the box-in-a-star approach impracticable at these extremely low surface gravities ($\log g \simeq 0.0-0.5$);

- a more plausible solution could be studying convection and its interplay with emission of acoustic energy in "star-in-a-box" simulations, where the whole star is enclosed in a cube (Freytag, Steffen, and Dorch 2002). These kinds of simulation were designed for extremely low-g stars.

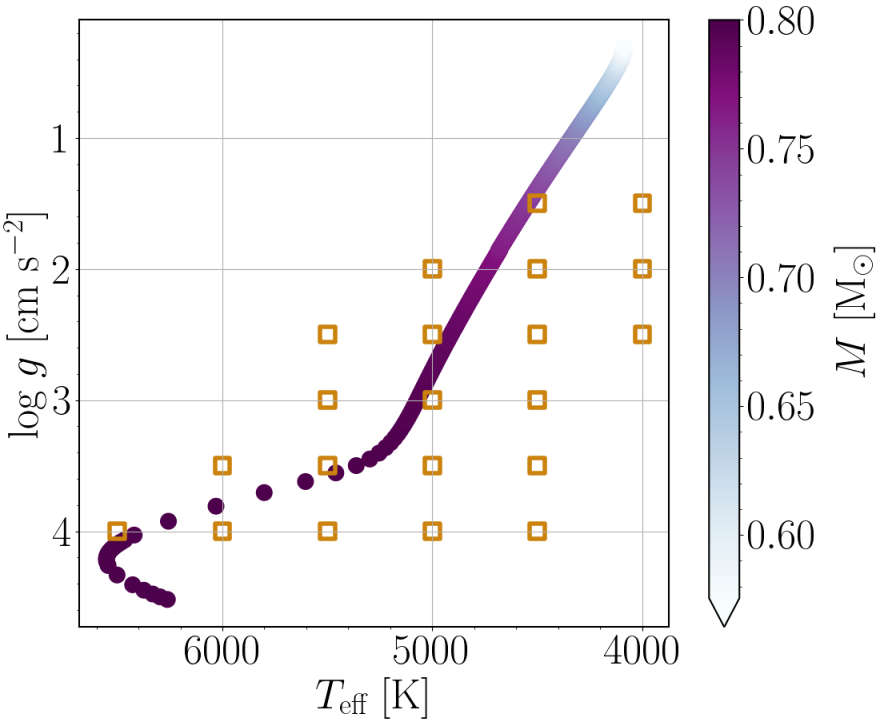

Figure 5.12: Evolutionary track on the Kiel diagram (from MS to the tip of the RGB) relative to the star of the FPR3D grid with initial mass $M_{\rm in} = 0.8\,{\rm M}_\odot$, initial $Y = 0.24$, [Fe/H] $= -2.00$. The color bar indicates the mass of the star along the RGB phase. The orange squared points are the targeted red giant atmosphere models of the Stagger grid.

Performing the same study on other grids. It would be interesting to do the same analysis performed in this project on other grids of 3D box-in-a-star simulations, such as the grid constructed with the CO^{5}BOLD code (Freytag, Steffen, Ludwig, et al. 2012) or the second version of the Stagger grid (Rodríguez Díaz et al. 2024). It would be interesting to see if the acoustic energy per unit area scales with g and $T_{\rm eff}$ similarly to the dependence discussed in section 4.3.2. If so, the results found in the FPR3D mass loss would be confirmed on a more solid basis.

Comparing with magnetically-driven mass loss. The results obtained in the present work could be compared with models where the mass loss rate is computed from stellar wind theories involving magnetic effects. For example, let me recall the

work proposed by MacDonald and Mullan (2025) about the possibility that mass ejecta could originate from magnetic recombination (see section 2.3 for more details). In their work, the authors derived three different expressions for the average mass loss rate after the RGB bump. In each of these relations, the mass loss rate linearly decreases with the number of density scale heights in the convection zone. Such relations could possibly be implemented in MESA. Therefore, performing this analysis would be interesting to see how the mass-loss predictions of the present work compare with a modelling grounded in completely different physical arguments.

The potential future role of 3D simulations. Thanks to 3D hydrodynamic simulations of atmosphere layers of giant stars and stellar convection, we can now search for improvements on the treatment of acoustic energy and go beyond the limitations affecting the classical theories of sound generation. This provides a starting point for improving the *existing* models where stellar winds are assumed to be powered by some mechanism involving the mechanical energy associated to acoustic waves. Indeed, this has been the core of this Master's thesis project: the acoustic energy per unit area was taken from 3D hydrodynamic simulations and then plugged in the structure of the FPR mass loss prescription (Fusi-Pecci and Renzini 1975), with the aim of computing the mass loss rate along the RGB.

However, besides improving the existing models of mass loss, 3D simulations can provide us further information on the *actual mechanisms* through which the acoustic energy could drive mass ejecta. Indeed, thanks to these advanced simulations, we can study the temporal evolution of acoustic waves and this can give us insights on their dissipation in the upper atmosphere. On the other hand, the use of MHD simulations provide also information on the properties of magnetic fields, thus potentially improving our understanding of those magnetic phenomena considered for years as plausible candidates for the origin of stellar winds from RGB stars (e.g., dissipation of Alfvén waves and MHD waves). Therefore, using 3D simulations could lay the groundwork for mass loss theories based on a more solid physical framework, eventually abandoning the use of efficiency factors as free parameters, which is still the main weakness affecting numerous mass loss prescriptions.

References

Adams, Walter S. and Elizabeth MacCormack (Mar. 1935). "Systematic Displacements of Lines in the Spectra of Certain Bright Stars". In: *The Astrophysical Journal* 81, p. 119. DOI: 10.1086/143620.

Aerts, Conny, Jørgen Christensen-Dalsgaard, and Donald W. Kurtz (2010). *Asteroseismology*. DOI: 10.1007/978-1-4020-5803-5.

Asplund, Martin et al. (Sept. 2009). "The Chemical Composition of the Sun". In: *Annual Review of Astronomy and Astrophysics* 47.1, pp. 481–522. DOI: 10.1146/annurev.astro.46.060407.145222. arXiv: 0909.0948 [astro-ph.SR].

Belkacem, K. et al. (2013). *On the seismic scaling relations $\Delta\nu - \bar{\rho}$ and $\nu_{\max} - \nu_c$*. arXiv: 1307.3132 [astro-ph.SR]. URL: https://arxiv.org/abs/1307.3132.

Böhm-Vitense, E. (Jan. 1958). "Über die Wasserstoffkonvektionszone in Sternen verschiedener Effektivtemperaturen und Leuchtkräfte. Mit 5 Textabbildungen". In: *Zeitschrift fuer Astrophysik* 46, p. 108.

Brogaard, K et al. (Feb. 2018). "Establishing the accuracy of asteroseismic mass and radius estimates of giant stars – I. Three eclipsing systems at $[Fe/H] \sim -0.3$ and the need for a large high-precision sample". In: *Monthly Notices of the Royal Astronomical Society* 476.3, pp. 3729–3743. ISSN: 1365-2966. DOI: 10.1093/mnras/sty268. URL: http://dx.doi.org/10.1093/mnras/sty268.

Brogaard, K. et al. (Nov. 2024). "Connecting integrated red giant branch mass loss from asteroseismology and globular clusters". In: *Astronomy & Astrophysics* 691, A288. ISSN: 1432-0746. DOI: 10.1051/0004-6361/202452033. URL: http://dx.doi.org/10.1051/0004-6361/202452033.

Christensen-Dalsgaard, J. (Jan. 2014). *Lecture Notes on Stellar Oscillations*.

Christensen-Dalsgaard, J. et al. (May 1996). "The Current State of Solar Modeling". In: *Science* 272.5266, pp. 1286–1292. DOI: 10.1126/science.272.5266.1286.

Dalessandro, E. et al. (Jan. 2011). "The peculiar horizontal branch of NGC 2808". In: *Monthly Notices of the Royal Astronomical Society* 410.1, pp. 694–704. DOI: 10.1111/j.1365-2966.2010.17479.x. arXiv: 1008.4478 [astro-ph.SR].

Deutsch, Armin J. (Mar. 1956). "The Circumstellar Envelope of Alpha Herculis." In: *The Astrophysical Journal* 123, p. 210. DOI: 10.1086/146152.

— (1960). "The Loss of Mass from Red Giant Stars". In: *Stellar atmospheres. Edited by Jesse Leonard Greenstein. Supported in part by the National Science Foundation. Published by the University of Chicago Press*. Ed. by Jesse Leonard Greenstein, p. 543.

Ferraro, F. R., B. Paltrinieri, and C. Cacciari (Jan. 1999). "Galactic globular clusters in the UV." In: *Memorie della Società Astronomica Italiana* 70, pp. 599–616.

Freytag, B., M. Steffen, and B. Dorch (July 2002). "Spots on the surface of Betelgeuse – Results from new 3D stellar convection models". In: *Astronomische Nachrichten*

323, pp. 213–219. DOI: 10.1002/1521-3994(200208)323:3/4<213::AID-ASNA213>3.0.CO;2-H.

Freytag, B., M. Steffen, H.-G. Ludwig, et al. (Feb. 2012). "Simulations of stellar convection with CO5BOLD". In: *Journal of Computational Physics* 231.3, pp. 919–959. DOI: 10.1016/j.jcp.2011.09.026. arXiv: 1110.6844 [astro-ph.SR].

Fusi-Pecci, F. and A. Renzini (Mar. 1975). "On mass loss by stellar wind in population II red giants." In: *Astronomy & Astrophysics* 39, pp. 413–419.

— (Feb. 1976). "On total mass loss in stars with $M \lessapprox 8M_{\odot}$." In: *Astronomy & Astrophysics* 46, pp. 447–454.

García, R. A. and D. Stello (2015). "Asteroseismology of red giant stars". In: *Extraterrestrial Seismology*. Ed. by V. Tong and R. Garcí, pp. 159–169. DOI: 10.1017/CBO9781107300668.014.

Gehrz, R. D. and N. J. Woolf (May 1971). "Mass Loss from M Stars". In: *The Astrophysical Journal* 165, p. 285. DOI: 10.1086/150897.

Glass, I. S. et al. (May 2009). "Mid-infrared period-magnitude relations for AGB stars". In: *Monthly Notices of the Royal Astronomical Society* 395.1, pp. L11–L15. DOI: 10.1111/j.1745-3933.2009.00628.x. arXiv: 0901.3032 [astro-ph.SR].

Gratton, Raffaele G., Eugenio Carretta, and Angela Bragaglia (Feb. 2012). "Multiple populations in globular clusters. Lessons learned from the Milky Way globular clusters". In: *The Astronomy and Astrophysics Review* 20, 50, p. 50. DOI: 10.1007/s00159-012-0050-3. arXiv: 1201.6526 [astro-ph.SR].

Greggio, L. and A. Renzini (2011). *Stellar Populations. A User Guide from Low to High Redshift*.

Han, Z. et al. (Oct. 2002). "The origin of subdwarf B stars - I. The formation channels". In: *Monthly Notices of the Royal Astronomical Society* 336.2, pp. 449–466. DOI: 10.1046/j.1365-8711.2002.05752.x. arXiv: astro-ph/0206130 [astro-ph].

Hartmann, L. and K. B. MacGregor (Nov. 1980). "Momentum and energy deposition in late-type stellar atmospheres and winds." In: *The Astrophysical Journal* 242, pp. 260–282. DOI: 10.1086/158461.

Heasley, J. N. and J. G. Mengel (June 1972). "An estimate of stellar wind mass loss during the red giant phase of evolution". In: *The Observatory* 92, pp. 93–96.

Jackiewicz, Jason (2021). "Solar-Like Oscillators in the Kepler Era: A Review". In: *Frontiers in Astronomy and Space Sciences* Volume 7 - 2020. ISSN: 2296-987X. DOI: 10.3389/fspas.2020.595017. URL: https://www.frontiersin.org/journals/astronomy-and-space-sciences/articles/10.3389/fspas.2020.595017.

Kitiashvili, I. N. et al. (Apr. 2016). "Dynamics of Turbulent Convection and Convective Overshoot in a Moderate-mass Star". In: *The Astrophysical Journal Letters* 821.1, L17, p. L17. DOI: 10.3847/2041-8205/821/1/L17. arXiv: 1512.07298 [astro-ph.SR].

Lebzelter, T. et al. (Nov. 2012). "Comparative modelling of the spectra of cool giants⋆⋆⋆". In: *Astronomy & Astrophysics* 547, A108, A108. DOI: 10.1051/0004-6361/201219142. arXiv: 1209.2656 [astro-ph.SR].

Li, Yaguang (Aug. 2025). "Evidence that Mass Loss on the Red Giant Branch Decreases with Metallicity". In: *The Astrophysical Journal* 988.2, 179, p. 179. DOI: 10.3847/1538-4357/ade3c7. arXiv: 2505.12794 [astro-ph.SR].

Lighthill, J. (Mar. 1952). "On Sound Generated Aerodynamically. I. General Theory". In: *Proceedings of the Royal Society of London Series A* 211.1107, pp. 564–587. DOI: 10.1098/rspa.1952.0060.

— (1978). *Waves in fluids*.

MacDonald, J. and D. J. Mullan (Aug. 2025). "A Plasmoid Model for Mass Loss from Stars on the Upper Red Giant Branch: The Mass-loss Rate is Controlled by the Number of Density Scale Heights in the Convection Zone". In: *The Astrophysical Journal Letters* 989.2, L28, p. L28. DOI: 10.3847/2041-8213/adf6ae. arXiv: 2508.05480 [astro-ph.SR].

Magic, Z. et al. (Sept. 2013). "The Stagger-grid: A grid of 3D stellar atmosphere models. I. Methods and general properties". In: *Astronomy & Astrophysics* 557, A26, A26. DOI: 10.1051/0004-6361/201321274. arXiv: 1302.2621 [astro-ph.SR].

Miglio, A., K. Brogaard, et al. (Jan. 2012). "Asteroseismology of old open clusters with Kepler: direct estimate of the integrated red giant branch mass-loss in NGC 6791 and 6819". In: *Monthly Notices of the Royal Astronomical Society* 419.3, pp. 2077–2088. DOI: 10.1111/j.1365-2966.2011.19859.x. arXiv: 1109.4376 [astro-ph.SR].

Miglio, A., C. Chiappini, et al. (Jan. 2021). "Age dissection of the Milky Way discs: Red giants in the Kepler field". In: *Astronomy & Astrophysics* 645, A85, A85. DOI: 10.1051/0004-6361/202038307. arXiv: 2004.14806 [astro-ph.GA].

Mosser, B. et al. (Nov. 2013). "Period-luminosity relations in evolved red giants explained by solar-like oscillations". In: *Astronomy & Astrophysics* 559, A137, A137. DOI: 10.1051/0004-6361/201322243. arXiv: 1310.0839 [astro-ph.SR].

Narain, U. and P. Ulmschneider (Dec. 1990). "Chromospheric and Coronal Heating Mechanisms". In: *Space Science Reviews* 54.3-4, pp. 377–445. DOI: 10.1007/BF00177801.

Parker, E. N. (Nov. 1958). "Dynamics of the Interplanetary Gas and Magnetic Fields." In: *The Astrophysical Journal* 128, p. 664. DOI: 10.1086/146579.

Paxton, Bill et al. (Jan. 2011). "Modules for Experiments in Stellar Astrophysics (MESA)". In: *The Astrophysical Journal Supplement Series* 192.1, 3, p. 3. DOI: 10.1088/0067-0049/192/1/3. arXiv: 1009.1622 [astro-ph.SR].

Philidet, J. (Sept. 2021). "Study of the coupling between turbulent convection and solar-like oscillations". Theses. Université Paris sciences et lettres. URL: https://theses.hal.science/tel-03850835.

Proudman, I. (Aug. 1952). "The Generation of Noise by Isotropic Turbulence". In: *Proceedings of the Royal Society of London Series A* 214.1116, pp. 119–132. DOI: 10.1098/rspa.1952.0154.

Reimers, D. (1975). "Circumstellar envelopes and mass loss of red giant stars." In: *Problems in stellar atmospheres and envelopes.* Ed. by B. Baschek, W. H. Kegel, and G. Traving, pp. 229–256.

Rodríguez Díaz, Luisa F. et al. (Aug. 2024). "An extended and refined grid of 3D STAGGER model atmospheres. Processed snapshots for stellar spectroscopy". In: *Astronomy & Astrophysics* 688, A212, A212. DOI: 10.1051/0004-6361/202348480. arXiv: 2405.07872 [astro-ph.SR].

Rood, Robert T. (Sept. 1973). "Metal-Poor Stars. V. Horizontal-Branch Morphology". In: *The Astrophysical Journal* 184, pp. 815–838. DOI: 10.1086/152373.

Salaris, Maurizio and Santi Cassisi (2005). *Evolution of Stars and Stellar Populations*.

Salaris, Maurizio, Alessandro Chieffi, and Oscar Straniero (Sept. 1993). "The alpha - enhanced Isochrones and Their Impact on the FITS to the Galactic Globular Cluster System". In: *The Astrophysical Journal* 414, p. 580. DOI: 10.1086/173105.

Samadi, R. (Dec. 2000). "Excitation stochastique des oscillations stellaires. Application à la mission spatiale COROT." Theses. Université Pierre et Marie Curie - Paris VI. URL: https://theses.hal.science/tel-00067734.

Schröder, K.-P. and Robert Connon Smith (May 2008). "Distant future of the Sun and Earth revisited". In: *Monthly Notices of the Royal Astronomical Society* 386.1, pp. 155–163. DOI: 10.1111/j.1365-2966.2008.13022.x. arXiv: 0801.4031 [astro-ph].

Stello, D. et al. (Dec. 2016). "The K2 M67 Study: Revisiting Old Friends with K2 Reveals Oscillating Red Giants in the Open Cluster M67". In: *The Astrophysical Journal* 832.2, 133, p. 133. DOI: 10.3847/0004-637X/832/2/133. arXiv: 1610.03060 [astro-ph.SR].

Tailo, M. et al. (June 2022). "Asteroseismology of the multiple stellar populations in the globular cluster M4". In: *Astronomy & Astrophysics* 662, L7, p. L7. DOI: 10.1051/0004-6361/202243721. arXiv: 2205.06645 [astro-ph.SR].

Unno, Wasaburo et al. (1989). *Nonradial oscillations of stars*.

Weymann, R. (Sept. 1960). "Coronal Evaporation as a Possible Mechanism for Mass Loss in Red Giants." In: *The Astrophysical Journal* 132, p. 380. DOI: 10.1086/146937.

— (Jan. 1963). "Mass Loss from Stars". In: *Annual Review of Astronomy and Astrophysics* 1, p. 97. DOI: 10.1146/annurev.aa.01.090163.000525.

Zhou, Yixiao et al. (2025). *Coupling 1D stellar evolution with 3D-hydrodynamical simulations on-the-fly III: stellar evolution at different metallicities*. arXiv: 2506.05094 [astro-ph.SR]. URL: https://arxiv.org/abs/2506.05094.